

Functional waterborne polymer dispersions for high performance anticorrosion coatings

Stefano Chimenti

Supervised by: Dr. M. Paulis and Prof. J. R. Leiza

Chemical Engineering Group

University of the Basque Country UPV/EHU

Donostia-San Sebastián

(2019)



POLYMAT

Contents

Chapter 1

Introduction and thesis outline

1.1	Introduction.....	3
1.2	An insight into the corrosion mechanism.....	4
1.3	Protective mechanism.....	7
1.4	Organic coating systems for corrosion protection.....	8
1.5	Conversion coatings.....	10
1.6	Primers.....	11
1.6.1	Binders.....	12
1.6.1.1	Epoxy resins.....	12
1.6.1.2	Alkyd resins.....	13
1.6.1.3	Polyurethane resins.....	13
1.6.1.4	Acrylic resins.....	14
1.6.2	Pigments.....	15
1.7	Motivation and Objective of the work.....	18
1.8	Outline of the thesis.....	21
1.9	References.....	24

Chapter 2

In-situ phosphatization and enhanced corrosion properties of films made of phosphate functionalized nanoparticles

2.1	Introduction.....	43
2.2	Synthesis of phosphated Poly (MMA-co-BA) waterborne dispersions.....	46
2.3	Polymerization kinetics and evolution of particles size.....	48
2.4	Latex application on steel substrate.....	50
2.4.1	In-situ phosphatization and influence of drying conditions.....	50
2.4.2	Characterization of the in-situ phosphatization.....	55
2.5	In-situ phosphatization and anticorrosion protection.....	67
2.6	Conclusions.....	73
2.7	References	75

Chapter 3

Effect of the incorporation of hydrophobic perfluorinated monomer in the corrosion protection of waterborne latexes

3.1	Introduction.....	85
3.2	Synthesis of phosphated Poly(POA-co-MMA-co-BA) waterborne dispersion.....	87
3.3	Influence of the perfluorooctyl acrylate on the evolution of particle size	89
3.4	Influence of the incorporation of POA on the film formation	90
3.5	Anticorrosion properties of POA based latexes	93
3.5.1	Influence of the coating thickness on the corrosion protection of PMB latex based film.....	96
3.5.2	The influence of iron phosphate layer on the corrosion protection	98
3.5.3	Evaluation of corrosion protection of PMB film in harsh conditions.	100
3.5.4	Evaluation of the barrier properties of PMB films.....	101
3.6	Conclusions.....	106
3.7	References	107

Chapter 4

Assessment of particle morphology of perfluorooctyl acrylate containing latexes

4.1	Introduction.....	115
4.2	PMB polymer particles morphology.....	115
4.3	TEM characterization of cryo-sectioned wet films.....	118
4.4	sSNOM characterization of cryo-sectioned wet films.....	123
4.5	Conclusions.....	130
4.4	References	131

Chapter 5

Use of ZnO nanoparticles as corrosion inhibitors in fluorinated acrylic polymer latexes

5.1	Introduction.....	135
5.2	ZnO nanoparticles preliminary characterizations.....	137
5.2.1	ZnO nanoparticles wettability	137
5.2.2	Miniemulsion stability.....	139
5.3	Encapsulation of ZnO nanoparticles in perfluorinated latexes	142
5.3.1	Batch miniemulsion polymerization.....	142
5.3.2	ZnO nanoparticles encapsulation	144
5.3.3	Film formation on steel substrate	146
5.3.4	Corrosion evaluation.....	150
5.4	Encapsulation of ZnO nanoparticles in perfluorinated latexes containing Sipomer PAM200	155
5.4.1	Seeded semibatch emulsion polymerization.....	155
5.4.2	Nanohybrid latex morphology.....	156
5.4.3	Corrosion properties	158
5.5	Conclusions.....	160
5.6	References	162

Chapter 6

Synergic effect of semicrystalline nanodomains and in-situ phosphatization on the anticorrosion properties of waterborne latexes

6.1	Introduction	171
6.2	Synthesis of phosphated Poly(SA-co-MMA-co-BA) latexes with core-shell morphology.....	173
6.3	Influence of nanocrystalline domains on the barrier properties of the final coating.....	178
6.4	Corrosion protection of waterborne latexes containing nanocrystalline domains	184
6.5	Conclusions	192
6.6	References	193

Chapter 7

Performance of phosphated waterborne binders in Direct to Metal (DTM) Paints

7.1	Introduction	203
7.2	Synthesis of waterborne binders for DTM paint.....	205
7.3	DTM paint preparation.....	207
7.4	Performance of DTM paints	208
7.4.1	Adhesion resistance.....	210
7.4.2	Flash rust resistance	213
7.4.3	High Humidity resistance.....	213
7.4.4	Weathering cyclic test.....	222
7.4.5	Salt spray test	224
7.5	Conclusions	225
7.6	References.....	226

Chapter 8

8. Conclusions.....	229
---------------------	-----

List of publications and conference presentations

Publications.....	235
Presentation	237
Posters	238

Appendix I

Materials and experimental setup

I.1 Materials.....	240
I.2 Experimental setup.....	241

Appendix II

Characterization and preparation methods

II.1 Conversion.....	245
II.2 Contact Angle measurement.....	246
II.3 Dynamic light scattering.....	246
II.4 Differential Scanning calorimetry (DSC).....	246
II.5 Electrochemical Impedance Spectroscopy (EIS).....	247
II.6 Film application on steel substrates.....	248
II.7 FTIR.....	249
II.8 MALDI-TOF.....	250
II.9 Multispeckle Diffusing Wave Spectroscopy (MDWS).....	250
II.10 Nuclear Magnetic Resonance (NMR).....	252
II.11 Powder Wettability test.....	253
II.12 Scanning electron microscopy with Energy dispersive X-rays analysis (SEM/EDX).....	254
II.13 Scattering-type Scanning Near-field Optical Microscope (sSNOM).....	255
II.14 Salt Spray test.....	255
II.15 Transmission Electron Microscopy (TEM).....	256
II.16 Water sensitivity.....	257
II.17 References.....	257

Appendix III

Supporting Information

III.1	Chapter 1	261
III.2	Chapter 2	263
III.3	Chapter 3	265
III.4	Chapter 5	266
	III.4.1 MALDI-TOF characterization	266
	III.4.2 ZnO encapsulation semibatch reaction screening.....	268
III.5	Chapter 6	269
III.6	Chapter 7	269
	III.6.1 Pigments.....	270
	III.6.2 Thickeners	270
	III.6.3 Dispersing agent.....	271
	III.6.4 Defoamer.....	272
	III.6.5 Biocide	272
III.7	Reference	273

Acronyms list

Acronyms list	277
---------------------	-----

Resumen y conclusiones

Resumen y conclusiones.....	281
-----------------------------	-----

Chapter 1

Introduction and thesis outline

1.1	Introduction.....	3
1.2	An insight into the corrosion mechanism	4
1.3	Protective mechanism.....	7
1.4	Organic coating systems for corrosion protection.....	8
1.5	Conversion coatings	10
1.6	Primers.....	11
1.6.1	Binders	12
1.6.1.1	Epoxy resins	12
1.6.1.2	Alkyd resins.....	13
1.6.1.3	Polyurethane resins.....	13
1.6.1.4	Acrylic resins.....	14
1.6.2	Pigments	15
1.7	Motivation and Objective of the work.....	18
1.8	Outline of the thesis.....	21
1.9	References.....	24

1.1 Introduction

Mild steel is used as primary constructional material in many sectors such as transportation, infrastructures and utilities. However, it is very much prone to corrosion and its protection against deterioration is challenging and necessary. Corrosion can be defined as a chemical or electrochemical process that degrades the surface of a metal¹. Moreover, it is a very fast process that causes lots of economic losses; according to NACE International, the global cost of corrosion was estimated to be US\$2.5 trillion, which is equivalent to 3.4% of the global GDP (2013)². In addition to the economic cost, corrosion can lead to structural failure that can have dramatic consequences for humans and the environment^{3,4}.

Because of that the industrial and scientific community are devoting large efforts to developing efficient and suitable corrosion protection systems that are able to provide complete protection under different conditions. In order to design the best protective strategy, an in-depth knowledge of the corrosion mechanism is needed. In fact, according to the way in which corrosion is triggered and how it develops (which is also depend on the surrounding environment) it is possible to build up different protection strategies.

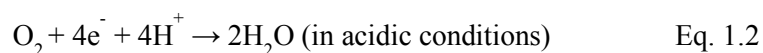
1.2 An insight into the corrosion mechanism

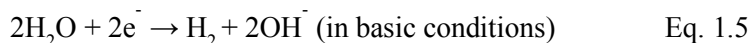
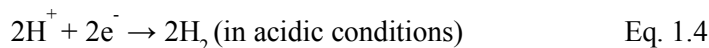
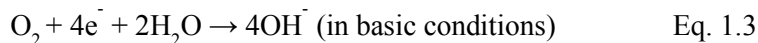
Corrosion is the result of an electrochemical reaction between two separate areas with different potentials i.e., an anode and a cathode, that requires an electrolyte solution and a metallic conductor. The formation of ferrous oxides (rust) is a well-known consequence of the corrosion process when iron and steel corrode, but many other metals are also prone to suffer corrosion. For instance, the green-colored patina on copper and the white rust on zinc are other examples of corrosion products.

Generally, the corrosion mechanism of a metal in aqueous media is an electrochemical process involving anodic (or oxidation) and cathodic (or reduction) reactions and it can be described as follows⁵. Dissolution of a metal M, which represents an anodic reaction, is presented by the half-cell reaction:



The electrons of the anodic reaction must be consumed by a cathodic reaction for corrosion to proceed. Two predominant cathodic reactions in aqueous corrosion are oxygen reduction (Equation 1.2 and 1.3) and hydrogen evolution (Equation 1.4 and 1.5) respectively and they are pH dependent⁵. Their half-cell reactions are represented as follows:





Oxygen reduction can only occur in aerated solutions, which contain dissolved oxygen molecules, whereas hydrogen evolution can occur in both deaerated and aerated solutions.

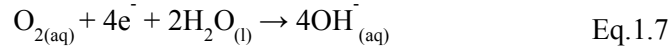
For corrosion to occur, however, the cell potential, E_{cell} , of the overall reaction must be positive, which corresponds to a decrease in Gibb's free energy ($\Delta G^\circ < 0$). E_{cell} is the difference in the equilibrium potential of the cathodic half-cell reaction (E_{Red}) and the anodic half-cell reaction (E_{Ox}). (Equation 1.6).

$$E_{cell} = E_{Red} - E_{Ox} \quad \text{Eq. 1.6}$$

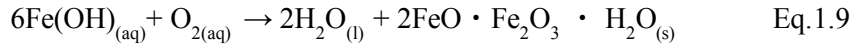
In principle, the standard electrode potential may be used as a measure of the thermodynamic vulnerability of metals towards corrosion (the lower the E_{Ox} the higher the susceptibility towards corrosion).

In the specific example of iron and its alloys, when the metal is in contact with water, the formation of anodic and cathodic areas on its surface occurs⁶. At the cathode, the oxygen is reduced on a catalytically active surface of oxidized metal, mainly to hydroxyl ions, as given in Equation 1.7. At the anode, several corrosion reactions take

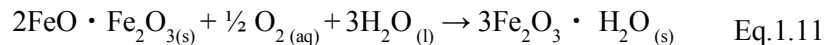
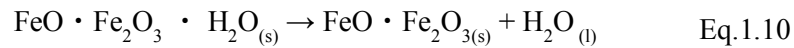
place ⁶ and the net result is the production of ferrous ions and electrons given in Equation 1.8.



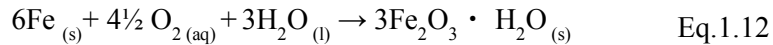
In these conditions, iron ions interact with the hydroxyl ions and form hydroxides, that further convert into ferrous oxides in their hydrated state, i.e. the green magnetite (Equation 1.9)⁶.



However, hydrated magnetite is unstable and will decompose into black magnetite (Equation 1.10), which, in the presence of oxygen, will subsequently oxidize into stable red-brown hydrated hematite (frequently referred to as rust) (Equation 1.11)⁶.



Hence the overall reaction is summarized in Equation 1.12.



It has to be said that the presence of chloride ions, such as in marine environments, is known to accelerate the corrosion process. In fact, in the corrosion process, due to

the flow of the released electrons (Equation 1.8) from the anode to the cathode, the solution enclosed in the anodic area gains positive electrical charges (Fe^{n+}), which subsequently attracts negatively charged chlorine ions (Cl^-)^{7, 8}. This results in the formation of intermediate iron chlorides compounds that readily react with water to form iron hydroxides and hydrochloric acid (Equation 1.14) and hence a drastic pH drop, from 6 to 2-3, that causes a further acceleration of the corrosion^{7, 8}.

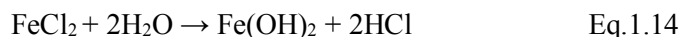


Figure 1.1 shows a schematic representation of all the reactions involved in the corrosion process.

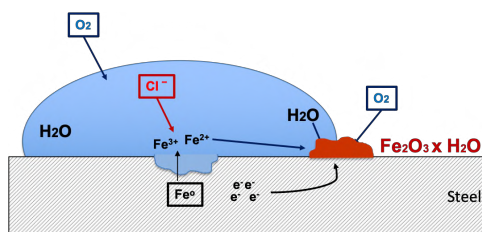


Figure 1.1 *Illustration of corrosion process of steel in the presence of water, oxygen and chlorine ions.*

1.3 Protective mechanism

When the integrity of the metal is affected by the external action of the environment, it becomes necessary to protect it against this detrimental action and the application of a coating results to be one of the most suitable routes.

According to the corrosion mechanism, described in section 1.2, it is clear that the first property that a coating must provide is an effective physical barrier, impeding the diffusion of detrimental agents (water, electrolyte and oxygen⁹⁻¹¹) to the metallic surface. It is worth to mention that the degree of protection, apart from the nature of the coating, is highly dependent on its thickness. In fact, the delamination and the formation of defects has been reported to be significantly reduced when the thickness of the coating is increased^{12,13}, due to the semipermeable behavior of the coating¹⁴. In addition to the barrier effect, the coating must offer the ability to inhibit the corrosion process, in case of failure of the coating, which can be obtained either by means of the passivation of the iron surface or through the addition of inhibiting pigments that are able to quench the corrosion process if triggered by an external stimulus¹⁵. As alternative to the inhibition effect, sacrificial protection (based on the galvanic effect¹⁶) can be provided through the presence of a more active metal that is more prone to corrode than the iron.

1.4 Organic coating systems for corrosion protection

One of the strategies used to prevent the corrosion, where the scientific community is devoting large efforts, is the development of protective organic coatings¹⁷⁻²¹. In fact, thanks to the wide variety of polymers that can be employed as well as their tunability,

organic coatings can offer a physical barrier, impeding the diffusion of corrosive species to the metal surface, and the inhibition of the corrosion reactions that threaten the underlying metal. In principle, for significant corrosion protection one single layered coating is not enough and a more robust coating system is used. Usually, they are designed as multilayer systems with a thickness in the range of hundreds of microns and where each layer provides specific functionality^{6,15,19,22}. A typical coating system comprises a conversion coating directly applied on the metal surface, a primer, one or more intermediate coats and a topcoat (Figure 1.2).

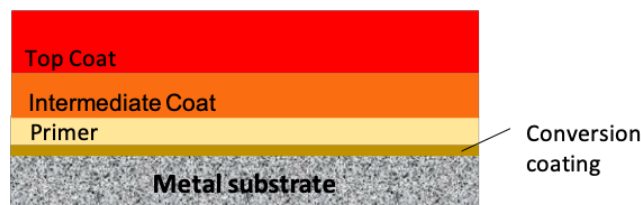


Figure 1.2. *Multilayer corrosion protection coating.*

However, depending on the final application, not all these layers are applied. For instance, for housing appliance, only the primer and the top-coat are used, while in the automotive and infrastructure sectors, where long lasting protection is required, conversion coating is always applied below the primer and top-coat. In the case of marine applications, which are characterized by highly corrosive conditions, additional intermediate coats are employed to build up the coating thickness and hence to reduce

the permeation of corrosive species. It should be noted that, while the top and the intermediate coats are substantially used to provide thickness, gloss, aesthetic mechanical and thermal stability, the corrosion protection is mainly provided by the conversion coating and the primer.

1.5 Conversion coatings

A conversion-coating is necessary to obtain primary adhesion to the metal surface and to provide an electrical barrier^{23,24}. Commonly, it is a metal oxide passive layer, which is deposited onto the substrate under controlled conditions and it is characterized by uniform thickness, low porosity and electrical resistance.

Chromate conversion coatings have been quite commonly used in corrosion protection. However, due to environmental and safety regulations the use of chromium hexavalent (high toxicity) is prohibited^{25,26}. As a nontoxic alternative the phosphating conversion coating is widely used, even if it renders a lower level of corrosion protection, due to its higher porosity with respect to the analogous chromate layer²⁷⁻²⁹.

As new developments, aqueous pretreatments have been introduced, which combine organic and inorganic chemistry such as the silane/siloxane coatings³⁰. These coatings employ the formation of silane/polysiloxane layers³¹ from a sol-gel process^{32, 33}. Typical representatives of this class of compounds are terminal aminopropyl triethoxy

silane (γ -APS), or bis-(triethoxysilyl)ethane (BTSE). The process involves controlled hydrolyzation of the Si-OC₂H₅ functions, bonding the surface via metal-O-Si linkages, and polymerization/crosslinking of the affixed hydroxysilane moieties to form a polysiloxane. Thanks to that, the functionalized organic groups protrude from the substrate surface, becoming available for bonding with the subsequent primer coat.

1.6 Primers

The primer forms a physical barrier, that prevents the access of detrimental agents to the metal surface, and provides additional corrosion protection through either inhibitive or sacrificial (galvanic) protection^{34,35}. Generally, primers used in corrosion protection are solvent based but, due to the tightening of the environmental regulation requirements and sustainability^{36,37}, waterborne coatings have become increasingly interesting in the coating industries thanks to their low content in volatile organic compounds (VOC).

Waterborne primers, contain different additives than organic solvent based primers and an appropriate choice among the various alternatives brings a challenge, to both manufacturers and researchers, in providing long-lasting corrosion protection. However, the two main components that constitute and play a key role in anticorrosion protection are the polymeric binders and the pigments.

1.6.1 Binders

The binder represents the film forming agent that controls most of the properties and performance that the coating should have, i.e. hardness, strength, adhesion to the substrate, chemical and weather resistance, cohesion with the other component of the coating and low permeability.

In this section a description of the structure and properties of the most common types of waterborne binders used in the formulation of anticorrosive coatings is presented.

1.6.1.1 Epoxy resins

Epoxy resins present extremely good barrier properties, good substrate adhesion and very good mechanical properties.³⁸ The molecular weight of the epoxy resin and the presence of stable carbon-carbon and ether bonds in the backbone, control the cross-linking density, hardness, flexibility, resistance to chemicals^{15,39-41} and hence the final anticorrosion properties. Nevertheless, epoxy resins present poor light stability, generally exhibiting strong chalking, discoloration, loss of gloss and color. These degradations take place mainly in the surface of the film, leaving the protective properties of the coating unaffected. For that reason, the use of this type of binder is limited to coatings for which aesthetic are not so important or include the application of an additional top coat with low color change and high gloss retention, e.g. a polyurethane topcoat³⁹.

1.6.1.2 *Alkyd resins*

An alkyd is a polyester modified by the addition of fatty acids that can contain up to 70 % of oil content. Alkyd resins undoubtedly represent a large segment in the coating market thanks to their broad application range, good price-quality balance, large content of renewable materials, long shelf life and optimal adhesion to the substrate (even poorly prepared metal) thanks to the large extent of functional groups present in the backbone (double bonds, hydroxyl groups and carboxylic groups)^{15, 39}. However, alkyd coatings should be applied with care in anticorrosive environments because they are subjected to saponification⁴². In fact, the ester linkages are attacked by alkaline materials to form an alcohol and the salt of a carboxylic acid and hence impair the anticorrosion protection especially in galvanized steel or in zinc-rich primers.

Solventborne alkyds continue to be widely used due to their balance of application and film performance. However, some waterborne alkyd-modified resins^{43,44} show a reduction in performance gap with their solventborne counterparts, including dry time, gloss, adhesion, corrosion and humidity resistance.

1.6.1.3 *Polyurethane resins*

Compared to the epoxy coatings technology, the advantage of polyurethane coatings is their excellent resistance to weathering. This type of coatings exhibits low loss of gloss and color change when exposed to ultraviolet radiation⁴⁵. This means that

polyurethane coatings are often applied as topcoats in environments where the coating system is exposed to sunlight. However, polyurethane coatings are also commercially available in primers and intermediate coatings formulation. Another advantage of these coatings is the “self-healing” (scratch resistant) ability due to hydrogen bonds between the urethane linkages, which may reform after “breakage”^{46, 47}. Waterborne polyurethane resins are generally known as PUD (polyurethane dispersion) and combine the benefits of polyurethane coating with the solvent free (organic) characteristic of waterborne systems⁴⁶. They usually comprise a hydroxyl functional polymer, such as polyester polyol or acrylic polyol, and the hardener which is at least a diisocyanate having a hydrophilic group in order to be water dispensable ⁴⁶. Nevertheless, it is noteworthy the fact that the reduction of the gap between solventborne and waterborne, in terms of chemical and corrosion resistance, is challenging making the first the preferred choice in the most demanding applications (exposition in industrial or marine sites)^{39, 46}.

1.6.1.4 Acrylic resins

Acrylic polymers and copolymers are widely used for the formulation of protective coatings, due to their good adhesion, film forming properties and environmental stability (against UV and hydrolysis after extended weathering) ^{15, 39}. Acrylic binders present a great latitude of formulation due to the versatility of acrylic building blocks

on copolymerizing with other monomers such as vinyl acetate and styrene. Moreover, they can be easily synthesized in waterborne media and, according to the synthetic procedure, it is possible to control their final properties. They are produced by emulsion or miniemulsion polymerization^{48, 49} (these type polymerization have been used in the present work and their brief description is presented in Appendix III.1).

Contrary to epoxy resins, acrylic resins are not adequate for constant and prolonged immersion in water due to their higher water sensitivity⁵⁰⁻⁵⁴. Moreover, if compared with the solventborne counterparts, waterborne acrylic resins present weaker adhesion to the substrate and slow drying which can impair the anticorrosive properties.

1.6.2 Pigments

Almost all the waterborne binders present the same limitation in the use as anticorrosive coatings, i.e., the occurrence of flash rust and the lower barrier properties if compared with their solventborne counterpart. The flash rust⁵⁵ is a phenomenon that appears quickly, especially when thin water films reside on the metal surface triggering the corrosive action. In order to prevent flash rust corrosion from taking place^{20, 56}, unlike in solventborne systems, the addition of pigments is always considered in the waterborne paints formulation. Anticorrosive pigments have a strong influence on the performance of protective coatings in several ways, i.e. they can increase the durability of the coating system and prevent the underfilm corrosion by means of either

decreasing or quenching the reaction rates. Usually, they may be classified, based on their function as, barrier pigments, sacrificial pigments and inhibitive pigments⁵⁷.

1.6.2.1 Barrier pigments

Barrier protection is, to a certain extent, offered by any particle that is impermeable to aggressive species and incorporated into a coating. However, some pigments are especially designed to impart barrier properties to an organic coating by impeding the transport of aggressive species to the surface of the substrate^{9, 58-65}. Such pigments are typically lamellar or flake-shape pigments, which orientate themselves parallel to the substrate surface and protect the substrate by providing a tortuous path of diffusion. In addition, lamellar pigments may have a reinforcing effect on the mechanical properties of the coating⁶⁶. For instance, some of the most commonly used barrier pigments are chemically inert aluminum flakes⁶⁷, glass flakes⁶⁷ and micaceous ion oxides⁶⁸⁻⁷⁰. However, the most important characteristics that a barrier pigment should have are to be insoluble in the applied medium and to be inert.

1.6.2.2 Sacrificial pigments

An alternative way of protecting ferrous substrate is the utilization of metallic pigments that are more likely to corrode than iron, i.e. zinc or magnesium and their alloys⁷¹⁻⁷⁴. In fact, zinc itself acts as a sacrificial anode and dissolves into the aqueous media whereas the steel acts as cathode (the whole process is therefore termed cathodic

protection mechanism)⁷⁵. It is worth to mention that the electrochemical efficiency of zinc-rich coating does not last forever due to corrosion products formed at the particles interface. Nevertheless, this reaction between zinc and the atmosphere might be beneficial in terms of filling pores or pinholes of the paint films with insoluble zinc compounds (cementification).

1.6.2.3 *Inhibitive pigments*

Contrary to barrier pigments, inhibitive pigments show a certain controlled solubility which results in either chemical and/or electrochemical activity. Inhibitive pigments may be classified according to their effect on the cathodic and anodic reactions^{15, 39, 76}. Cathodic inhibitors, such as inorganic salts of magnesium and manganese, suppress corrosion at the cathode by the consumption of the free electrons released from the anode and by forming insoluble deposits with hydroxyls ions⁷⁷⁻⁷⁹.

Anodic inhibitors, such as inorganic salts of phosphate, borate, and silicate compounds, form a protective oxide film on the metal surface^{76, 80-83}. Anodic inhibitors are absorbed onto the surface of the substrate and reduce the rate of corrosion by increasing the anodic polarization. Moreover, neutralization of acidic or corrosion stimulating substances like chlorides ions is another pathway which can be chosen by utilization of a combination of metals with both anodic and cathodic inhibition effect⁵⁷.

1.7 Motivation and Objective of the work

This thesis is focused on the design of environmentally friendly coatings based on waterborne acrylic dispersion that are able to provide high corrosion protection of low carbon steel, through the combination of different anticorrosion capabilities, i.e. barrier and inhibitive properties. The choice of acrylic resin was driven by their easy production in waterborne media (emulsion polymerization), their versatility in terms of final properties (depending on their composition) and their good weather resistance. At the same time, the reduction of the water sensitivity as well as the enhancement of their poor adhesion to the substrate was investigated.

Standard anticorrosion acrylic coatings developed so far, require thicker and multiple layers that combine several functions in order to provide complete protection. The next generations of protective coatings should be much thinner (thus reducing the CO₂ emission and the quantity of raw materials per m² of the substrate) and have to be characterized by multiple functions, i.e. self-healing, antifouling or hydrophobicity, that are highly desired by high-added value applications, such as in automotive and aerospace industries. In this respect, recent developments in nanotechnology and the combination of different chemistries are the most promising^{18, 20, 39}. Keeping this in mind, we tried to combine the passivation effect, that phosphate ions have on the steel surface, with the good film forming properties of a conventional waterborne acrylic latex. There are some work in literature in which

a phosphating agent is blended with the acrylic latex⁸⁴ or in which phosphate functionalities are incorporated into the polymer composition^{85, 86}. However, in these cases, the corrosion protection was not good enough to avoid the use of anticorrosion inhibitors¹⁰³.

The incorporation of phosphate functionalities on the surface of the latex polymer particles, based on methyl methacrylate (MMA) and butyl acrylate (BA), was investigated. The ability to in-situ passivate the steel substrate during the film application was targeted along with the capability to prevent the corrosion from occurring by means of a thin single layer (below 70 μm).

Later, in order to enhance the barrier properties and hence to extend the anticorrosion protection, the hydrophobicity of the initial coating containing phosphate functionalities, was increased through the addition of a hydrophobic comonomer into the polymer composition. Hydrophobicity and superhydrophobicity are key surface properties for corrosion protection because they result in water and aqueous electrolyte repellence, antifouling and antibio-corrosion^{18, 87-91}. These functionalities can be achieved by incorporating functional species in the polymer composition or even tuning the morphology of the outermost surface layer⁹²⁻⁹⁴. For instance, Styrene/acrylic copolymers are widely used as hydrophobic coatings in corrosion protection^{95, 96}, but the incorporation of fluoro containing monomers have shown higher enhancement in

corrosion protection. Polyurethane coatings modified with waterborne perfluoroalkyl methacrylic⁹⁷ co-polymers displayed effective anti-wetting and self-cleaning properties, which are desirable properties especially for coating that are used in marine environments where low surface energy surfaces are used to avoid the adhesion and the diffusion of corrosive agents. In a recent work of Lopez et. al^{93, 94, 98}, the incorporation of hydrophobic perfluoro dodecyl acrylate (PDFA) shows a considerable enhance of the surface hydrophobicity of the resulting films. However, due to the new regulation imposed by the European Commission⁹⁹, the PDFA was banned from its use in many application as it is considered a harmful compound for the environment. On the other hand, the use of perfluorooctyl acrylate monomer(POA) was not limited by the EU regulation and because of that, its incorporation in the initial acrylic system (poly(MMA-co-BA)) was performed and the anticorrosion performance tested and compared with the previous systems.

The introduction of ZnO nanoparticles as anticorrosion inhibitor, in combination with the presence of phosphate functionalities was also evaluated for waterborne coatings that present poor anticorrosive protection. In detail, the encapsulation of ZnO by miniemulsion and seeded semibatch emulsion polymerization was carried out.

As alternative to the POA comonomer, the incorporation of hydrophobic Stearyl Acrylate (SA) to the initial coating system containing phosphate functionalities was considered in this work. Moreover, thanks to the ability of poly(SA) to crystallize, we aimed at reducing the diffusion of detrimental agents through the coating by the presence of semicrystalline nanodomains.

Finally, the synthesized waterborne latexes were incorporated in commercial anticorrosion paint formulation and the analysis of the final paints has also been included in the present work.

1.8 Outline of the thesis

Chapter 2 reports the synthesis of a thin, stand-alone waterborne coating (based on Poly(methyl methacrylate-co-Butyl acrylate) copolymer) with excellent anticorrosion performance, successfully designed thanks to a built-in ability to in-situ phosphatize low carbon steel substrates. During film formation, the phosphate functionalities, incorporated by using a phosphate functional surfmer (Sipomer PAM200), were able to interact with steel leading to a thin iron phosphate passive layer at the coating-metal interface. The phosphatization layer that plays a key role on the excellent anticorrosion properties obtained (measured by EIS analysis of coated sample immersed in 3.5 wt% NaCl solution and in an aggressive salt spray chamber) strongly depends on the

humidity at which the waterborne dispersion is applied; at relative humidity above 60%, optimum performance is achieved.

Chapter 3 shows the attempts to increase of hydrophobicity of the coating containing phosphate functionalities, described in Chapter 2, that was achieved throughout the incorporation of perfluorooctyl acrylate comonomer into the polymer composition. Unexpected lack of particles coalescence during the film formation affected the barrier properties and hence the corrosion performance of the coating, which resulted in worse anticorrosion properties than the less hydrophobic coating.

Chapter 4 presents the study carried out on the phase separation that occurred into the polymer particles containing perfluorooctyl acrylate, synthesized in Chapter 3, that is likely the reason of the observed lack of coalescence during the film formation. The morphology and the composition of each phase present in the polymer particle was investigated by TEM and sSNOM (scattering-type scanning near-field optical microscope).

In **Chapter 5** the encapsulation of zinc oxide nanoparticles (ZnO) into the perfluorinated latex carried out either by batch miniemulsion polymerizations or by means of seeded semibatch emulsion polymerization is shown. The beneficial effect of

the incorporation of ZnO was observed by EIS after immersion in 3.5 wt% NaCl solution.

Chapter 6 reports the synergic combination of enhanced barrier properties and a built-in ability to in-situ phosphatize low carbon steel substrate. On the one hand, the physical barrier protection was provided by a homogeneous dispersion of semicrystalline nanodomains in the polymer matrix, which was achieved from the coalescence of polymer particles with core-shell morphology. On the other hand, the in-situ phosphatization was provided according to the mechanism described in Chapter 2. This synergic effect represents the key strength of the excellent anticorrosion properties achieved (measured by EIS analysis of coated sample immersed in 3.5 wt% NaCl solution and in an aggressive salt spray chamber).

Chapter 7 presents the work carried out in VINA-VIL spa. (Villadossola, Italy) under the supervision of Dr. Marco Cerra. In this chapter the incorporation of the waterborne latexes developed in POLYMAT into commercial paint formulation for Direct to Metal (DTM) paints is shown, without the addition of any anticorrosion inhibitors. The resulting DTM paint have been tested in several corrosion tests and compared with a commercial VINA-VIL DTM paint containing corrosion inhibitors.

In **Chapter 8** the most relevant conclusions of this PhD thesis are summarized.

1.9 References

1. Groysman, A., Corrosion Phenomena. In *Corrosion for Everybody*, Springer Netherlands: Dordrecht, 2010; pp 53-108.
2. International Measures of Prevention, Application and Economics of Corrosion Technology (IMPACT). *NACE international* **2013**.
3. Fragata, F.; Salai, R. P.; Amorim, C.; Almeida, E., Compatibility and incompatibility in anticorrosive painting: The particular case of maintenance painting. *Progress in Organic Coatings* **2006**, 56 (4), 257-268.
4. Pandey, M.; Nessim, M., Reliability-based inspection of post-tensioned concrete slabs. *Canadian Journal of Civil Engineering* **1996**, 23 (1), 242-249.
5. Hihara, L. H., Chapter 1 - Electrochemical Aspects of Corrosion-Control Coatings. In *Intelligent Coatings for Corrosion Control*, Tiwari, A.; Rawlins, J.; Hihara, L. H., Eds. Butterworth-Heinemann: Boston, 2015; pp 1-15.
6. Jones, D. A., *Principles and prevention of corrosion* 2nd Ed.; Upper Saddle River, NJ : Prentice Hall, 1996.

7. Song, Y.; Jiang, G.; Chen, Y.; Zhao, P.; Tian, Y., Effects of chloride ions on corrosion of ductile iron and carbon steel in soil environments. *Scientific Reports* **2017**, *7* (1), 6865.
8. Ma, F.-Y., Corrosive effects of chlorides on metals. In *Pitting corrosion*, InTechOpen: 2012.
9. Thomas, N. L., The barrier properties of paint coatings. *Progress in Organic Coatings* **1991**, *19* (2), 101-121.
10. Bacon, R. C.; Smith, J. J.; Rugg, F. M., Electrolytic Resistance in Evaluating Protective Merit of Coatings on Metals. *Industrial & Engineering Chemistry* **1948**, *40* (1), 161-167.
11. Kittelberger, W. W.; Elm, A. C., DIFFUSION OF SODIUM CHLORIDE THROUGH VARIOUS PAINT SYSTEMS. *Industrial & Engineering Chemistry* **1952**, *44* (2), 326-329.
12. Steinsmo, U.; Skar, J. I., Factors Influencing the Rate of Cathodic Disbonding of Coatings. **1994**, *50* (12), 934-939.
13. Keane, J. D.; Wettach, W.; Bosch, W., Minimum Paint Film Thickness for Economical Protection of Hot-Rolled Steel Against Corrosion. *J Journal of Paint Technology* **1969**. vol 41, 372-382.

14. Sørensen, P. A.; Kiil, S.; Dam-Johansen, K.; Weinell, C. E., Influence of substrate topography on cathodic delamination of anticorrosive coatings. *Progress in Organic Coatings* **2009**, *64* (2), 142-149.
15. Sørensen, P. A.; Kiil, S.; Dam-Johansen, K.; Weinell, , Anticorrosive coatings: a review. *Journal of Coating Technology and Research* **2009**, *6* (2), 135-176.
16. Zhang, X., Galvanic corrosion. *Uhlig's Corrosion Handbook* **2011**, *51*, 123.
17. Funke, W., Problems and progress in organic coatings science and technology. *Progress in Organic Coatings* **1997**, *31* (1), 5-9.
18. Ulaeto, S. B.; Rajan, R.; Pancreicious, J. K.; Rajan, T. P. D.; Pai, B. C., Developments in smart anticorrosive coatings with multifunctional characteristics. *Progress in Organic Coatings* **2017**, *111*, 294-314.
19. Kendig, M.; Mills, D. J., An historical perspective on the corrosion protection by paints. *Progress in Organic Coatings* **2016**, *102*, 53-59.
20. Montemor, M. F., Functional and smart coatings for corrosion protection: A review of recent advances. *Surface and Coatings Technology* **2014**, *258*, 17-37.

21. Arthur, D.; Jonathan, A.; Ameh, P.; Anya, C., A review on the assessment of polymeric materials used as corrosion inhibitor of metals and alloys. *Internation Journal of Industrial Chemistry* **2013**, *4* (1), 1-9.
22. Gurrappa, I.; Yashwanth, I. V. S., Chapter 2 - The Importance of Corrosion and the Necessity of Applying Intelligent Coatings for Its Control. In *Intelligent Coatings for Corrosion Control*, Tiwari, A.; Rawlins, J.; Hihara, L. H., Eds. Butterworth-Heinemann: Boston, 2015; pp 17-58.
23. Joshi, P. S.; Venkateswaran, G.; Venkateswarlu, K. S., Passivation of carbon steel alloy in de-oxygenated alkaline pH media. The effect of various additives. *Corrosion Science* **1993**, *34* (8), 1367-1379.
24. Simescu, F.; Idrissi, H., Effect of zinc phosphate chemical conversion coating on corrosion behaviour of mild steel in alkaline medium: protection of rebars in reinforced concrete. *Science and Technology of Advanced Materials* **2008**, *9* (4), 045009.
25. 2011/65/EU, E. D., The restriction of the use of certain hazardous substances in electrical and electronic equipment. In *The European Parliament and of the Council of 8 June 2011*, European Union Parliament 2011.

26. Salnikow, K.; Zhitkovich, A., Genetic and Epigenetic Mechanisms in Metal Carcinogenesis and Cocarcinogenesis: Nickel, Arsenic, and Chromium. *Chemical Research in Toxicology* **2008**, *21* (1), 28-44.
27. Satoh, N., Effects of heavy metal additions and crystal modification on the zinc phosphating of electrogalvanized steel sheet. *Surface and Coatings Technology* **1987**, *30* (2), 171-181.
28. Sankara Narayanan, T., Surface pretreatment by phosphate conversion coatings-A review. *Reviews in Advanced Materials Science* **2005**, *9*, 130-177.
29. Popić, J. P.; Jegdić, B. V.; Bajat, J. B.; Veljović, Đ.; Stevanović, S. I.; Mišković-Stanković, V. B., The effect of deposition temperature on the surface coverage and morphology of iron-phosphate coatings on low carbon steel. *Applied Surface Science* **2011**, *257* (24), 10855-10862.
30. van Ooij, W. J.; Zhu, D.; Palanivel, V.; Lamar, J. A.; Stacy, M., Overview: the potential of silanes for chromate replacement in metal finishing industries. *J Silicon Chemistry* **2006**, *3* (1-2), 11-30.
31. Van Ooij, W.; Zhu, D.; Prasad, G.; Jayaseelan, S.; Fu, Y.; Teredesai, N., Silane based chromate replacements for corrosion control, paint adhesion, and rubber bonding. *Surface Engineering* **2000**, *16* (5), 386-396.

32. Tiwari, A.; Hihara, L. H., Chapter 10 - Sol-Gel Route for the Development of Smart Green Conversion Coatings for Corrosion Protection of Metal Alloys. In *Intelligent Coatings for Corrosion Control*, Tiwari, A.; Rawlins, J.; Hihara, L. H., Eds. Butterworth-Heinemann: Boston, 2015; pp 363-407.
33. Metroke, T. L.; Parkhill, R. L.; Knobbe, E. T., Passivation of metal alloys using sol-gel-derived materials—a review. *Progress in Organic Coatings* **2001**, *41* (4), 233-238.
34. Makhlof, A. S. H., 3 - Techniques for synthesizing and applying smart coatings for material protection. In *Handbook of Smart Coatings for Materials Protection*, Woodhead Publishing: 2014; pp 56-74.
35. Baghdachi, J., Smart Coatings. In *Smart Coatings II*, American Chemical Society: 2009; Vol. 1002, pp 3-24.
36. Pilcher, G. In *Meeting the challenge of radical change: coatings R&D as we enter the 21st century*, Macromolecular Symposia, Wiley Online Library: 2002; pp 1-16.
37. Van Herk A. ,Specialty Applications of Latex Polymers. In *Chemistry and Technology of Emulsion Polymerisation*, Cap 10, 283-304.

38. Almeida, E.; Santos, D.; Fragata, F.; De La Fuente, D.; Morcillo, M., Anticorrosive painting for a wide spectrum of marine atmospheres: Environmental-friendly versus traditional paint systems. *J Progress in Organic Coatings* **2006**, *57* (1), 11-22.
39. Mircea Manea, L. K., Jörg Sanders, Organic Coating Materials. In *Anticorrosive Coatings- Fundamentals and New Concepts*, Sanders, J., Ed. Vincentz network Hanover, Germany, 2010.
40. Zhang, J.-T.; Hu, J.-M.; Zhang, J.-Q.; Cao, C.-N., Studies of water transport behavior and impedance models of epoxy-coated metals in NaCl solution by EIS. *Progress in Organic Coatings* **2004**, *51* (2), 145-151.
41. van Westing, E. P. M.; Ferrari, G. M.; de Wit, J. H. W., The determination of coating performance with impedance measurements—II. Water uptake of coatings. *Corrosion Science* **1994**, *36* (6), 957-977.
42. Aigbodion, A.; Okieimen, F.; Obazee, E.; Bakare, I., Utilisation of maleinized rubber seed oil and its alkyd resin as binders in water-borne coatings. *Progress in Organic Coatings* **2003**, *46* (1), 28-31.
43. Gonçalves, G. S.; Baldissera, A. F.; Rodrigues, L. F.; Martini, E. M. A.; Ferreira, C. A., Alkyd coatings containing polyanilines for corrosion protection of mild steel. *Synthetic Metals* **2011**, *161* (3), 313-323.

44. Weiss, K. D., Paint and coatings: A mature industry in transition. *Progress in Polymer Science* **1997**, 22 (2), 203-245.
45. Howarth, G., Polyurethanes, polyurethane dispersions and polyureas: Past, present and future. *Surface Coatings International part B: coatings transactions* **2003**, 86 (2), 111-118.
46. Koh, E.; Lee, S.; Shin, J.; Kim, Y.-W., Renewable Polyurethane Microcapsules with Isosorbide Derivatives for Self-Healing Anticorrosion Coatings. *Industrial & Engineering Chemistry Research* **2013**, 52 (44), 15541-15548.
47. Machotová, J.; Černošková, E.; Honzíček, J.; Šňupárek, J., Water sensitivity of fluorine-containing polyacrylate latex coatings: Effects of crosslinking and ambient drying conditions. *Progress in Organic Coatings* **2018**, 120, 266-273.
48. Asua, J. M., Emulsion polymerization: From fundamental mechanisms to process developments. *Journal of Polymer Science, Part A: Polymer Chemistry* **2004**, 42 (5), 1025-1041.
49. Asua, J. M., Miniemulsion polymerization. *Progress in Polymer Science* **2002**, 27 (7), 1283-1346.

50. Nguyen, T.; Bentz, D.; Byrd, E., Method for measuring water diffusion in a coating applied to a substrate. *Journal of Coatings Technology* **1995**, *67* (844), 37-46.
51. Roulstone, B.; Wilkinson, M.; Hearn, J., Studies on polymer latex films: II. Effect of surfactants on the water vapour permeability of polymer latex films. *Polymer international* **1992**, *27* (1), 43-50.
52. Aramendia, E.; Barandiaran, M. J.; Grade, J.; Blease, T.; Asua, J. M., Improving water sensitivity in acrylic films using surfmers. *Langmuir* **2005**, *21* (4), 1428-1435.
53. Liu, Y.; Soer, W.-J.; Scheerder, J. r.; Satgurunathan, G.; Keddie, J. L., Water vapor sorption and diffusion in secondary dispersion barrier coatings: A critical comparison with emulsion polymers. *ACS Applied Materials & Interfaces* **2015**, *7* (22), 12147-12157.
54. Jiang, B.; Tsavalas, J. G.; Sundberg, D. C., Water whitening of polymer films: Mechanistic studies and comparisons between water and solvent borne films. *Progress in Organic Coatings* **2017**, *105*, 56-66.
55. Mistry, J. K., Ironing out stains. *European Coating Journal* **2008**, Vol. 12.

56. Chimenti, S.; Vega, J. M.; Aguirre, M.; García-Lecina, E.; Díez, J. A.; Grande, H.-J.; Paulis, M.; Leiza, J. R., Effective incorporation of ZnO nanoparticles by miniemulsion polymerization in waterborne binders for steel corrosion protection. *Journal of Coatings Technology and Research* **2017**, *14* (4), 829-839.
57. *Chapter 28- Protective Coatings and Inorganic Anti-Corrosion Pigments, Paint and Coating Testing Manual, Philadelphia, PA.* 14th Edition ed.; American Society of Testing and Materials: 1995; Vol. 20, p 282-299.
58. Shi, X.; Nguyen, T. A.; Suo, Z.; Liu, Y.; Avci, R., Effect of nanoparticles on the anticorrosion and mechanical properties of epoxy coating. *Surface and Coatings Technology* **2009**, *204* (3), 237-245.
59. Choudalakis, G.; Gotsis, A. D., Permeability of polymer/clay nanocomposites: A review. *European Polymer Journal* **2009**, *45* (4), 967-984.
60. Xu, B.; Zheng, Q.; Song, Y.; Shangguan, Y., Calculating barrier properties of polymer/clay nanocomposites: Effects of clay layers. *Polymer* **2006**, *47* (8), 2904-2910.
61. Sridhar, L. N.; Gupta, R. K.; Bhardwaj, M., Barrier Properties of Polymer Nanocomposites. *Industrial & Engineering Chemistry Research* **2006**, *45* (25), 8282-8289.

62. Zubielewicz, M.; Gnot, W., Mechanisms of non-toxic anticorrosive pigments in organic waterborne coatings. *Progress in Organic Coatings* **2004**, *49* (4), 358-371.
63. Sangaj, N. S.; Malshe, V. C., Permeability of polymers in protective organic coatings. *Progress in Organic Coatings* **2004**, *50* (1), 28-39.
64. Lange, J.; Wyser, Y., Recent innovations in barrier technologies for plastic packaging—a review. *Packaging Technology and Science* **2003**, *16* (4), 149-158.
65. Weinkauff, D. H.; Paul, D. R., Effects of Structural Order on Barrier Properties. In *Barrier Polymers and Structures*, American Chemical Society: 1990; Vol. 423, pp 60-91.
66. Wolf, C.; Angellier-Coussy, H.; Gontard, N.; Doghieri, F.; Guillard, V., How the shape of fillers affects the barrier properties of polymer/non-porous particles nanocomposites: A review. *Journal of Membrane Science* **2018**, *556*, 393-418.
67. Knudsen, O. Ø.; Steinsmo, U., Effect of Barrier Pigments on Cathodic Disbonding. *Journal of Corrosion Science Engineering* *2*, 50-1.

68. Nikraves, B.; Ramezanzadeh, B.; Sarabi, A.; Kasiriha, S., Evaluation of the corrosion resistance of an epoxy-polyamide coating containing different ratios of micaceous iron oxide/Al pigments. *Corrosion Science* **2011**, *53* (4), 1592-1603.
69. Giúdice, C. A.; Benítez, J. C., Optimising the corrosion protective abilities of lamellar micaceous iron oxide containing primers. *Anti-Corrosion Methods Materials* **2000**, *47* (4), 226-232.
70. Kalenda, P.; Kalendová, A.; Štengl, V.; Antoš, P.; Šubrt, J.; Kváča, Z.; Bakardjieva, S., Properties of surface-treated mica in anticorrosive coatings. *Progress in Organic Coatings* **2004**, *49* (2), 137-145.
71. Kalendová, A., Effects of particle sizes and shapes of zinc metal on the properties of anticorrosive coatings. *Progress in Organic Coatings* **2003**, *46* (4), 324-332.
72. Bajat, J.; Kačarević-Popović, Z.; Mišković-Stanković, V.; Maksimović, M., Corrosion behaviour of epoxy coatings electrodeposited on galvanized steel and steel modified by Zn–Ni alloys. *Progress in Organic Coatings* **2000**, *39* (2-4), 127-135.

73. Boshkov, N.; Petrov, K.; Raichevski, G., Corrosion behavior and protective ability of multilayer Galvanic coatings of Zn and Zn–Mn alloys in sulfate containing medium. *Surface*

Coatings Technology **2006**, *200* (20-21), 5995-6001.

74. King, A.; Scully, J., Sacrificial anode-based galvanic and barrier corrosion protection of 2024-T351 by a Mg-rich primer and development of test methods for remaining life assessment. *Corrosion* **2011**, *67* (5), 055004-1-055004-22.

75. Kalendova, A., Mechanism of the action of zinc-powder in anticorrosive coatings. *Anti-corrosion methods materials* **2002**, *49* (3), 173-180.

76. Nabih, N.; Herrmann, U.; Glasser, G.; Lieberwirth, I.; Landfester, K.; Taden, A., Water-based hybrid zinc phosphate-polymer miniemulsion as anticorrosive coating. *Progress in Organic Coatings* **2013**, *76* (4), 555-562.

77. Yang, Y.; Scantlebury, J.; Koroleva, E.; Ogawa, O.; Tanabe, H., A Novel Anti-corrosion Calcium Magnesium Polyphosphate Pigment and Its Performance in Aqueous Solutions on Mild Steel when Coupled to Metallic Zinc. *ECS Transactions* **2010**, *24* (1), 163-183.

78. Williams, G.; McMurray, H.; Grace, R., Inhibition of magnesium localised corrosion in chloride containing electrolyte. *Electrochimica Acta* **2010**, *55* (27), 7824-7833.
79. De, L. H. K., US3034210A- Inhibition of corrosion of magnesium. 1962.
80. Del Amo, B.; Romagnoli, R.; Vetere, V.; Hernández, L., Study of the anticorrosive properties of zinc phosphate in vinyl paints. *Progress in Organic Coatings* **1998**, *33* (1), 28-35.
81. Sinko, J., Challenges of chromate inhibitor pigments replacement in organic coatings. *Progress in Organic Coatings* **2001**, *42* (3-4), 267-282.
82. Del Amo, B.; Romagnoli, R.; Deyá, C.; González, J., High performance water-based paints with non-toxic anticorrosive pigments. *Progress in Organic Coatings* **2002**, *45* (4), 389-397.
83. Grundmeier, G.; Rossenbeck, B.; Roschmann, K. J.; Ebbinghaus, P.; Stratmann, M., Corrosion protection of Zn-phosphate containing water borne dispersion coatings. *Corros. Sci.* **2006**, *48* (11), 3716-3730.
84. [US], L. C.-T. Additive package for in situ phosphatizing paint, paint and method 1994.

85. Reyes, Y.; Rodriguez, F. J.; del Rio, J. M.; Corea, M.; Vazquez, F., Characterisation of an anticorrosive phosphated surfactant and its use in waterborne coatings. *Progress in Organic Coatings* **2005**, *52* (4), 366-371.
86. Gonzalez, I.; Mestach, D.; Leiza, J. R.; Asua, J. M., Adhesion enhancement in waterborne acrylic latex binders synthesized with phosphate methacrylate monomers. *Progress in Organic Coatings* **2008**, *61* (1), 38-44.
87. Boinovich, L. B.; Emelyanenko, A. M., Hydrophobic materials and coatings: principles of design, properties and applications. *Russian Chemical Review*, **2008**, *77* (7), 583-600.
88. de Leon, A.; Advincula, R. C., Chapter 11 - Conducting Polymers with Superhydrophobic Effects as Anticorrosion Coating. In *Intelligent Coatings for Corrosion Control*, Tiwari, A.; Rawlins, J.; Hihara, L. H., Eds. Butterworth-Heinemann: Boston, 2015; pp 409-430.
89. Ionov, L.; Synytska, A., Self-healing superhydrophobic materials. *Physical Chemistry Chemical Physics* **2012**, *14* (30), 10497-10502.
90. de Leon, A. C. C.; Pernites, R. B.; Advincula, R. C., Superhydrophobic colloiddally textured polythiophene film as superior anticorrosion coating. *ACS Applied Materials*

interfaces **2012**, 4 (6), 3169-3176.

91. Xu, L.; He, J., Fabrication of Highly Transparent Superhydrophobic Coatings from Hollow Silica Nanoparticles. *Langmuir* **2012**, 28 (19), 7512-7518.

92. Cohen, N.; Dotan, A.; Dodiuk, H.; Kenig, S., Superhydrophobic Coatings and Their Durability. *Materials and Manufacturing Processes* **2016**, 31 (9), 1143-1155.

93. López, A. B.; de la Cal, J. C.; Asua, J. M., Highly Hydrophobic Coatings from Waterborne Latexes. *Langmuir* **2016**, 32 (30), 7459-7466.

94. López, A. B.; de la Cal, J. C.; Asua, J. M., Controlling film topography to form highly hydrophobic waterborne coatings. *Soft Matter* **2016**, 12 (33), 7005-7011.

95. Haiyan, J.; Lifan, H.; Xiaoyu, L., Synthesis of Styrene-Acrylate Emulsion and Its Application in Waterborne Antirust Coatings *Paint Coatings Industry* **2007**, 9.

96. Electrochemical Impedance Spectroscopy Investigation of the Corrosion Resistance of a Waterborne Acrylic Coating Containing Active Electrochemical Pigments for the Protection of Carbon Steel. **2014**.

97. Steele, A.; Bayer, I.; Loth, E., Adhesion strength and superhydrophobicity of polyurethane/organoclay nanocomposite coatings. *Applied Polymer Science part A* **2012**, *125* (S1), E445-E452.
98. López, A. B.; de la Cal, J. C.; Asua, J. M. Waterborne Fluoropolymer Dispersion For Super-Hydrophobic coatings. Thesis UPV/EHU, POLYMAT, 2016.
99. Commission, E., Amending Annex XVII to regulation (EC) No 1907/2006 regard perfluorinated acid(PFOA), its salt and PFOA-related substances. In *Official Journal of the European Union*, 2017.

Chapter 2

In-situ phosphatization and enhanced corrosion properties of films made of phosphate functionalized nanoparticles

Part of this chapter has been included in an international patent application (PCT/EP-2019/052860) entitled "**A Method for Providing Coating Systems with Corrosion-Protective Properties**".

Chapter 2

2.1	Introduction	43
2.2	Synthesis of phosphated Poly (MMA-co-BA) waterborne dispersions	46
2.3	Polymerization kinetics and evolution of particles size	48
2.4	Latex application on steel substrate	50
2.4.1	In-situ phosphatization and influence of drying conditions	50
2.4.2	Characterization of the in-situ phosphatization	55
2.5	In-situ phosphatization and anticorrosion protection	67
2.6	Conclusions	73
2.7	References	75

2.1 Introduction

As already mentioned in Chapter 1, although the interest towards waterborne coatings has increased in the last decades due to their sustainability¹⁻³, good film formation and weatherability⁴⁻⁶, solventborne systems have the hegemony in the field of corrosion protective coatings. In fact, since waterborne coatings present worse water resistant properties, compared to their solvent based counterparts, solventborne coatings remain the preferred choice in corrosion protection (they continue to offer exceptional barrier performances in a wide range of environmental conditions).

In films cast from waterborne latexes, the presence of surfactants or salts, that are not totally exuded during the film formation, cause higher diffusion of water through the film and impair the ability to prevent the corrosion⁷⁻¹². Nevertheless, as showed in literature, the reduction of water sensitivity can be partially overcome by incorporating polymerizable surfactants in the latex formulation^{9, 10, 13}.

Another drawback of waterborne coatings for corrosion protection that is worth considering is the flash rust corrosion¹⁴. This phenomenon appears quickly, especially when thin water films reside on the metal surface triggering the corrosive action. Due to that, in order to prevent flash rust corrosion from taking place^{15, 16}, unlike in solventborne systems, conversion coating layers are always considered in the design of the protective coatings based on waterborne binders. Some attempts to design a

waterborne primer with a built-in conversion coating have been done to reduce the number of layers. Lin et al. have reported an in-situ phosphatizing system in which a phosphatizing agent is pre-mixed with the coating¹⁷. An alternative is to incorporate the phosphate functionality into the resin in the form of surfactant¹⁸ or monomer¹⁹. Although better adhesion has been reported, none of these systems has demonstrated to be able to protect the metal substrate in formulations without anti-corrosion pigments. Some stand-alone single layered epoxy barrier coatings with thicknesses in the range of 250 μm have been studied and reported in literature^{20,21}. However, in these cases, anticorrosion inhibitor pigments were always mixed with the polymer and in some cases they could trigger the degradation of the polymeric matrices²².

In the present chapter, we attempt to develop a thin stand-alone single layered barrier coating by synthesizing a versatile waterborne binder (which fulfills the environmental standard established related to VOCs levels), with multifunctional capabilities such as metal/coating interface adhesion/passivation and barrier protection, typical of a conversion coating and primer-topcoat respectively, and that is able to protect the metal substrate without the aid of any corrosion inhibitors. A waterborne polymeric dispersion, made of methyl methacrylate (MMA) and n-butyl acrylate (BA) copolymer containing phosphated functionalities has been synthesized using a phosphated surfmer.

Polymerizable surfactants have been extensively used in emulsion polymerization, however it is important to consider that their correct selection is strongly related to the process and to the (co)monomers used^{23, 24}. The position (in the hydrophilic or hydrophobic part) or the reactivity of the double bond can lead to different final latexes. On the one hand the location of the double bond can affect the surface properties of the polymerizable surfactant as well as the CMC^{25, 26}. On the other hand, different reactivities influence the stabilization efficiency; in fact, very reactive double bonds can lead to the formation of polyelectrolytes soluble in the aqueous phase that deprive the latex from stabilizing groups or also can be buried if incorporated to the particles²⁷. In this work Sipomer PAM200 (labelled SIP) was used as polymerizable surfactant and its structure is presented in Figure 2.1.

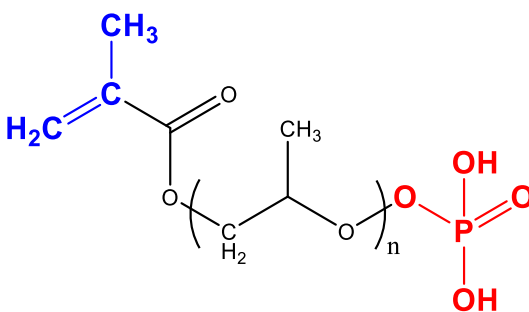


Figure 2.1. Chemical structure of Sipomer PAM200.

SIP presents a methacrylic function that has moderate reactivity with methyl methacrylate and butyl acrylate and that is located in the hydrophobic part of the

surfactant (polypropylene oxide chain extender). These properties allow an efficient incorporation of the surfactant in the polymer backbone and provide efficient stabilization of the aqueous dispersion. The hydrophilic part is represented by the phosphate group which also provides the phosphatization ability.

The optimal drying conditions that lead to in-situ phosphatization of the metal-coating interface have been investigated and the mechanism behind the provided anticorrosion protection has been evaluated in both mild (NaCl 3.5 wt% solution) and harsh corrosive environments (salt-spray exposure to 5 wt% NaCl salty fog), respectively. The performance of these binders was compared with a binder synthesized using conventional anionic surfactant. For all the tested samples, electrochemical impedance spectroscopy (EIS) has been used as non-destructive test to monitor the evolution of the coating with time.

2.2 Synthesis of phosphated Poly (MMA-co-BA) waterborne dispersions

All the latexes were synthesized by seeded semibatch emulsion polymerization and the recipes are summarized in Tables 2.1 and 2.2. The synthesis of the seed (labeled MB) with a solids content of 13 %, was carried out in a 1L glass-jacketed reactor (equipped with reflux condenser, feeding and sampling outlet and stainless steel

impeller rotating at 200 rpm) under a N₂ atmosphere at 70 °C in semibatch conditions by feeding the monomer during 4 hours and allowing the latex to react for one more hour under batch conditions (Table 2.1). Stable Poly (MMA-co-BA) seed latex with 13 % of solids content and average particle size of 65 nm was successfully synthesized by semibatch emulsion polymerization and then used for the synthesis of the final waterborne MB acrylic dispersions. Poly (MMA-co-BA) latexes with 50% of solids content and theoretical particle size of 181 nm were synthesized by seeded semibatch emulsion polymerization using conventional or polymerizable surfactants (latexes labeled MB_D and MB_S). In detail, the experimental procedure to achieve a latex of 50 % solids content was as follows; the seed was added into the reactor and heated up to the target reaction temperature of 70 °C. Once the temperature was reached, the initiator (KPS) was added and a monomer preemulsion (containing the monomers, water and Sipomer PAM200 (SIP) or Dowfax 2A1 (DOW)) was fed to the reactor for 4 hours. pH neutralization, by addition of ammonia solution, of the preemulsion containing SIP was necessary to incorporate the surfmer into the system, as very acid or very basic conditions would hydrolyze the ester linkage of the phosphate group. Upon finishing the feeding, the reaction was post-polymerized for one hour to reduce the amount of unreacted monomers. The latex synthesized with SIP is labeled as MB_S and the one with DOW as MB_D (see Table 2.2).

Table 2.1. *MB seed formulation.*

Reagent	Initial load(g)	Stream (g)
MMA	-	31.3
BA	-	31.3
Water	436.7	-
DOW	0.630	-
KPS	0.313	-
NaHCO ₃	1.035	-

Table 2.2. *Formulation used to synthesize MB_S and MB_D waterborne binders.*

LATEX	MB (seed)(g)	MMA(g)	BA(g)	KPS(g)	DOW(g)	SIP(g)	Water(g)	S.C.(%)
MB_S	107	119	119	0.313	/	5	149.77	50
MB_D	107	119	119	0.313	5	/	149.77	50

2.3 Polymerization kinetics and evolution of particles size

Despite the use of a surfmer can result in surfactant burial or formation of oligomers in the aqueous phase ^{13, 23} with consequent emulsion destabilization, SIP was

successfully incorporated in the final latex obtaining particle sizes close to the target one. In fact, the particle size evolution during the reaction fits very well with the theoretical one that assumes negligible secondary nucleation or coagulation (Figure 2.2). In addition, the use of polymerizable surfactant (SIP) had not remarkable effects on the polymerization kinetics. The evolution of the instantaneous conversion of the latexes using Dowfax (MB_D) and Sipomer (MB_S) surfactants measured gravimetrically, is plotted in Figure 2.3. Starved conditions (conversion higher than 90%) were obtained in the second stage of the process and the different surfactants, used in the second stage, hardly affected the kinetics of the polymerization.

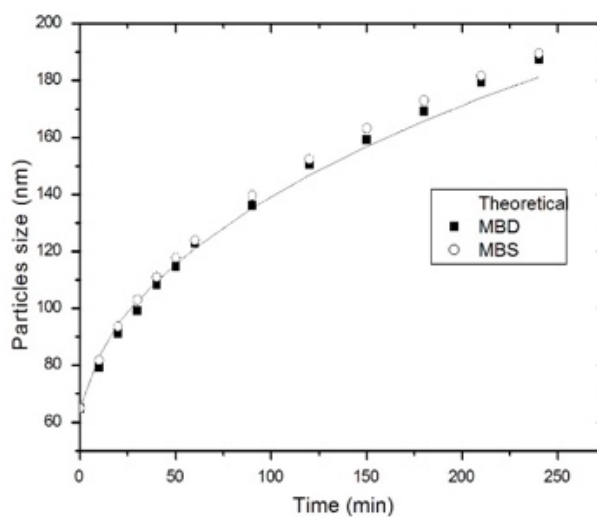


Figure 2.2. Time evolution of particle diameter during the synthesis of MB_D and MB_S latexes.

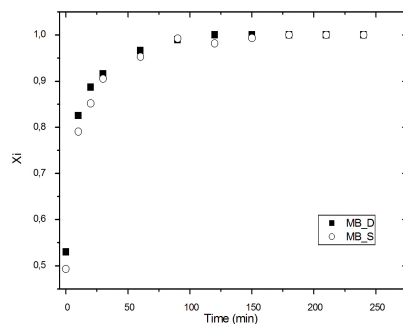


Figure 2.3. Time evolution of the instantaneous conversion for the experiments *MB_S* and *MB_D*.

2.4 Latex application on steel substrate

2.4.1 In-situ phosphatization and influence of drying conditions

In order to evaluate the anticorrosion performance, *MB_D* and *MB_S* latexes were applied, at 23 °C and 60% of relative humidity (RH), on steel substrates, previously cleaned, and the resulting coatings are shown in Figure 2.4. As it can be seen, when *MB_D* was cast, brownish non-homogeneous stains (Figure 2.4a), typical of flash rust, appeared on the steel surface. Indeed, sulfonate groups (belonging to the anionic surfactant Dowfax), in presence of water, can interact with the metal substrate forming iron complexes typically called green rust²⁸⁻³⁰. On the other hand, when *MB_S* binder was used (Figure 2.4b), a homogeneous yellowish stain appeared on the surface of the

steel, presumably due to the interaction between the phosphate groups of the latex and the steel surface. The probable explanation behind this effect is the strong interfacial acid-base interactions of $\text{PO}^{\text{m-}}$ groups with the $\text{Fe}^{\text{n+}}$ ³¹. In fact, at neutral pH conditions, orthophosphate ions (RHPO_4^- and RPO_4^{2-}) may interact with the hydroxyl groups present on the metal surface, forming a dense and thin iron phosphate passivating layer (Figure 2.5).

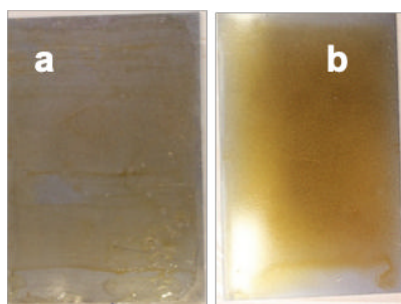


Figure 2.4. *Steel substrates coated with MB_D (a) and MB_S (b) at 23 °C and RH= 60%.*

However, it has to be pointed out that this phenomenon was severely affected by the drying conditions. Figure 2.6 presents the different coatings obtained when the latex was cast on steel substrates at different drying conditions, namely maintaining constant the drying temperature at 23 °C and changing the relative humidity (RH %) from 30% to 60%.

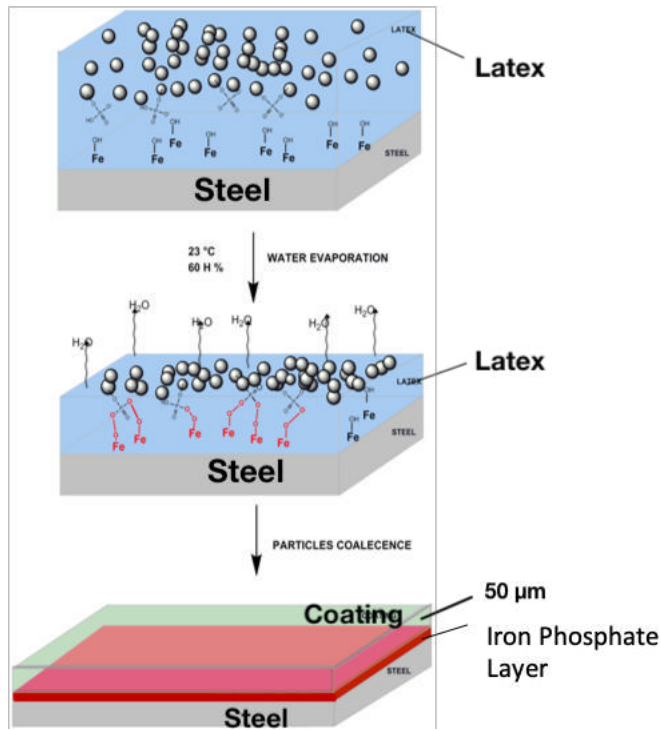


Figure 2.5. Schematic drawing of the in-situ phosphatization mechanism during latex film formation.

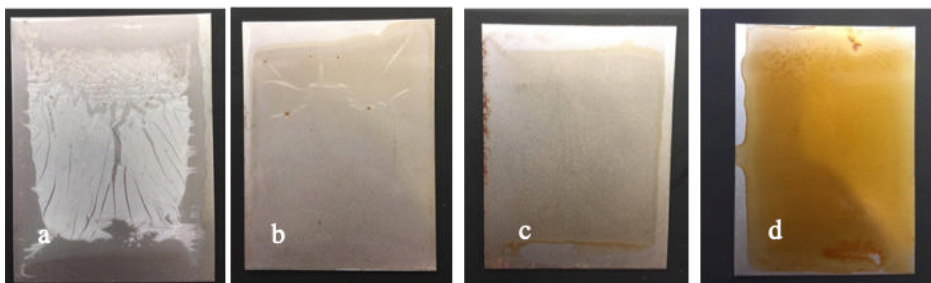


Figure 2.6. MB_S cast on steel substrates at different drying conditions; $T=23\text{ }^{\circ}\text{C}$ (constant), a) $RH=30\%$, b) $RH=43\%$, c) $RH=50\%$, d) $RH=60\%$.

According to the film formation mechanism³², during the water evaporation, latex particles pack, deform and eventually coalesce. Depending on the latex composition (e.g. monomers and surfactants), substrate, temperature of drying and the rate at which water evaporation occurs, different qualities of films can be obtained. In our study the drying temperature was maintained at a constant value of 23 °C, low enough to avoid the formation of superficial defects, related to a drastic evaporation of the water, and to avoid the skin layer formation, due to the faster evaporation of water compared to particles diffusion.

The drying rate was changed by means of variations of relative humidity (RH). As it can be seen in Figure 2.6, in-situ phosphatization with a good film formation was favored by decreasing drying rates (best layers obtained at 60% RH). At higher drying rate (RH < 60%) the phosphatization did not have enough time to occur (Figure 2.6b and 2.6c). Moreover, if the RH was reduced to 30%, the film formation was affected as confirmed by the presence of fractures on the film surface. This observation might indicate that above 60% RH (where good films are obtained) a deformation by wet or capillary sintering occurs, which is avoided when water evaporation is too fast (30% RH).

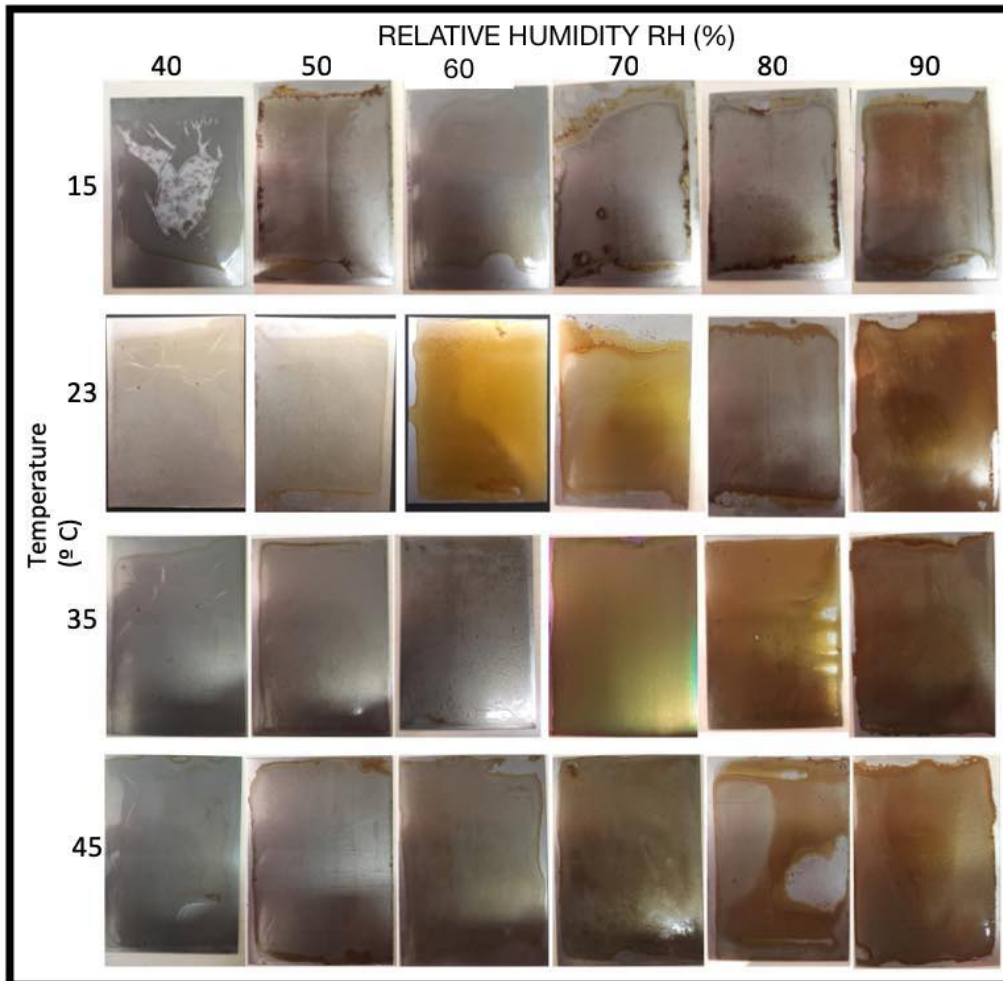


Figure 2.7. *MB_S* cast on steel substrates at different drying conditions; $T=15, 23, 35, 45$ °C and $RH=40, 50, 60, 70, 80, 90$ %.

Due to the evident key role of the drying conditions on the extent of phosphatization, film formation and flash rust, the application of MB_S latex on steel substrate under a

wider range of temperatures (15, 23, 35 and 45 °C) and relative humidities (40, 50, 60, 70, 80 and 90 %) was also implemented in this study (Figure 2.7).

On the one hand, at $RH < 60\%$ the evaporation of water from the latex is fast enough to prevent, in all the samples, the interaction between the hydroxyl groups (belonging to the metal surface) with the surrounding reactive species (H_2O , O_2 and PO^{m-}), which means that neither phosphatization nor flash rust at the coating-substrate interface occurred. On the other hand, at $RH > 70\%$, due to the lower drying rate, the prolonged contact between the water and the metal substrate triggered the formation of rust at the interface, which is confirmed by the characteristic dark-brownish color. Moreover, it is worth to mention that the higher the drying temperature the higher the extent of rust formation; for instance, at 45 °C rust formed at already 60 % of relative humidity. Regarding the phosphatization, the optimal drying range to produce it was confined within a temperature comprised between 23 and 35 °C and RH comprised between 60 and 70 %.

2.4.2 Characterization of the in-situ phosphatization

The interface morphology, composition and texture of the coating formed on steel can be effectively studied by scanning electron microscope (SEM) assisted with energy dispersive X-ray analysis (EDX) for the films cast at different drying rates. For

comparison purpose, Figure 2.8 shows an example of a clean steel surface (2.8a) and some examples of rust morphology (2.8 b, c and d). These micrographs were collected in the early stage of this work, with the purpose of identifying the different morphology of iron oxides produced during the corrosion of bare steel after immersion in 3.5 wt % NaCl solution, in order to compare them with those already characterized by several authors and commonly found in real applications. As depicted in Figure 2.8b, rusted steel is characterized by the presence of different iron oxides to which characteristic morphologies are associated; some of them are represented in Figures 2.8c and d.

Misawa et al.³³ first investigated the mechanism of rust formation on steel substrates in aqueous solution and identified several iron oxyhydroxide and oxides as rust constituents. The main phases reported were γ -FeOOH (Lepidocrocite), α -FeOOH (Goethite) and Fe_3O_4 (Magnetite). γ -FeOOH is usually formed in the early stages of corrosion and then it is transformed into α -FeOOH at longer exposition time.

Moreover, it has been seen that in the presence of high humidity ($\text{RH} > 60\%$), the reduction of γ -FeOOH can result in the formation of $\text{Fe}(\text{OH})_2$ which can convert into Fe_3O_4 after dehydration. These phases present typical morphologies; for instance, γ -FeOOH appears like small crystalline globules (sandy crystals) and an example is depicted in Figure 2.8d. The α -FeOOH looks like globular structures, called cotton balls (semicrystalline goethite), interconnected by formations as nests or even like

acicular structures (crystalline goethite) and it is represented in Figure 2.8c. The Fe_3O_4 comes out as flat regions, with circular disks.

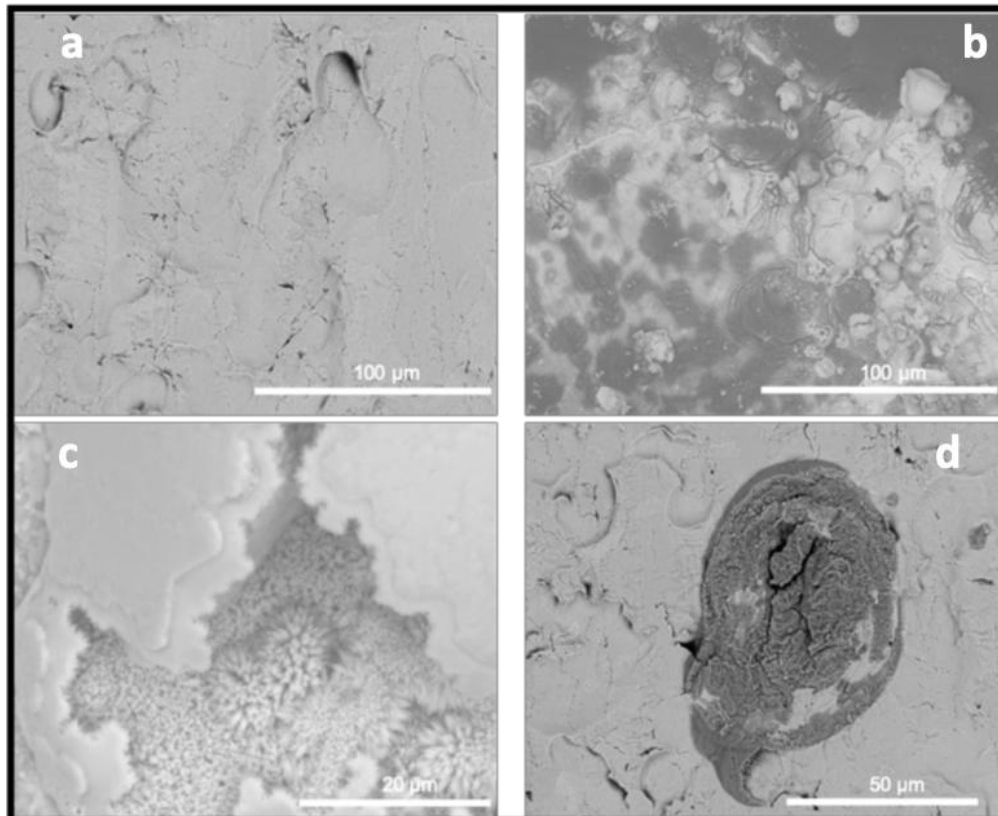


Figure 2.8. SEM micrographs of different type of morphologies found on steel substrates; a) clean steel surface b) rusted steel surface c) Goethite d) Lepidocrocite after immersion in NaCl 3.5 wt% solution.

For a better understanding of the following analysis, Table 2.3 displays the weight % average composition in oxygen, iron and hydrogen for the above-mentioned species formed from iron oxidation.

Table 2.3. *Elemental weight % composition of hydroxides and oxides characteristic of iron rust.*

Compound	Elemental composition (wt%)		
	Fe	O	H
FeOOH	63	36	1
Fe(OH) ₂	62	35,5	1,5
Fe ₃ O ₄	72	28	/

In this work the morphology and the elemental composition of the coating-substrate interface has been investigated by detaching the coating after its application onto steel substrate. This was achieved by dipping the coated steel specimen in liquid N₂ and removing the polymeric coating from the substrate without damaging neither the metal nor the coating surface (see detailed information in the Appendix II.12). For all the film samples, only the surface of the detached coating at the coating/steel interface (for simplicity it will be referred as coating surface) and the surface of the steel will be analysed by SEM/EDX after detaching the coating (Figure 2.9).

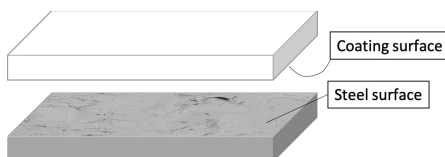


Figure 2.9. Schematic representation of the analyzed specimen surfaces.

After detaching the MB_S film dried at low rates ($T= 23\text{ }^{\circ}\text{C}$ and $\text{RH}=60\%$), the steel surface resulted rust-free, which is confirmed visually (Figure 2.10) and by the elemental composition analysis (EDX) (Figure 2.11). The oxygen peak centered at 0.53 KeV had lower intensity than the iron's peak at 0.7 KeV and the composition showed a Fe/O ratio of 92/8 which is consistent with the absence of rust (see Table 2.3). However, contrary to our expectations, the EDX spectra did not show any characteristic peak for phosphorus atoms and hence any signs of the presence of iron phosphate layer. Nevertheless, evidences of steel phosphatization were found in the analysis of the coating surface of MB_S. In fact, the iron mapping, represented in Figure 2.12, surprisingly shows the presence of Fe atoms on all the analyzed area. In the EDX spectra (Figure 2.13) the characteristic peaks of iron, centered at 0.7, 6.2 and 7.0 KeV, are clearly visible. This suggests that the superficial iron is covalently bonded to the coating surface and when the coating is detached from the steel surface, the iron phosphates stay attached to the polymeric coating. For the latex cast at higher drying rate ($T= 23\text{ }^{\circ}\text{C}$ and $\text{RH} = 43\%$), no peaks of iron were detected in the EDX spectrum

of the coating surface (Figure 2.14 and 2.15), confirming that drying conditions play a key role in the generation of the iron phosphate layer. According to these results, it is evident that lower drying rates allowed the formation of more homogeneous films and promote the strong interaction of the phosphate groups of the surfactant with the substrate.

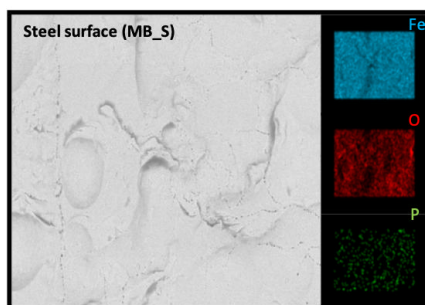


Figure 2.10. SEM micrograph and EDX elemental mapping (for Fe, O and P atoms) of steel surface after detaching MB_S coating.

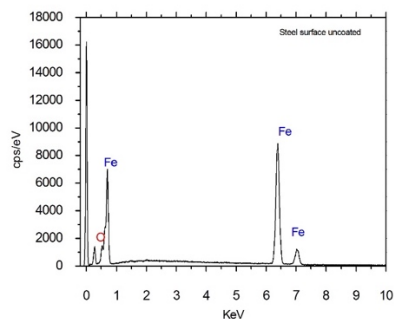


Figure 2.11. EDX spectrum of steel surface after detaching MB_S coating.

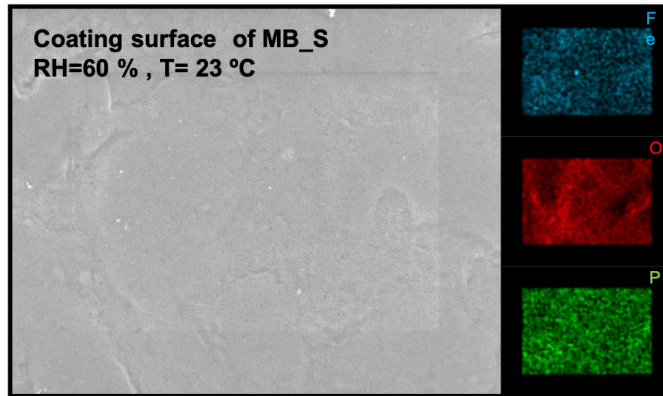


Figure 2.12. SEM micrograph and EDX elemental mapping (for Fe, O and P atoms) of the coating surface after detaching MB_S dried at RH=60 % and 23 °C.

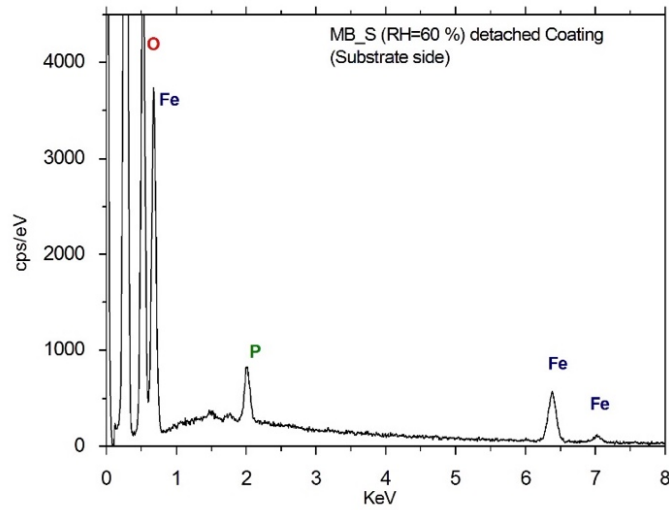


Figure 2.13. EDX spectra of the coating surface after detaching MB_S dried at RH=60 % and 23 °C.

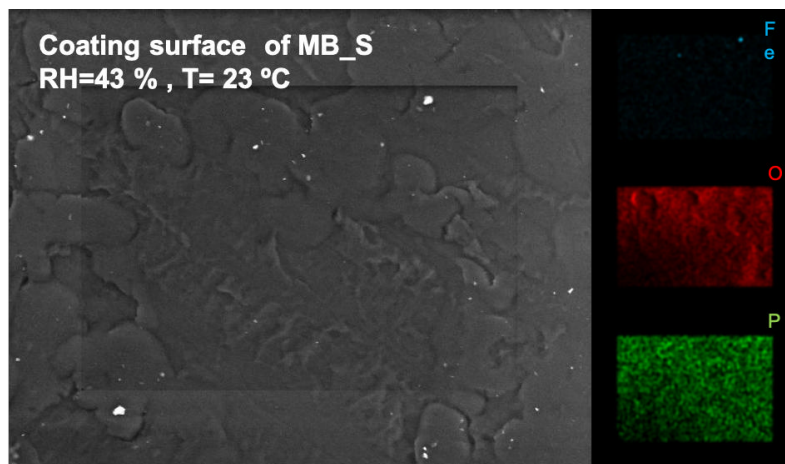


Figure 2.14. SEM micrograph and EDX elemental mapping (for Fe, O and P atoms) of the coating surface after detaching MB_S dried at RH=43% and 23 °C.

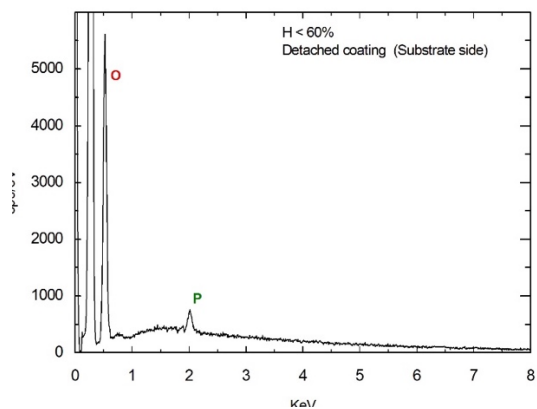


Figure 2.15. EDX spectrum of the film surface at the coating-steel interface after detaching MB_S at RH=43% and 23 °C.

The same analysis was carried out for a steel surface of the specimen coated with a film cast from MB_D latex. The EDX spectrum of the coating surface was analogous

to the detached film cast from MB_S dried at higher drying rate (RH<60 %), but without the peak of phosphorus atoms. For the sake of brevity, it is not reported here. On the other hand, it is worth to analyze the steel surface after detaching MB_D coat. As it can be seen in Figure 2.16, the SEM micrograph shows a grain-like agglomerate that resembles the morphology of Lepidocrocite (γ -FeOOH) previously showed in Figure 8d. This finding suggests the formation of flash rust which is also confirmed in the EDX spectra, reported in Figure 2.17, by the higher intensity of the O peak (0.53 KeV) with respect to the one of Fe (0.7 KeV). The elemental composition extrapolated from the spectrum in Figure 2.17 showed a Fe/O ratio of 61/39, which is consistent with the FeOOH composition listed in Table 2.3.

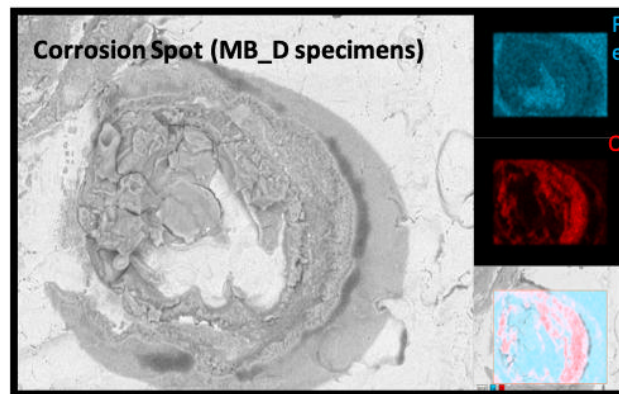


Figure 2.16. SEM micrograph and EDX elemental mapping (for Fe, O and P atoms) of a corrosion spot found on steel surface after detaching MB_D coating.

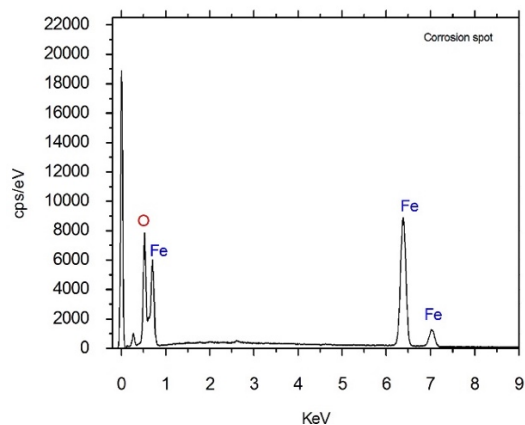


Figure 2.17. EDX spectra of a corrosion spot found on steel surface after detaching MB_D coating.

Additional evidence of the in-situ phosphatization was provided by FTIR analysis of the coatings, cast from MB_S, within the range of 400-4000 cm^{-1} . Figure 2.19 shows the FTIR absorption spectra of the surface of the detached coating, cast from MB_S under low drying rate (RH=60%), at the coating-air (a) and coating-steel (b) surface respectively (Figure 2.18)

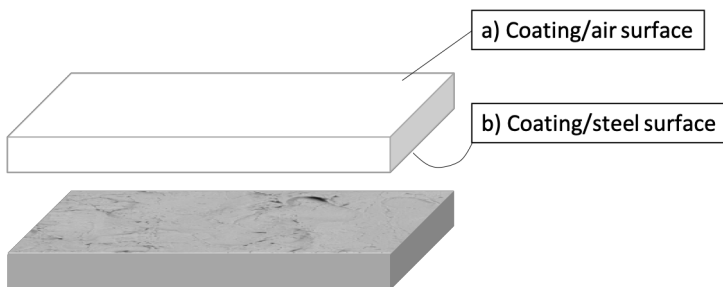


Figure 2.18. Schematic representation of the analyzed specimens surfaces by FTIR.

At first glance, the difference in composition between the coating-air and the coating-steel interface was indicated in the spectrum b) by the stretching and bending vibrations bands of water molecules at 3300-3400 cm^{-1} and 1600 cm^{-1} respectively³⁴⁻³⁶. These bands suggest the presence of chemisorbed water at the coating-steel substrate which is consistent with the formation of iron phosphate layer. In fact, it is reported in literature that the iron phosphate is generally produced in its hydrated forms such as Hureaulite ($\text{Fe}_3\text{H}_2(\text{PO}_4)_4 \cdot 4\text{H}_2\text{O}$) or Strengite ($\text{FePO}_4 \cdot 2\text{H}_2\text{O}$)³⁷. In the low wavenumber region of both spectra a) and b) (from 1100 to 400 cm^{-1}), we identify internal modes of phosphates anions that belong to the phosphate group of SIP; namely the symmetric stretching vibration at 900 cm^{-1} , the asymmetric stretching in the regions of 990-1000 cm^{-1} (Figure 2.19) and the symmetric bending at 430-510 cm^{-1} (Figure 2.20)³⁴⁻³⁸. However, the presence of Fe in the coating at the coating-steel surface (spectrum b, Figure 2.20) is corroborated by the formation of new absorption bands in the region of 430-510 cm^{-1} ; a shoulder at 430 cm^{-1} which was assigned to Fe-O bending vibration, and the peaks at 455 cm^{-1} and 495 cm^{-1} that were induced by the correlation effect of Fe-O units with phosphate anions^{35,38}. Furthermore, the peak at 620 cm^{-1} (spectrum b), that partially overlap the doublet at 620-630 cm^{-1} (assigned to C-O and C=O vibrations out of the plane³⁹), was assigned to the stretching vibration of Fe-O³⁶. Same analysis was carried out for MB_S coating dried at high drying rate (RH=43%). According to

our expectation, the spectra of the film surface at the coating-air and coating-steel surfaces were pretty much the same one to each other confirming the absence of the iron phosphate layer (see Appendix III.2).

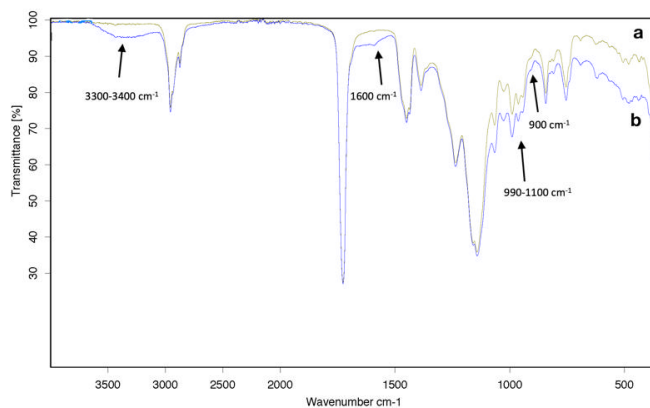


Figure 2.19. FTIR spectra of the MB_S (dried at RH=60%) surface at a) coating-air interface and at b) coating-steel interface.

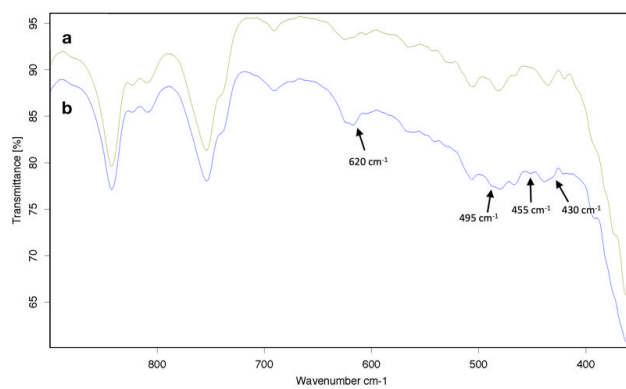


Figure 2.20. FTIR spectra at high wavenumber region of the MB_S (dried at RH=60%) surface at a) coating-air surface and at b) coating-steel surface.

2.5 In-situ phosphatization and anticorrosion protection

Electrochemical impedance spectroscopy (EIS) was used to evaluate the corrosion protection of the synthesized latexes on the coated steel. The effect of phosphatization (mediated by interaction between polymer particles and steel surface), coating thickness and drying conditions were investigated. Table 2.4 summarizes the impedance modulus values ($|Z|$ at 10^{-2} Hz, collected after 500 h of immersion in 3.5 wt% NaCl solution) obtained from Figure 2.21a, where the Bode plots for MB_D and MB_S, dried at different conditions, are presented. Bare steel was used as reference. MB_S1, MB_S2 and MB_S3 are films dried at the different drying conditions and with different thicknesses. It is worth to point out that values of impedance modulus of $10^9 \Omega \text{ cm}^2$ or higher represent the maximum values achievable by the instrument.

At first glance, all the coatings show great corrosion protection due to the capacitive behavior, with impedance modulus values higher than $10^9 \Omega \text{ cm}^2$ compared to that of bare steel at $10^3 \Omega \text{ cm}^2$. The former systems show a single time constant whilst the later shows two-time constants; although the second one is not well defined at low frequencies (Figure 2.21b). Usually, the medium-low frequency window (from 1 to 10^{-3} Hz) provides information of the coating/metal interface (e.g. charge transfer resistance and double layer capacitance related to the corrosion process, oxide resistance and capacitance related to passivation of the interface, etc.), while the high

frequency range (from 10^5 to 1 Hz) provides information of the barrier response of the coating^{40,41}. Considering the low frequency range, the impedance modulus was similar for all coatings and substantially higher than the reference substrate (more than 6 orders of magnitude higher than bare steel). None of the coatings cast at lower relative humidity (without phosphatization layer; MB_S2 with lower thickness or MB_S3 with higher thickness) presented any noticeable difference in the whole frequency range of Bode plot, with the film that was cast at higher relative humidity (with the phosphatization layer); namely, at the mild conditions of exposure (500 h in a solution of 3.5 wt% of NaCl) the performance of the coatings was very similar. The coating made out of the conventional surfactant did also present the same performance. This is indicative of the good barrier performance of the copolymer system employed in all coatings under the mild exposure conditions.

In order to get information about the effect of the phosphatization layer, experiments using a harsh environment were carried out (e.g. accelerated salt spray tests). The results for steel specimens coated with these latexes are summarized in Table 2.5 and Figure 2.22.

Table 2.4. Properties and anticorrosion performances of MB series coatings

Latex	Specimen tag	Average thickness (μm)	Drying conditions		Ph*	Flash rust	IZI ($\Omega \text{ cm}^2$)**
			T ($^{\circ}\text{C}$)	RH (%)			
	MB_S1	30	23	60	yes	no	10^9 - 10^{10}
MB_S	MB_S2	30	23	<60	no	no	10^9 - 10^{10}
	MB_S3	90	23	<60	no	no	10^9 - 10^{10}
MB_D	MB_D1	30	23	60	no	yes	10^9 - 10^{10}
None	Steel	-	-	-	-	-	10^3

* Phosphatization

** Impedance modulus values at 10^{-2} Hz after 500 h of immersion is 3.5 wt% NaCl solution

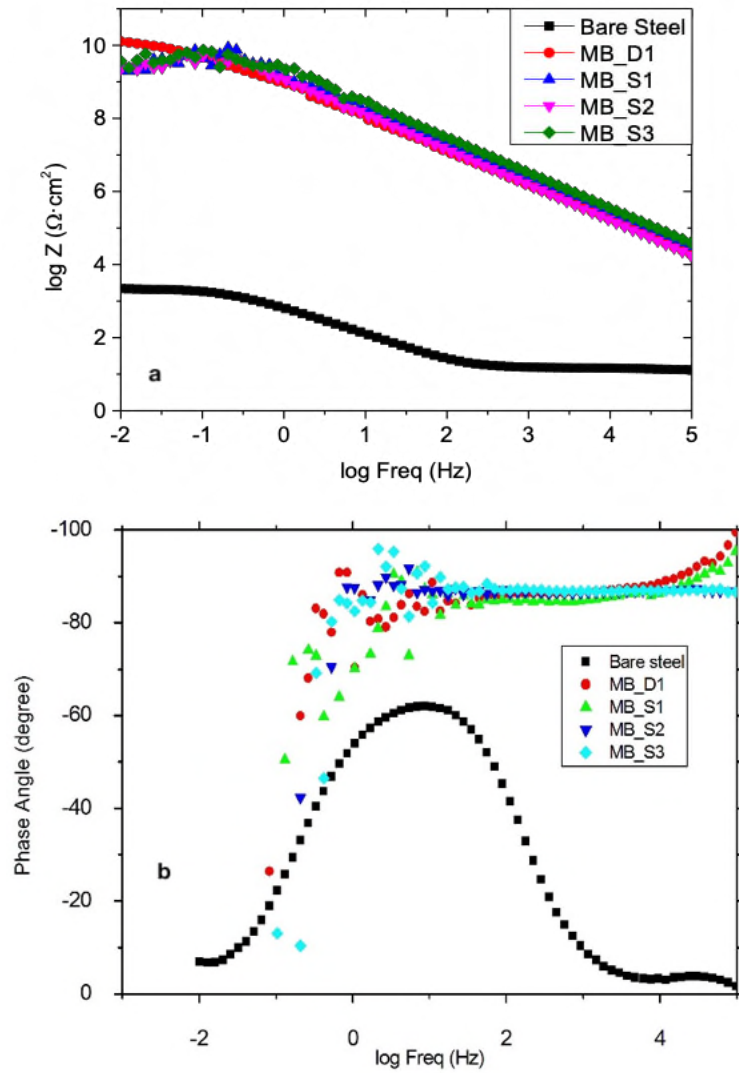


Figure 2.21. a) Bode plot and b) Phase plot for MB_D1, MB_S1, MB_S2 and MB_S3 coated steel substrates after 500 h immersion in 3.5 wt% NaCl solution.

Table 2.5. Salt spray test performances for MB_S and MB_D coated steel substrates.

Latex	Specimen tag	Film thickness (μm)	Drying conditions		IZI ($\Omega \text{ cm}^2$) *	
			T ($^{\circ}\text{C}$)	RH (%)	144h	408h
MB_S	MB_S4	58	23	60	10^9 - 10^{10}	10^9 - 10^{10}
MB_D	MB_D2	60	23	60	10^9 - 10^{10}	10^8

* Impedance modulus values at 10^{-2} Hz after 144 and 408 hours in salt spray test

Figure 2.22 shows the impedance diagram after different exposure periods in the neutral salt spray (NSS) chamber. Although the barrier protection remained intact after 144 h of exposure for both coatings, the influence of substrate phosphatization showed up after 408 h. In fact, the impedance modulus of MB_D2 (at low frequency range) dropped to $\approx 10^8 \Omega \text{ cm}^2$ while MB_S4 maintained the high value of circa $10^{10} \Omega \text{ cm}^2$.

In order to analyze the water sensitivity of both free films, MB_S and MB_D, liquid water uptake (WU) test, that consists in monitoring for 14 days the relative weight gain by circular specimens (diameter = 24 mm, thickness= 2.3 mm) in water was carried out (Figure 2.23).

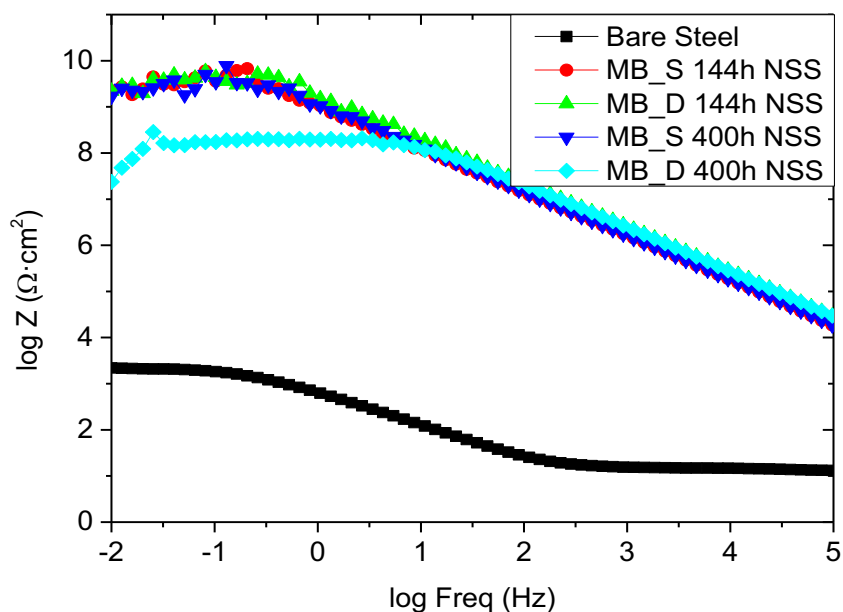


Figure 2.22. Bode plots of MB_S4 and MB_D2 after salt spray test.

As it can be seen, when Sipomer was used, the water uptake of the final film results lower, as has already been seen by other authors¹³, confirming the lower water sensitivity and higher barrier properties of MB_S compared to MB_D. Therefore, NSS results confirm the enhanced corrosion protection of MB_S coating by a synergetic effect of good barrier properties together with the substrate phosphatization. In fact, the permeation of water and ions through MB_D2 started to be more effective and, due to

the absence of a passive layer at the coating/substrate interface, the corrosion mechanism occurred for this sample.

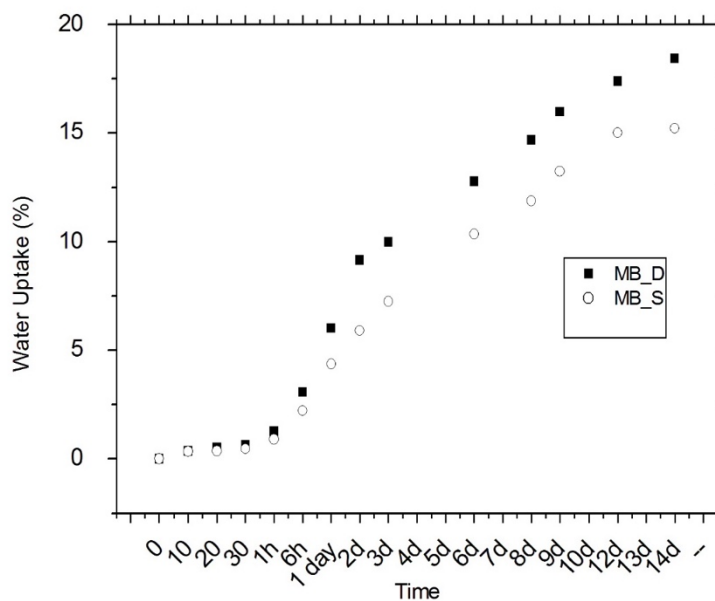


Figure 2.23. Water uptake evolution of MB_S and MB_D free films for 14 days in distilled water.

2.6 Conclusions

Poly(MMA-co-BA) nanoparticle dispersions with phosphated functionalities (MB_S) were successfully synthesized by seeded semibatch emulsion polymerization by using a polymerizable phosphate surfactant (SIP).

When MB_S latex was applied on low carbon steel, it was found that the phosphated functionalities, bearing from SIP, were able to phosphatize the steel surface under slow drying rate ($T=23\text{ }^{\circ}\text{C}$ and $\text{RH}=60\%$). The formation of a passive thin iron phosphate layer at the metal-coating surface was confirmed by energy dispersed X-rays analysis (EDX) and infrared spectroscopy (FTIR). Further analysis of the drying conditions showed that the in-situ phosphatization occurred in a restricted range of condition (23 and $35\text{ }^{\circ}\text{C}$ and RH comprised between 60 and 70%), out of which flush rust or bad film formation are dominating.

Coatings made from these latexes yield a phosphatization thin layer on steel substrates when dried at relative humidity higher than 60% at room temperature. This layer plays a very important role on the anticorrosion properties of these coatings. It was found that in harsh exposure conditions the coatings that contained the in-situ produced phosphatization layer, were able to present excellent corrosion protection after 400 h in salt-spray chamber, whereas latexes produced with the same composition but using a conventional non-polymerizable and non-phosphate containing group failed and corrosion started on the steel substrates. This opens the possibility to use this functional waterborne dispersion in paint formulations that might require little or no anticorrosion pigments to be used.

2.7 References

1. Pilcher, G. In *Meeting the challenge of radical change: coatings R&D as we enter the 21st century*, Macromolecular Symposia, Wiley Online Library: 2002; pp 1-16.
2. Asua, J. M., Emulsion polymerization: From fundamental mechanisms to process developments. *Journal of Polymer Science, Part A: Polymer Chemistry* **2004**, *42* (5), 1025-1041.
3. Pichot C., Delair T., and Kawaguchi H., Specialty Applications of Latex Polymers. In *Chemistry and Technology of Emulsion Polymerisation* cap. 11, 283-304.
4. Kang, K.; Kan, C.; Du, Y.; Liu, D., Synthesis and properties of soap-free poly(methyl methacrylate-ethyl acrylate-methacrylic acid) latex particles prepared by seeded emulsion polymerization. *European Polymer Journal* **2005**, *41* (3), 439-445.
5. Rahman, O. u.; Kashif, M.; Ahmad, S., Nanoferrite dispersed waterborne epoxy-acrylate: Anticorrosive nanocomposite coatings. *Progress in Organic Coatings* **2015**, *80*, 77-86.

6. Haase, M. F.; Grigoriev, D. O.; Möhwald, H.; Shchukin, D. G., Development of Nanoparticle Stabilized Polymer Nanocontainers with High Content of the Encapsulated Active Agent and Their Application in Water-Borne Anticorrosive Coatings. *Advanced Materials*, **2012**, *24* (18), 2429-2435.
7. Nguyen, T.; Bentz, D.; Byrd, E., Method for measuring water diffusion in a coating applied to a substrate. *Journal of Coatings Technology* **1995**, *67* (844), 37-46.
8. Roulstone, B.; Wilkinson, M.; Hearn, J., Studies on polymer latex films: II. Effect of surfactants on the water vapour permeability of polymer latex films. *Polymer international* **1992**, *27* (1), 43-50.
9. Aguirreurreta, Z.; Dimmer, J. A.; Willerich, I.; de la Cal, J. C.; Leiza, J. R., Water Whitening Reduction in Waterborne Pressure-Sensitive Adhesives Produced with Polymerizable Surfactants. *Macromolecular Materials and Engineering* **2015**, *300* (9), 925-936.
10. Aramendia, E.; Barandiaran, M. J.; Grade, J.; Blease, T.; Asua, J. M., Improving Water Sensitivity in Acrylic Films Using Surfmers. *Langmuir* **2005**, *21* (4), 1428-1435.
11. Liu, Y.; Soer, W.-J.; Scheerder, J. r.; Satgurunathan, G.; Keddie, J. L., Water vapor sorption and diffusion in secondary dispersion barrier coatings: A

critical comparison with emulsion polymers. *ACS Applied Materials & Interfaces* **2015**, 7 (22), 12147-12157.

12. Jiang, B.; Tsavalas, J. G.; Sundberg, D. C., Water whitening of polymer films: Mechanistic studies and comparisons between water and solvent borne films. *Progress in Organic Coatings* **2017**, 105, 56-66.

13. Aguirreurreta, Z.; de la Cal, J. C.; Leiza, J. R., Preparation of high solids content waterborne acrylic coatings using polymerizable surfactants to improve water sensitivity. *Progress in Organic Coatings* **2017**, 112, 200-209.

14. Mistry, J. K., Ironing out stains. *European Coating Journal* 2008, vol 12.

15. Chimenti, S.; Vega, J. M.; Aguirre, M.; García-Lecina, E.; Díez, J. A.; Grande, H.-J.; Paulis, M.; Leiza, J. R., Effective incorporation of ZnO nanoparticles by miniemulsion polymerization in waterborne binders for steel corrosion protection. *Journal of Coatings Technology and Research* **2017**, 14 (4), 829-839.

16. Montemor, M. F., Functional and smart coatings for corrosion protection: A review of recent advances. *Surface and Coatings Technology* **2014**, 258, 17-37.

17. US199209978. Additive package for in situ phosphatizing paint, paint and method 1994.
18. Reyes, Y.; Rodriguez, F. J.; del Rio, J. M.; Corea, M.; Vazquez, F., Characterisation of an anticorrosive phosphated surfactant and its use in waterborne coatings. *Progress in Organic Coatings* **2005**, *52* (4), 366-371.
19. Gonzalez, I.; Mestach, D.; Leiza, J. R.; Asua, J. M., Adhesion enhancement in waterborne acrylic latex binders synthesized with phosphate methacrylate monomers. *Progress in Organic Coatings* **2008**, *61* (1), 38-44.
20. Shi, X.; Nguyen, T. A.; Suo, Z.; Liu, Y.; Avci, R., Effect of nanoparticles on the anticorrosion and mechanical properties of epoxy coating. *Surface and Coatings Technology* **2009**, *204* (3), 237-245.
21. Arthur, D.; Jonathan, A.; Ameh, P.; Anya, C., A review on the assessment of polymeric materials used as corrosion inhibitor of metals and alloys. *International Journal of Industrial Chemistry* **2013**, *4* (1), 1-9.
22. Andreeva, D. V.; Shchukin, D. G., Smart self-repairing protective coatings. *Materials Today* **2008**, *11* (10), 24-30.
23. Asua, J. M.; Schoonbrood, H. A. S., Reactive surfactants in heterophase polymerization. *Acta Polymerica* **1998**, *49* (12), 671-686.

24. Schoonbrood, H. A. S.; Asua, J. M., Reactive Surfactants in Heterophase Polymerization. 9. Optimum Surfmer Behavior in Emulsion Polymerization. *Macromolecules* **1997**, *30* (20), 6034-6041.
25. Dais, P.; Paleos, C. M.; Nika, G.; Malliaris, A., Positional effects of the methacrylate group on polymerization and microstructure of micelle-forming quaternary ammonium salts studied by NMR spectroscopy. **1993** *Makromol Chemistry*, *194* (2), 445-450.
26. Aoki, S.; Morimoto, Y., Effect of location of polymerizable double bond on the polymerization of micelle-forming monomers. *J. Polymer Bulletin* **1996**, *37* (6), 777-784.
27. Unzué, M. J.; Schoonbrood, H. A. S.; Asua, J. M.; Goñi, A. M.; Sherrington, D. C.; Stähler, K.; Goebel, K.-H.; Tauer, K.; Sjöberg, M.; Holmberg, K., Reactive surfactants in heterophase polymerization. VI. Synthesis and screening of polymerizable surfactants (surfmers) with varying reactivity in high solids styrene—butyl acrylate—acrylic acid emulsion polymerization. *Applied Polymer Science*, **1997**, *66* (9), 1803-1820.
28. Misawa, T.; Hashimoto, K.; Shimodaira, S., Formation of Fe(II), Fe(III) intermediate green complex on oxidation of ferrous ion in neutral and slightly alkaline sulphate solutions. *Journal of Inorganic and Nuclear Chemistry* **1973**, *35* (12), 4167-4174.

29. McGill, I. R.; McEnaney, B.; Smith, D. C., Crystal structure of green rust formed by corrosion of cast iron. *Nature* **1976**, *259*, 200.
30. Abdelmoula, M., Evidence for the Fe(II)-Fe(III) Green Rust "Fougerite" Mineral Occurrence in a Hydromorphic Soil and Its Transformation with Depth. *Hyperfine Interactions* **1998**, *112* (1-4), 235-238.
31. Kannan, A. G.; Choudhury, N. R.; Dutta, N. K., Electrochemical performance of sol-gel derived phospho-silicate-methacrylate hybrid coatings. *Journal of Electroanalytical Chemistry* **2010**, *641* (1), 28-34.
32. Keddie, J.; Routh, A. F., *Fundamentals of latex film formation: processes and properties*. Springer Science & Business Media: 2010.
33. Misawa, T.; Hashimoto, K.; Shimodaira, S., The mechanism of formation of iron oxide and oxyhydroxides in aqueous solutions at room temperature. *Corrosion Science* **1974**, *14* (2), 131-149.
34. Tang, S.; Wang, W.; Chen, X.; Wang, J, Fluoridized iron phosphate as a novel adsorbent for selective separation/isolation of cytochrome. *J. Applied Chemistry part. B*, **2011**, *401* (10), 3283-3292.
35. Ait Salah, A.; Jozwiak, P.; Zaghbi, K.; Garbarczyk, J.; Gendron, F.; Mauger, A.; Julien, C. M., FTIR features of lithium-iron phosphates as electrode

materials for rechargeable lithium batteries. *Spectrochimica Acta Part A: Molecular and Biomolecular Spectroscopy* **2006**, *65* (5), 1007-1013.

36. Danmaliki, G. I.; Saleh, T. A., Effects of bimetallic Ce/Fe nanoparticles on the desulfurization of thiophenes using activated carbon. *Chemical Engineering Journal* **2017**, *307*, 914-927.

37. Sankara N., Surface pretreatment by phosphate conversion coatings- a review. *Review in Advanced Materials*, **2005**, *9* (2), 130-177.

38. Salazar-Medina, A. J.; Gámez-Corrales, R.; Ramírez, J. Z.; González-Aguilar, G. A.; Velázquez-Contreras, E. F., Characterization of metal-bound water in bioactive Fe(III)-cyclophane complexes. *Journal of Molecular Structure* **2018**, *1154*, 225-231.

39. Hadži, D.; Sheppard, N., The Infra-Red Absorption Bands Associated with the COOH and COOD Groups in Dimeric Carboxylic Acids. I. The Region from 1500 to 500 cm^{-1} , *Proceedings of the Royal Society of London. Series A, Mathematical and Physical Sciences* **1953**, *216* (1125), 247-266.

40. Pebere, N.; Picaud, T.; Duprat, M.; Dabosi, F., Evaluation of corrosion performance of coated steel by the impedance technique. *Corrosion Science* **1989**, *29* (9), 1073-1086.

41. Le Pen, C.; Lacabanne, C.; Pébère, N., Structure of waterborne coatings by electrochemical impedance spectroscopy and a thermostimulated current method: influence of fillers. *Progress in Organic Coatings* **2000**, 39 (2), 167-175.

Chapter 3

Effect of the incorporation of
hydrophobic perfluorinated monomer in
the corrosion protection of waterborne
latexes

3.1	Introduction.....	85
3.2	Synthesis of phosphated Poly(POA-co-MMA-co-BA) waterborne dispersion.....	87
3.3	Influence of the perfluorooctyl acrylate on the evolution of particle size.	89
3.4	Influence of the incorporation of POA on the film formation	90
3.5	Anticorrosion properties of POA based latexes	93
3.5.1	Influence of the coating thickness on the corrosion protection of PMB latex based film	96
3.5.2	The influence of iron phosphate layer on the corrosion protection.....	98
3.5.3	Evaluation of corrosion protection of PMB film in harsh conditions.	100
3.5.4	Evaluation of the barrier properties of PMB films.....	101
3.6	Conclusions.....	106
3.7	References.....	107

3.1 Introduction

The development of hydrophobic materials has recently attracted a lot of attention due to the wide range of applications that can be tailored by using their low surface energy. Self-cleaning, antifouling, stains-resistant surfaces are some of the applications that have been widely investigated and, within them, the use of hydrophobic material in anticorrosion applications represents an important area of interest^{1,2}.

Fluorinated polymers are effective reducing the surface free energy and are considered a promising material for producing hydrophobic surfaces thanks to the unique features of fluorine atom³⁻⁵. In addition to that, fluoropolymers have many unique properties including high thermal, chemical, aging, and weather resistance; low dielectric constant, refractive index, surface energy, and flammability and excellent inertness to solvents, hydrocarbons, acids, alkalis, and moisture absorption⁶⁻⁸. However, their high price limits their use. For that reason, the copolymerization with other comonomers is the most efficient way to get advantages of the premium properties of fluorine based materials and to produce more economic materials.

For instance, fluorinated (meth)acrylates present good reactivity with other (meth)acrylate monomers, such as methyl methacrylate (MMA), and their copolymerization results in copolymers that exhibit properties intermediate between those of parent homopolymers^{9,10}, and which make them suitable to be used in a wide variety of

applications. The eco-friendly emulsion polymerization has been proved to be a promising way to synthesize fluoro-copolymers¹¹⁻¹³.

Based on these interesting premises, the objective of this Chapter is to increase the hydrophobicity of the latexes developed in Chapter 2, that have shown an excellent anticorrosion performance, by the incorporation of a perfluorooctyl acrylate monomer (POA, Figure 3.1) in the polymer composition. Generally, the incorporation of hydrophobic monomers like POA in a waterborne dispersion is better achieved by employing miniemulsion polymerization^{14, 15} to facilitate the incorporation of the perfluorooctyl acrylate monomer that is too hydrophobic for conventional emulsion polymerization¹⁶.

The influence of the perfluorinated monomer onto the film formation, anticorrosion properties and surface in-situ phosphatization has been investigated in this chapter.

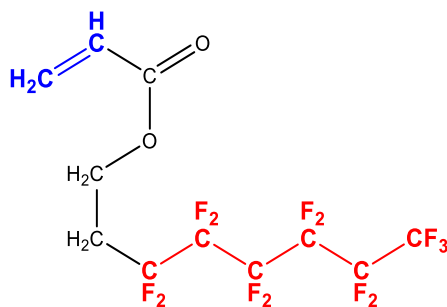


Figure 3.1. Chemical structure of Perfluorooctyl acrylate (POA).

3.2 Synthesis of phosphated Poly(POA-co-MMA-co-BA) waterborne dispersion

Seeded semibatch emulsion copolymerizations were carried out to synthesize the latex while the seed, based on perfluoro acrylate monomer, was produced by miniemulsion polymerization. It is worth mentioning that the latex composition presented below has been selected, after a preliminary screening, within several latex formulations that, for the sake of simplicity, are not discussed in this chapter. However, the list of reactions performed is reported in Appendix III.3.

In the optimal formulation (Table 3.1) to produce a latex of 50 % solids content and composition of POA/MMA/BA = 30/40/30 wt% (the resulting latex is labelled PMB), the whole amount of POA plus a small amount of MMA and BA were mixed to produce the oil phase of the seed miniemulsion. The aqueous phase was composed by Dowfax 2A1 surfactant (DOW) and deionized water in a solution at 2 wt%. Both oil and aqueous phases were mixed under magnetic stirring for 15 minutes and then they were mixed together for 15 minutes more. Subsequently, the oil-in-water coarse emulsion, with a solids content of 30%, was sonicated using a Branson Sonifier 450 for 15 min (operating at 8-output control and 70% duty cycle in an ice bath and under magnetic stirring), allowing the formation of a stable miniemulsion.

Table 3.1. Formulation used to synthesize PMB_S waterborne binder.

Component	Miniemulsion (seed) (g)	Preemulsion (g)
Oil phase	POA	-
	MMA	90.07
	BA	65.09
	AIBN	-
Aqueous phase	Water	28.93
	DOW	-
	SIP	5

The polymerization was started by loading the miniemulsion in the reactor and heating up the reactor to 70 °C. Once the reactor reached 70 °C, the initiator was introduced as a shot (1% wbm of AIBN) and the miniemulsion was left to polymerize for 30 minutes to produce in-situ the seed latex. After those 30 minutes, a preemulsion based on the remaining monomer mixture (MMA/BA), water and 2 wbm% (weight % based on total monomer) of Sipomer PAM200 (SIP) was fed for 4 hours (Table 3.1). As in the case of the synthesis of MMA/BA latex, the preemulsion containing SIP surfactant was neutralized. After the end of the preemulsion feeding, the reaction was post-polymerized for an additional hour.

3.3 Influence of the perfluorooctyl acrylate on the evolution of particle size

The seed latex of the POA comonomer (and a small amount of BA and MMA), produced by miniemulsion polymerization, had substantially large average particle size (348 nm), compared to the (MMA/BA) seed used in Chapter 2, mainly due to the larger size of the nanodroplets produced in the miniemulsification step ($d_d = 342\text{nm}$). The reasons behind the large nanodroplet size are probably the high viscosity of POA, its higher hydrophobicity (which will lower the emulsifier efficiency) and not enough energy used in the miniemulsification step¹⁵. Note that no attempt was done to control the seed miniemulsion droplet size and droplet size distribution in this study. During the semibatch process, the polymerization evolved under starved conditions, reaching full monomer conversion, and the final particle size of the latex (506 nm) was close to the theoretical value (509 nm) (Figure 3.2). This result indicates a stable particle growth, without neither secondary nucleation nor coagulation phenomena taking place during polymerization.

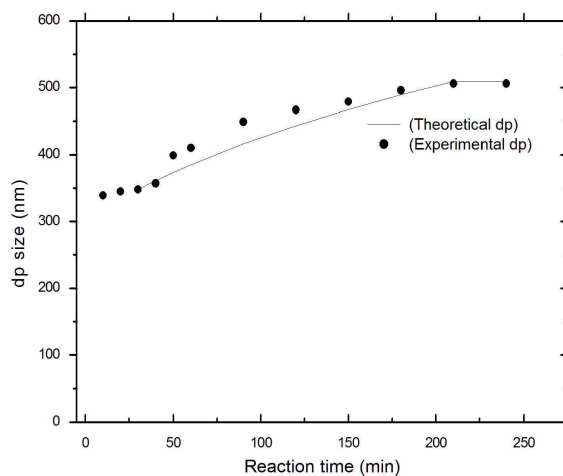


Figure 3.2. Time evolution of particle diameter during the semibatch emulsion polymerization of POA/MMA/BA. Note: the theoretical particle diameter was calculated for the semibatch process ($t \geq 30$ min) assuming that the number of particles of the seed remained constant during the feeding period.

3.4 Influence of the incorporation of POA on the film formation

The first feature that we expected to be enhanced by the incorporation of POA was the hydrophobicity of the coating surface. Experimentally, when a drop of liquid is placed onto a solid surface, a contact angle (θ) is created which is basically the angle formed at the liquid-solid-vapor interface (Figure 3.3). The contact angle of a liquid on

a smooth and chemically homogeneous solid surface is given by Young's equation¹⁷ and generally is higher than 90° for hydrophobic surfaces^{13, 18-22}.

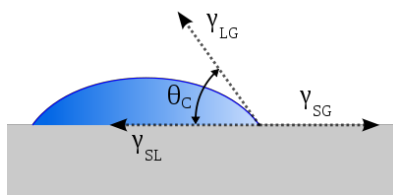


Figure 3.3. Scheme of the contact angle (θ) of a liquid drop with a flat surface.

As shown in Figure 3.4, θ of the fluorine free film (MB) was nearly 75°, which is characteristic of a rather hydrophilic surface. After introducing 30 wt.% of POA in the polymer composition (PMB), the surface of the film became more hydrophobic with θ of about 120°, which is the maximum value obtainable on a flat surface (to produce higher θ , it is necessary to create roughness on the surface)¹⁹.

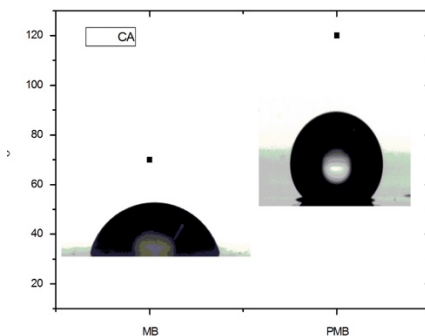


Figure 3.4. Effect of the incorporation of POA on the contact angle.

Once the enhanced surface hydrophobicity was proved, the next step was to confirm the ability to in-situ phosphatize the metal substrate as previously seen in Chapter 2.

Steel substrate specimens were coated at 23 °C and at different relative humidity (RH) with the synthesized perfluorinated waterborne copolymer dispersion (PMB) (Figure 3.5). Substrate phosphatization occurred when the film was formed at slow drying rate conditions (RH= 60%). However, at higher drying rates (RH<60%), no phosphatization occurred as can be seen in Figures 3.5 a, b and c, in agreement with the results previously reported in Chapter 2.

Based on these results, the influence of film thickness and drying conditions onto the anticorrosion performance of PMB latex-based coatings were investigated in the following section.

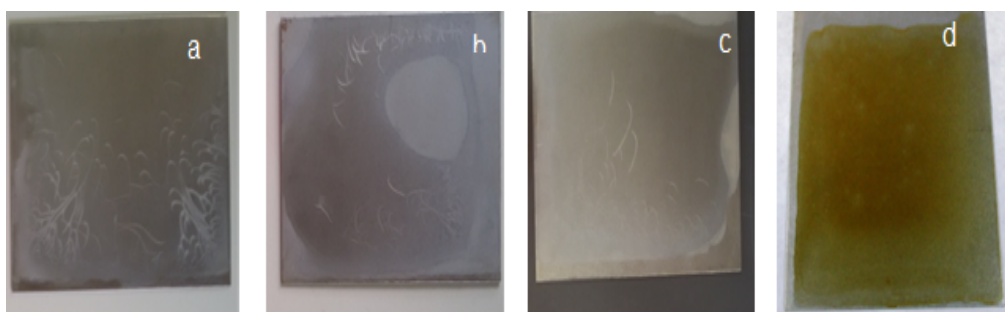


Figure 3.5. PMB cast on steel substrates at different drying conditions; $T=23\text{ }^{\circ}\text{C}$ (constant), a) RH=30%, b) RH=43%, c) RH=50%, d) RH=60%.

3.5 Anticorrosion properties of POA based latexes

The influence of drying conditions and coating thickness onto the anticorrosion performance of PMB latex-based coatings were investigated, as in Chapter 2, by electrochemical impedance spectroscopy (EIS). The impedance modulus values at 10^{-2} Hz after 500 h of immersion in 3.5 wt% NaCl solution are reported in Table 3.2.

Table 3.2. *Properties and anticorrosion performances of PMB_S latex.*

Specimen tag	Average thickness (μm)	Drying conditions		Ph *	Flash rust	IZI ($\Omega \text{ cm}^2$) **
		T ($^{\circ}\text{C}$)	RH%			
PMB1	30	23	60	yes	no	10^9 - 10^{10}
PMB2	30	23	<60	no	no	10^3
PMB3	90	23	<60	no	no	10^5
Steel	-	-	-	-	-	10^3

*Phosphatization

** Impedance modulus after 500 h of immersion in 3.5 wt% NaCl solution.

Figure 3.6a shows the Bode plots of specimens coated with the same thickness (30 μm) but different relative humidity, PMB1 and PMB2 at high and low RH respectively. High impedance modulus at low frequency (<10 mHz) indicates efficient corrosion protection properties of the coating at the coating-substrate interface, whereas high modulus values at higher frequency (>10mHz) usually indicates good barrier properties

of the coating^{23,24}. The coating cast at slow drying conditions (PMB1), presented high corrosion protection properties according to the high impedance value at low frequency ($10^9 \Omega\text{cm}^2$), associated with a single time constant and a capacitive behaviour typical of a good barrier coating (Figure 3.6b). Interestingly, the coating cast under low relative humidity conditions (fast drying, PMB2) with the same thickness, presented very poor anticorrosion performances; indeed, the impedance was very similar to the bare steel.

This was not expected because coatings based on poly(MMA-co-BA) synthesized without Sipomer PAM200 surfactants (MB_D in Chapter 2), and hence without having a phosphatization layer, presented better performances under similar conditions and it was expected that better or at least same barrier properties will be provided by the incorporation of the hydrophobic POA comonomer. This poor performance can likely be attributed to a weaker film cast from PMB and dried at $\text{RH} < 60\%$. In fact, as it can be noticed in Figure 3.5, some defects can be seen on the coating surface, which may behave like channels for the diffusion of water, oxygen and ions to the metal-coating interface.

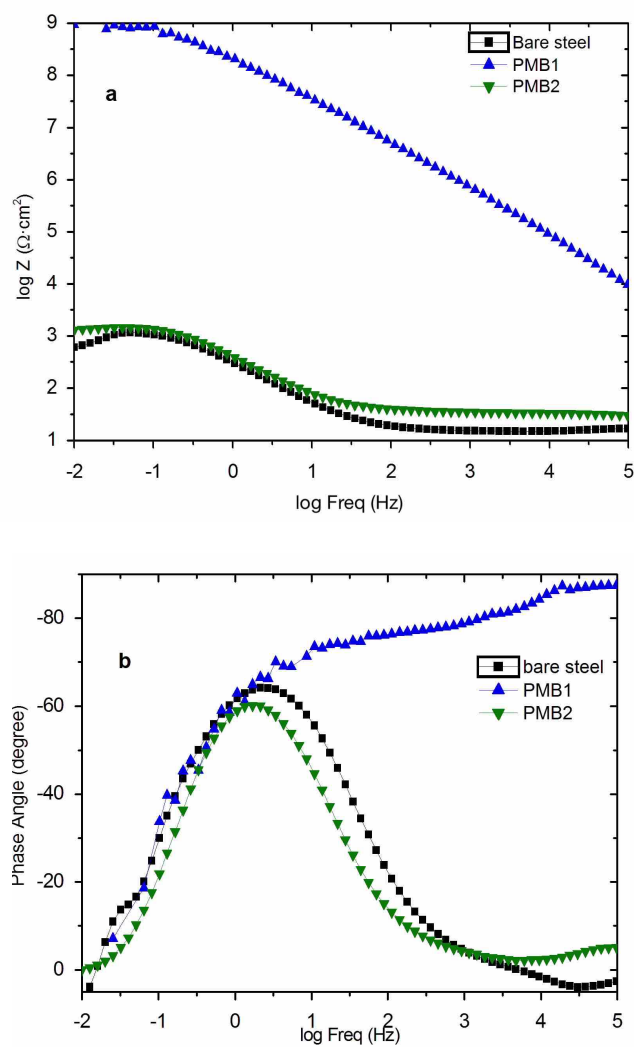


Figure 3.6. a) Bode plots and b) phase angle diagrams of Steel, PMB1 and PMB2 after 500 h immersion in 3.5 wt. % NaCl solution.

3.5.1 Influence of the coating thickness on the corrosion protection of PMB latex based film

A coating cast at low relative humidity but with higher thickness was tested by EIS (PMB3, see Table 3.2). This new coating was three times thicker than PMB2 (90 μm). Figure 3.7a shows the Bode plot of PMB3 system at different times of exposure. Although the impedance diagram of PMB3 indicates certain protection ($5 \cdot 10^4 \Omega\text{cm}^2$) compared to bare steel, such improvement was not enough to reach the good performance of PMB1 coating after 500 h of exposure. Its phase angle diagram (Figure 3.7b) shows the presence of two-time constants. Furthermore, the impedance dropped to values similar to that of steel after 6 h of exposure. These results indicate that building up a thicker coating with POA containing latex was not enough to provide better barrier properties for the coating in absence of the phosphatization layer; in other words, the in-situ produced phosphatization layer is critical to achieve a good anticorrosion performance for the PMB latexes.

In the following sub-section, the influence of the iron phosphate layer has been investigated.

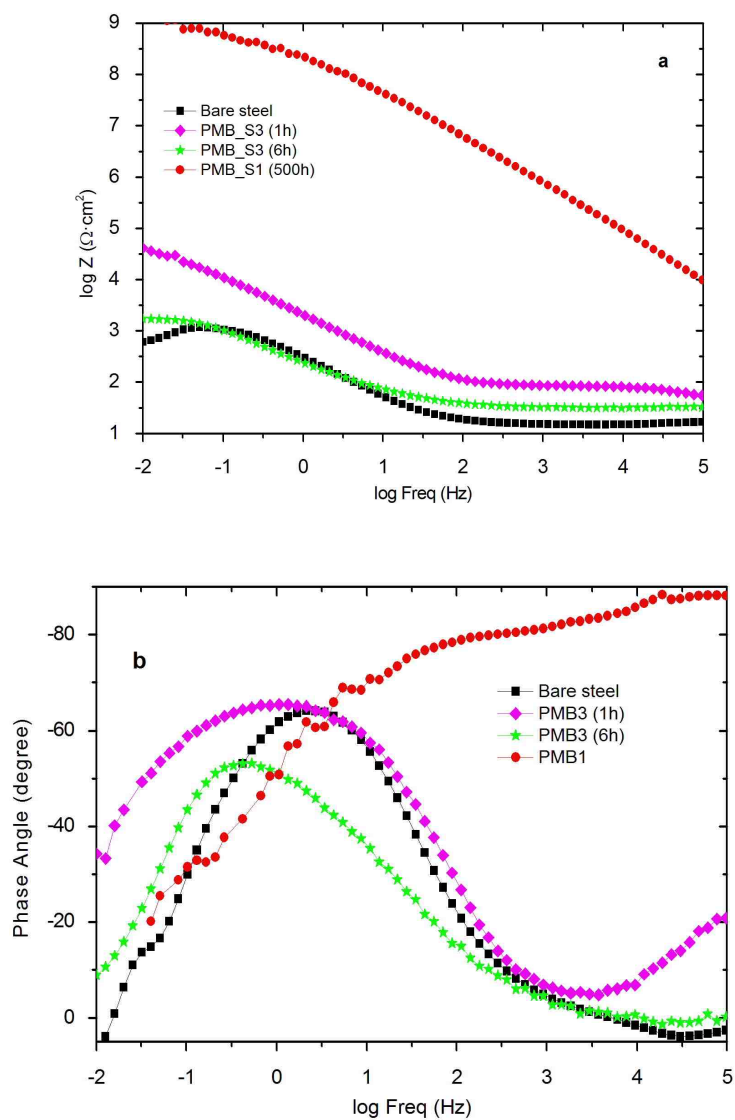


Figure 3.7. a) Bode plots and b) phase angle diagram of Steel, PMB1 and PMB3 after different immersion times in 3.5 wt. % NaCl solution.

3.5.2 The influence of iron phosphate layer on the corrosion protection

In order to isolate the role of the phosphate layer from the barrier protection provided by the coating itself, an artificial defect was created in a PMB coating, cast at 23 °C and 60 % of RH (providing a phosphate layer at the coating-steel interface) with an infrared laser with the goal to destroy the film in a localized spot and to reach the interface. Once the defect was created on PMB1 coat, EIS measurements at different times of immersion (1 h and 6 h) were performed as it is shown in Figure 3.8.

If we compare these impedance diagrams with the same system without defect (Figure 3.6), there is a huge decrease of the impedance modulus (from $10^9 \Omega\text{cm}^2$ to $4 \cdot 10^5 \Omega\text{cm}^2$ or less) at low frequency (10 mHz). The phase angle diagram (Figure 3.8 b) shows two time constants instead of the single time constant observed before the presence of the defect (Figure 3.6b). Moreover, the increase of the exposure time shows how the impedance progressively decreases to lower values as an indication of the degradation of the iron phosphate layer and the progress of the corrosion reactions in the substrate (Figure 3.8a).

Therefore, EIS has provided valuable information of the metal/coating interface of PMB1 systems (after an artificial defect was created) and confirms the corrosion

protection role played by the phosphate groups generated during the film casting process.

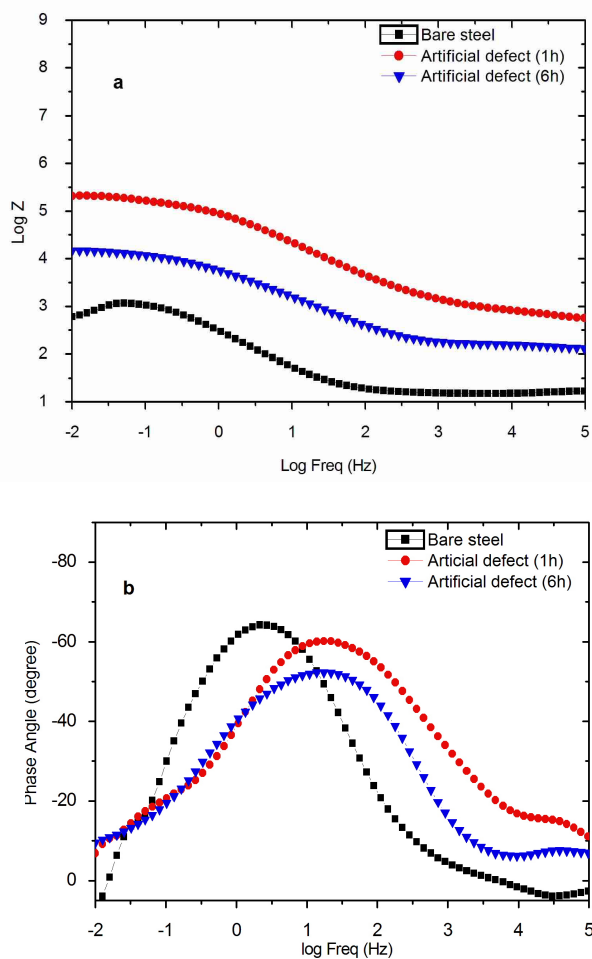


Figure 3.8. *a) Bode plots and b) phase angle diagram of PMBI film with an artificial defect after 1h and 6h of immersion in 3.5 wt. % NaCl.*

Therefore, it can be concluded that to provide complete and long-lasting protection against corrosion using PMB latex based coatings (i.e. impedance value of $10^9 \Omega\text{cm}^2$ after 500 h of immersion in NaCl 3.5 wt% solution), the combination of phosphatization and a coating thickness of at least $30 \mu\text{m}$ is necessary.

3.5.3 Evaluation of corrosion protection of PMB film in harsh conditions.

The corrosion resistance of steel specimens cast under high relative humidity (RH = 60 %; slow drying) from latex PMB were further assessed by introducing them in a salt spray chamber. Figure 3.9 presents the images of the samples after the experiment; clearly the specimen suffered corrosion already after 24 h (Figure 3.9a) and severe deterioration after 140 h of exposure to the salt spray (Figure 3.9b). Due to the deterioration of the specimen, EIS analysis of these samples was not carried out.

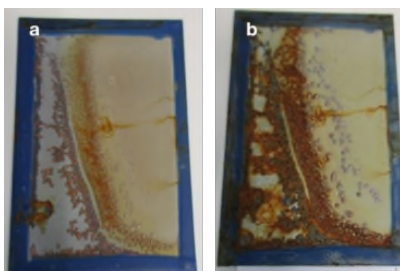


Figure 3.9 PMB coated specimen after 24 (a) and 140 (b) h of exposure in salt spray atmosphere.

This result was not expected because less hydrophobic coatings made of poly (MMA-co-BA) latexes (MB) showed a superior performance in salt spray chamber; i.e., no failure was observed up to 400 hours of salty fog exposure (Figure 2.17 of Chapter 2). This indicates that even under the optimal drying conditions (low drying rate and in-situ phosphatization), the PMB coating revealed a weakness that is likely due to the intrinsic coating film morphology.

3.5.4 Evaluation of the barrier properties of PMB films

The morphology of the PMB film was investigated by scanning electron microscopy (SEM). In addition, as the corrosion is mainly related to the diffusion of water and other ions through the coating, water uptake and water vapor permeability of the films were measured. Regarding the water uptake and WVTR, Table 3.3 shows the values for PMB and, for comparison purposes, the values for the film cast from MB have been included. As it can be seen, films of PMB absorbed less water than MB. The low dielectric constant of the pendant perfluorinated side chains of the perfluorooctyl acrylate being likely the reason for the lower water uptake. In general, polymers with low dielectric constant such as Teflon or Kapton (2.1 and 3.0 respectively) ²⁵ show weak interactions with materials with higher dielectric constant such as water which, results in a low absorption of one in the other. Even if the water absorption was lower for PMB latex films, the vapour permeability was substantially higher for this film.

Table 3.3. *Water uptake after 14 days and WVTR results.*

	WU	WVTR
	Weight gain %	g of H ₂ O mm/m ² by Day
MB_S	13	12
PMB_S	7	63

Although this behaviour was not expected because the absorption and the permeation phenomena are connected to each other, it is worth to note that they are governed by different mechanisms²⁶⁻²⁹. Absorption is controlled by the dissolution properties of solvent and solute, whereas permeation of water vapour is controlled by both the dissolution and diffusion of the permeant molecules. The later, it is governed by temperature, concentration of permeant agent on the two sides of the film and the bulky conformation of the materials³⁰. In literature, several works have reported opposite behaviour in liquid water and vapor permeation for different polymeric materials³⁰. Moreover, it is worth to point out that water aggregation status change in liquid and vapour phase, which means differences in mobility rate. Based on that, even if the PMB is not prone to liquid water absorption, its higher free volume, related to the pendant side chain, may allow the transport of the non-associated water vapor molecules more easily than the film based on MB latex. Although it is doubtful to draw conclusions, based only on WVTR measurements, the link between the higher permeability against water vapour molecules and the protection failure in harsh corrosive conditions, shown during the salt spray test, is striking. In fact, in salt spray test, water contacts the coating

in the form of vapour and in this condition, it is able to permeate more through the coating, to reach the interface with the substrate and to trigger the corrosion. This data suggests that there should be notable differences between the film morphology of poly(MMA-co-BA) (MB) and poly(POA-co-MMA-co-BA) (PMB) coatings.

In order to investigate the film morphology, the cross section of films cast from MB and PMB latexes were analysed by scanning electron microscopy. While MB film was homogeneous and defect free (Figure 3.10), PMB film clearly presented lack of coalescence of the particles during the film formation (Figure 3.11). The incomplete particle coalescence leads to the formation of channels through which the water molecules are free to diffuse. Generally, the stiffness of a material can impair the polymer diffusion during the particle coalescence and hence the formation of a coherent film. Nevertheless, the perfluorinated copolymer is characterized by a T_g and a minimum film formation temperature (MFFT) that are below the ambient temperature ($T_g = 14.5\text{ }^\circ\text{C}$ and $\text{MFFT} = 9\text{ }^\circ\text{C}$) which means that the material is soft enough to diffuse.

A possible reason for this observation could be found in the low miscibility between the perfluorinated enriched domains and the rest of the acrylic polymer. Due to the crucial effect on the anticorrosion performance of PMB, the morphology of the polymer particles has been deeply investigated in the following Chapter.

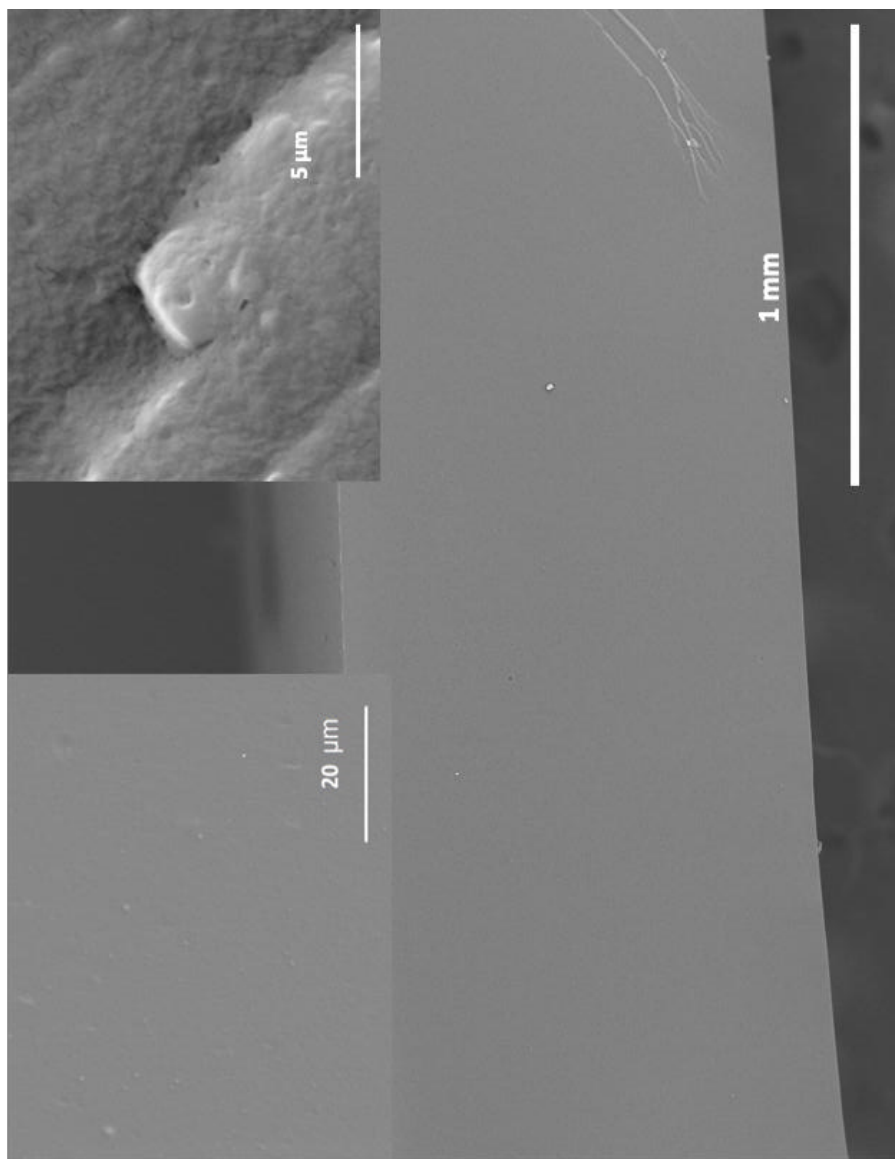


Figure 3.10. SEM micrograph (cross-section) for MB films.

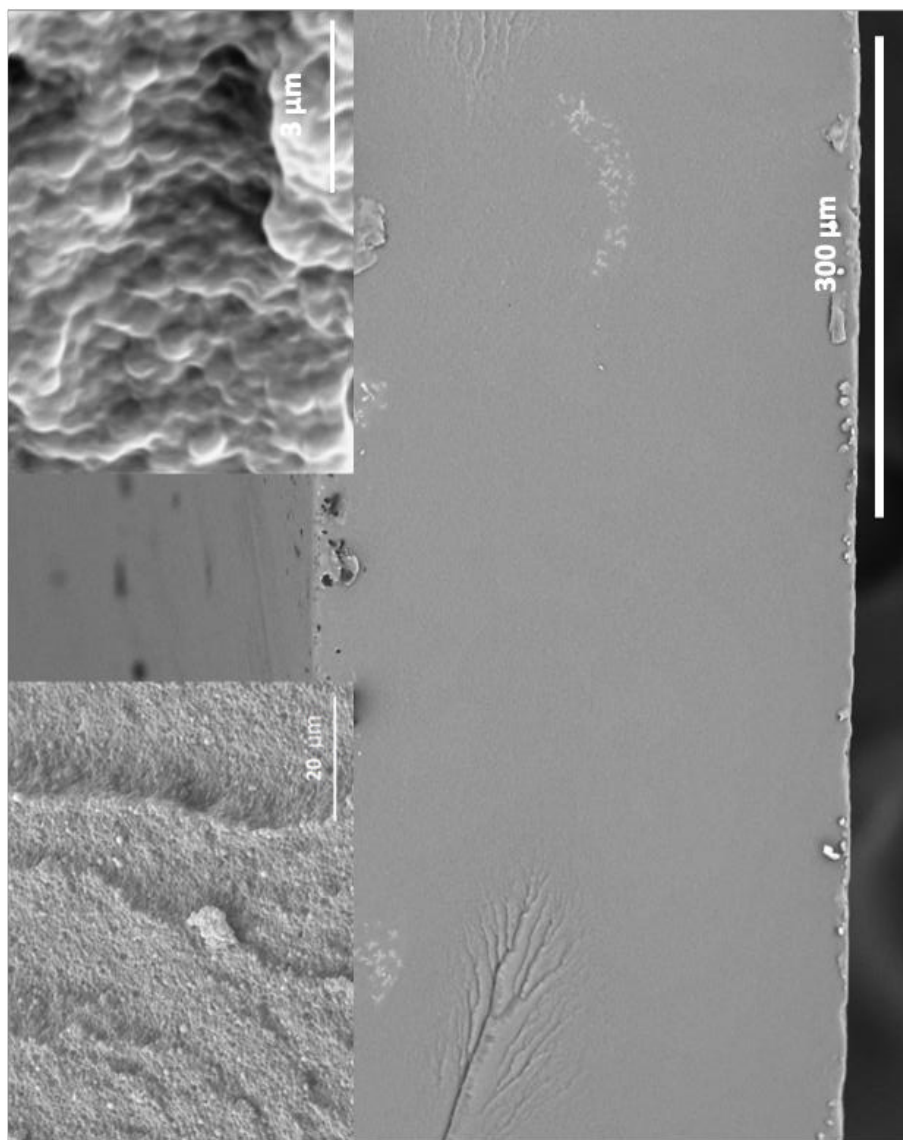


Figure 3.11. SEM micrograph (cross-section) for PMB films.

3.6 Conclusions

The incorporation of perfluorooctyl acrylate (POA) in waterborne latexes containing phosphate functionalities was successfully performed by seeded semibatch emulsion polymerization in which the seed (containing the whole amount of POA required to obtain a final composition of POA/MMA/BA = 30/40/30) was made by miniemulsion polymerization.

Even though the increase of hydrophobicity of the resulting coating (cast from PMB latex) was achieved, the incorporation of POA comonomer did not show up the expected enhancement of the corrosion performance. In fact, despite the presence of iron phosphate layer at the coating-substrate interface, the coating cast from PMB was not able to protect the metal substrate against corrosion in the harsh conditions present in the salt spray chamber.

By SEM analysis, it was found that the lack of particle coalescence during the film formation could be the most probable reason behind the bad corrosion performance of PMB films in harsh exposure conditions.

However, this finding confirmed the key role of the phosphatization layer that is able to enhance the corrosion protection of a relatively bad coating film and to guarantee the protection in mild exposure conditions (immersion in 3.5 wt% NaCl solution).

3.7 References

1. De Leon, A.; Advincula, R. C., Chapter 11 - Conducting Polymers with Superhydrophobic Effects as Anticorrosion Coating. In *Intelligent Coatings for Corrosion Control*, Tiwari, A.; Rawlins, J.; Hihara, L. H., Eds. Butterworth-Heinemann: Boston, **2015**; pp 409-430.
2. Montemor, M. F., Functional and smart coatings for corrosion protection: A review of recent advances. *Surface and Coatings Technology* **2014**, *258*, 17-37.
3. Nishino, T.; Meguro, M.; Nakamae, K.; Matsushita, M.; Ueda, Y., The Lowest Surface Free Energy Based on $-CF_3$ Alignment. *Langmuir* **1999**, *15* (13), 4321-4323.
4. Stone, M.; Nevell, T. G.; Tsibouklis, J., Surface energy characteristics of poly(perfluoroacrylate) film structures. *Materials Letters* **1998**, *37* (1-2), 102-105.
5. Castelvetro, V.; Aglietto, M.; Ciardelli, F.; Chiantore, O.; Lazzari, M.; Toniolo, L., Structure control, coating properties, and durability of fluorinated acrylic-based polymers. *Journal of Coatings Technology* **2002**, *74* (928), 57-66.
6. Roche, V.; Vacandio, F.; Bertin, D.; Massiani, Y. J. J. o. E., Corrosion performance of lamellae nanostructured fluorinated organic coating applied on steel. *Journal of Electroceramics* **2006**, *16* (1), 41-47.

7. McLain, S. J.; Sauer, B. B.; Firment, L. E., Surface Properties and Metathesis Synthesis of Block Copolymers Including Perfluoroalkyl-Ended Polyethylenes. *Macromolecules* **1996**, *29* (25), 8211-8219.
8. Park, I. J.; Lee, S.-B.; Choi, C. K., Surface properties for poly(perfluoroalkylethyl methacrylate)/poly(n-alkyl methacrylate)s mixtures. *Journal of Applied Polymer Science*. **1994**, *54* (10), 1449-1454.
9. Erol, I.; Sen, O.; Dedelioglu, A.; Cifci, C., Synthesis and characterization of novel fluorine-containing methacrylate copolymers: Reactivity ratios, thermal properties, and antimicrobial activity. *Journal of Applied Polymer Science* **2009**, *114* (6), 3351-3359.
10. Thomas, R. R.; Anton, D. R.; Graham, W. F.; Darmon, M. J.; Sauer, B. B.; Stika, K. M.; Swartzfager, D. G., Preparation and Surface Properties of Acrylic Polymers Containing Fluorinated Monomers. *Macromolecules* **1997**, *30* (10), 2883-2890.
11. Yang, W.; Zhu, L.; Chen, Y., Spherical and core-shell fluorinated polyacrylate latex particles: preparation and characterization. *Colloid Polymer Science* **2015**, *293* (8), 2349-2357.
12. Li, K.; Zeng, X.; Li, H.; Lai, X., Fabrication and characterization of stable superhydrophobic fluorinated-polyacrylate/silica hybrid coating. *Applied Surfaces Science* **2014**, *298*, 214-220.

13. López, A. B.; de la Cal, J. C.; Asua, J. M., Highly Hydrophobic Coatings from Waterborne Latexes. *Langmuir* **2016**, *32* (30), 7459-7466.
14. Asua, J. M., Challenges for industrialization of miniemulsion polymerization. *Progress in Polymer Science* **2014**, *39* (10), 1797-1826.
15. Asua, J. M., Miniemulsion polymerization. *Progress in Polymer Science* **2002**, *27* (7), 1283-1346.
16. Zhang, Q.; Zhan, X.; Chen, F., Miniemulsion polymerization of a fluorinated acrylate copolymer: kinetic studies and nanolatex morphology characterization. *Journal of Applied Polymer Science* **2007**, *104* (1), 641-647.
17. Young, T., III. An essay on the cohesion of fluids. *Philosophical Transactions of the Royal Society of London* **1805**, *95*, 65-87.
18. Wenzel, R. N., Resistance of solid surfaces to wetting by water. *Industrial & Engineering Chemistry* **1936**, *28* (8), 988-994.
19. Boinovich, L. B.; Emelyanenko, A. M., Hydrophobic materials and coatings: principles of design, properties and applications. *Russian Chemical Review*. **2008**, *77* (7), 583-600.
20. López, A. B.; de la Cal, J. C.; Asua, J. M., From fractal polymer dispersions to mechanically resistant waterborne superhydrophobic coatings. *Polymer* **2017**, *124*, 12-19.

21. López, A. B.; de la Cal, J. C.; Asua, J. M., Controlling film topography to form highly hydrophobic waterborne coatings. *Soft Matter* **2016**, *12* (33), 7005-7011.
22. López, A. B., Waterborne Fluoropolymer Dispersion For Super-Hydrophobic coatings. *PhD Thesis UPV/EHU, POLYMAT*, 2016.
23. Pebere, N.; Picaud, T.; Duprat, M.; Dabosi, F., Evaluation of corrosion performance of coated steel by the impedance technique. *Corrosion Science* **1989**, *29* (9), 1073-1086.
24. Le Pen, C.; Lacabanne, C.; Pébère, N., Structure of waterborne coatings by electrochemical impedance spectroscopy and a thermostimulated current method: influence of fillers. *Progress in Organic Coatings* **2000**, *39* (2), 167-175.
25. Ren, Y.; Lam, D. C. C., Properties and Microstructures of Low-Temperature-Processable Ultralow-Dielectric Porous Polyimide Films. *Journal of Electronic Materials* **2008**, *37* (7), 955.
26. Barrer, R. M.; Rideal, E. K., Permeation, diffusion and solution of gases in organic polymers. *Transactions of the Faraday Society* **1939**, *35* (0), 628-643.
27. Jiang, B.; Tsavalas, J. G.; Sundberg, D. C., Water whitening of polymer films: Mechanistic studies and comparisons between water and solvent borne films. *Progress in Organic Coatings* **2017**, *105*, 56-66.

28. Ashley, R. J., Permeability and Plastics Packaging. In *Polymer Permeability*, Comyn, J., Ed. Springer Netherlands: Dordrecht, **1985**; pp 269-308.
29. Liu, Y.; Soer, W.-J.; Scheerder, J.; Satgurunathan, G.; Keddie, J. L., Water Vapor Sorption and Diffusion in Secondary Dispersion Barrier Coatings: A Critical Comparison with Emulsion Polymers. *ACS Applied Materials & Interfaces* **2015**, 7 (22), 12147-12157.
30. Sangaj, N. S.; Malshe, V. C., Permeability of polymers in protective organic coatings. *Progress in Organic Coatings* **2004**, 50 (1), 28-39.

Chapter 4

Assessment of the particle morphology of perfluorooctyl acrylate containing latex

4.1	Introduction.....	115
4.2	PMB polymer particles morphology	115
4.3	TEM characterization of cryo-sectioned wet films	118
4.4	sSNOM characterization of cryo-sectioned wet films.....	123
4.5	Conclusions.....	130
4.4	References.....	131

4.1 Introduction

As shown in Chapter 3, the incorporation of a perfluorinated comonomer (perfluorooctyl acrylate labelled as POA) in the formulation of the waterborne latex based on poly(MMA-co-BA), affected the barrier properties of the resulting film. In fact, from the scanning electron microscopy micrographs (Figure 3.11), it was observed that the film was characterized by the presence of not coalesced particles that caused the formation of channels that facilitated the diffusion of permeant molecules and that strongly damaged the corrosion protection performance of the fluorinated coating.

In view of these data, in the present chapter we aimed at shedding light on the causes that prevented the poly(POA-co-MMA-co-BA)(PMB) polymer particles to form coherent and homogeneous films. More specifically, we have carefully analysed the morphology of the polymer particles and its influence on the film formation of the latex. For that purpose, transmission electron microscopy (TEM) and scattering-type scanning near-field optical microscopy (sSNOM) have been used.

4.2 PMB polymer particles morphology

In an effort to identify in detail particle morphology, TEM analysis of the PMB latex particles was carried out. Figure 4.1a presents a conventional TEM micrograph of the final latex with four particles that do not show any noticeable electron density change

that might indicate any phase separation or distinctive morphology. However, the influence of the POA comonomer onto the resulting latex particle morphology showed up in the STEM-HAADF micrograph (Scanning Transmission Electrical Microscopy coupled with High-Angle Annular Dark Field detector; see Appendix II.15 for detailed information). In fact, the presence of perfluorinated side chains in the acrylate comonomer resulted in intraparticle phase separation with a highly electron dense region located in the inner shell of the particle, that suggests a core-shell-shell morphology (Figure 4.1b). It is worth to point out that in STEM analysis, assisted with HAADF detector, brighter regions represent high electron dense domains, whereas in the traditional TEM analysis is the opposite (the brighter regions are less electrically dense). In the present case, the brighter region is generated by the interaction between the electron beam and the big fluorine nuclei of the perfluorinated pendant chains of POA. In fact, the contrast obtained in STEM-HAADF is generated by the electrons that have experienced nuclear interactions (i.e. scattered or diffracted into an angle greater than the axial detector acceptance angle typical of TEM analysis) and hence, it gives information on the chemical nature of the sample¹.

In order to shed light on the intraparticle phase separation, we further investigated the unexpected morphology found in the PMB latex particles.

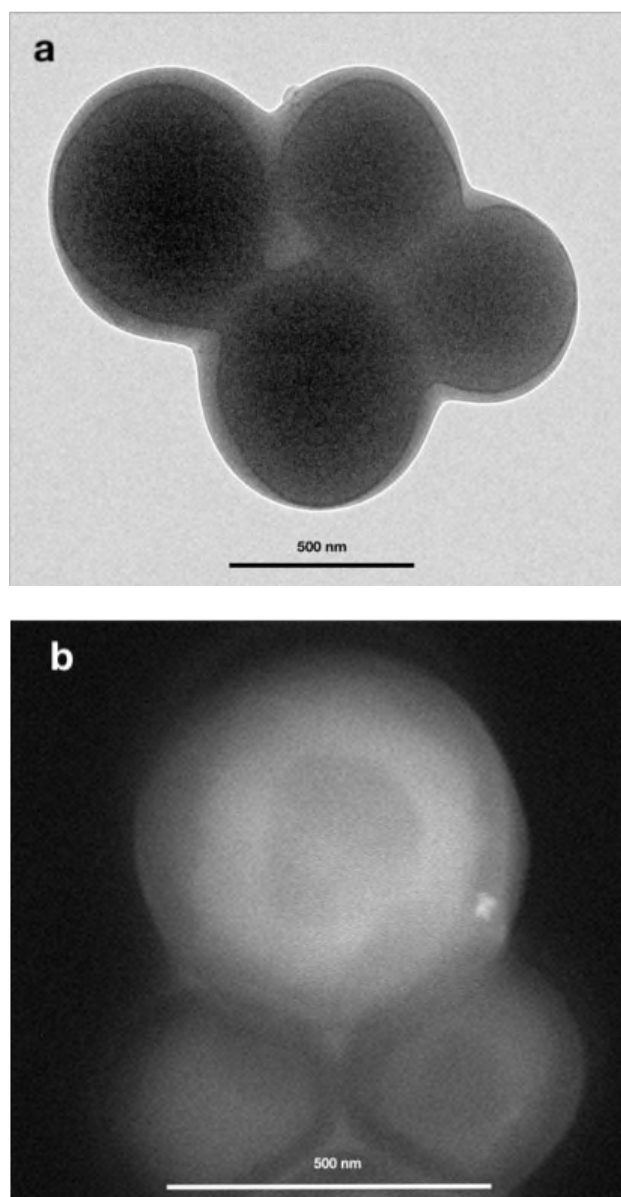


Figure 4.1 a) TEM and b) STEM-HAADF micrographs of PMB latex particles.

To do so, the morphology was further characterized analysing the cross-sections of the particles gathered by a novel sample preparation method. The thin cross-sections were then used in TEM and sSNOM (scattering-type Scanning Near-field Optical Microscopy) techniques to accurately determine the morphology of the particles.

4.3 TEM characterization of cryo-sectioned wet films

The most common way to analyze the internal morphology of latex polymer particles is by embedding the particles in a stable medium that does not react with the particles (i.e. epoxy resin or polyester resin), followed by ultramicrotomy of the resulting composite block². Although this sample preparation has been extensively used³, it has been reported that care should be taken because the epoxy resin might interact with the polymer particle and the original morphology can be affected⁴. Ideally, one would like to obtain a thin cross-section of the particle with a non interfering matrix.

With this idea in mind, we attempted a new sample preparation approach that considers frozen water as embedding medium. Namely, we froze the film formation process of the latex at a stage in which polymer particles are not yet in contact (close to the maximum packing of the particles) by using liquid nitrogen. The frozen block is then cryo-sectioned to obtain thin films to be used for further characterization.

Before showing the analysis of these thin films, a brief description of the film formation mechanism is appropriate here. The film formation of a latex can be divided in several steps⁵. Initially the polymer particles are dispersed in the water phase (Stage I) and, as soon as the water evaporates, they come into close contact forming a close packed array with water filled interstices (Stage II). During the transition to the next stage, interstitial water is lost and the particles are deformed, by Van der Waals and capillary forces, from spherical to hexagonal shape. Stage III is defined by a densely packed array in which the particles, despite their deformation, are still discrete and retain their identity. Thereafter, particles coalescence occurs (boundaries between particles disappear, reducing the total interfacial area), followed by the interdiffusion of the polymer chains between neighbouring particles. The last transition occurs only above the glass transition temperature of the polymer.

The moment at which each step of the film formation process occurs can be monitored by multispeckle diffusing wave spectroscopy⁶ (MDWS; for detailed information see the Appendix II.9). This technique is able to detect and to measure the particles' movement during the film formation along time.

For instance, Figure 4.2 shows the drying kinetics of a film cast from PMB latex using MDWS (100 μm wet film drying at 23 °C and RH=60%). The different steps of the film formation are distinguishable and hence it is possible to stop the process at the

time in which the residual water content is minimal and the polymer particles still retain their identity (original morphology) (Stage III).

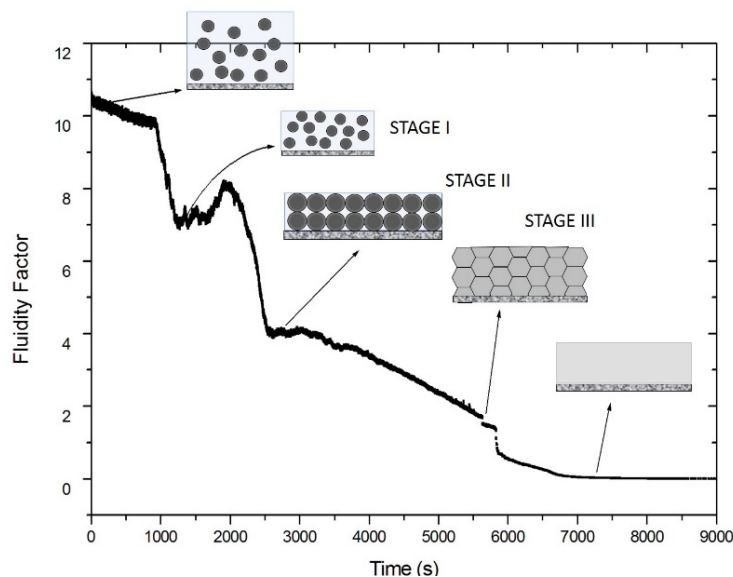


Figure 4.2 Drying kinetics profile of a film cast from PMB latex monitored by MDWS.

Based on this profile a sample of PMB latex was cast at approximately 1.5 h (6000s). Liquid N₂ was poured to freeze the process of film formation at an stage where polymer particles would still maintain their identity. The cryogenized film was immediately trimmed by ultracryomicrotomy in order to obtain a thin film suitable for other characterizations (TEM or sSNOM). Figure 4.3 shows the TEM micrograph of the ultramicrotomed PMB film; the boundaries of the particles are clearly visible confirming the suitability of the sample preparation method described above.

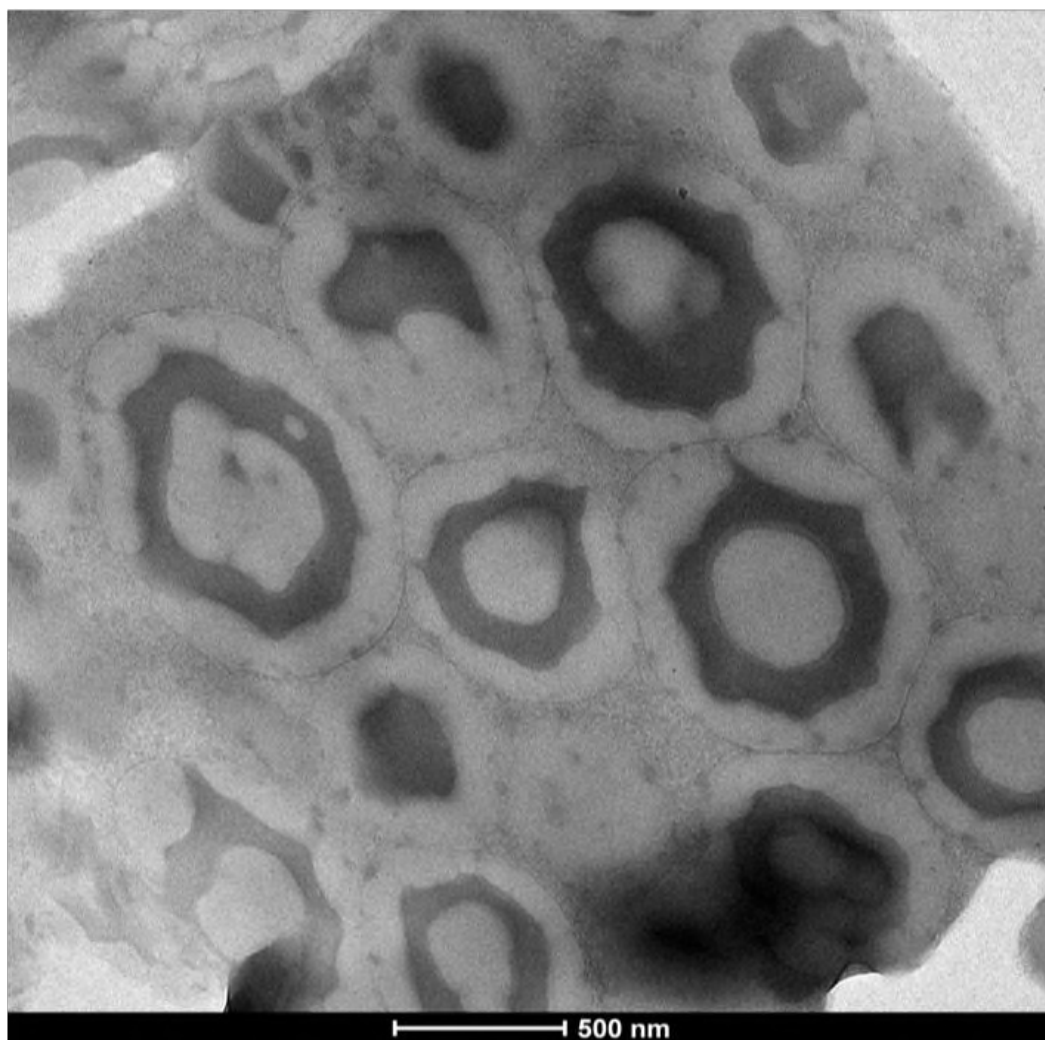


Figure 4.3 TEM micrograph of ultracryomicrotomed PMB film cast at 23 °C and RH=60% after the addition of liquid N₂. Note: in traditional TEM mode, the perfluorinated rich domains (highly electron dense) result darker than the conventional acrylic polymer.

Regarding the particle morphology, a core-shell-shell morphology is observed, with the inner shell presenting higher electron density (contrast) than the core and the outer shell, in agreement with the STEM-HAADF micrograph of Figure 4.1b. This result confirms that the POA enriched domain (darker region) phase separated from the MMA/BA enriched domains and it constituted the inner shell of the PMB latex particle. The fact that not all the particles in Figure 4.3 present the same morphology (i.e., some of them are core-shell-shell whereas others are core-shell or even particles with homogeneous morphology) can be found in the imperfect alignment of the (non monodisperse) particles during the film formation that, upon ultracryomicrotome slicing, resulted in a cross-section with particles trimmed at different heights (i.e. either at the core, at the first or the second shell heights).

This morphology was not expected because POA (although more hydrophobic than the other comonomers) is an acrylate monomer and it was assumed to have a reactivity ratio similar to n-butyl acrylate and hence it was expected that homogeneous particles would be formed. Furthermore, the similar contrast of the core and the external shell, in principle an indication of similar composition material, makes this morphology more intriguing; notably the mechanism by which such morphology was produced during semibatch emulsion polymerization is striking and worth analysing.

4.4 sSNOM characterization of cryo-sectioned wet films

The chemical composition of each of the phases of the core-shell-shell particle was determined using sSNOM, a novel technique that allows FTIR analysis at the nanoscale (see Appendix I.13 for details), based on the atomic force microscopy (AFM) technique in which the tip is irradiated with a monochromatic focused infrared light⁷⁻⁹. In addition to the topographical information, the backscattered light of the tip is detected by an interferometer that registers the phase and the amplitude with a resolution of approximately 20 nm⁹⁻¹¹.

The sSNOM technique was applied to the film obtained by the method described above, using as reference the FTIR spectra of poly POA homopolymer and a copolymer of BA and MMA with a 50/50 composition. The FTIR spectra of these references are shown in Figure 4.4.

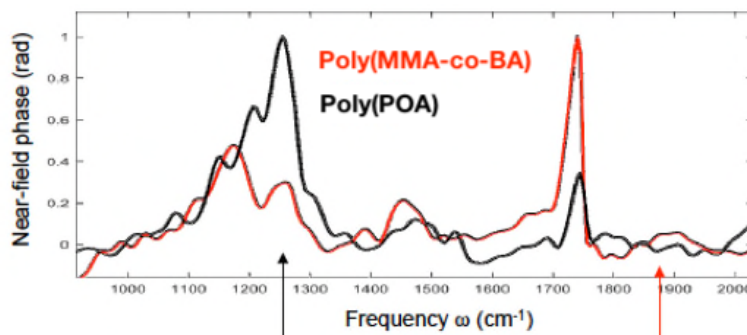


Figure 4.4 Nano-FTIR spectra of pure Poly(POA) and a Poly(MMA-co-BA) in the region of 900-2030 cm^{-1} .

The FTIR spectra of both polymers are similar but the regions at 1250 cm^{-1} (vibration band corresponding to the C-F bond) and at 1733 cm^{-1} (vibration corresponding to C=O bond) frequencies, show substantial differences that might allow to identify the reference polymers in a sample. Figure 4.5 presents topographical phase image and the spectral image normalized to the area of the C=O peak at 1733 cm^{-1} ; namely the intensity of this band is scaled from blue (0°) to red (40°) in the map.

Our interest is focussed on the spectral image because it can shed light on the composition of each of the phases observed in the TEM image in Figure 4.3. This spectral image identifies the core and the outer shell as rich in poly(MMA-co-BA) reference polymer and the inner shell as poor in this polymer, which can be seen as rich in POA polymer (indeed by normalizing the spectra to the band in 1250 cm^{-1} this inner shell presents the highest intensity and the core and the outer shell the lowest intensities). A more detailed analysis of the data can be done by plotting the spectra in different points of the three distinctive regions (core, inner shell and outer shell). Figure 4.6 presents the spectral image with indications of the points (P1-P9) where the FTIR spectra were collected, the corresponding spectra as well as the spectra of the references.

At first glance, the presence of the stretching band of C-F located at 1250 cm^{-1} in all the obtained FTIR spectra (3 for each region; P1,P2 and P3 in the core, P4, P6 and P7

in the inner shell and P7, P8 and P9 in the outer shell) indicated the presence of POA comonomer everywhere in the particle.

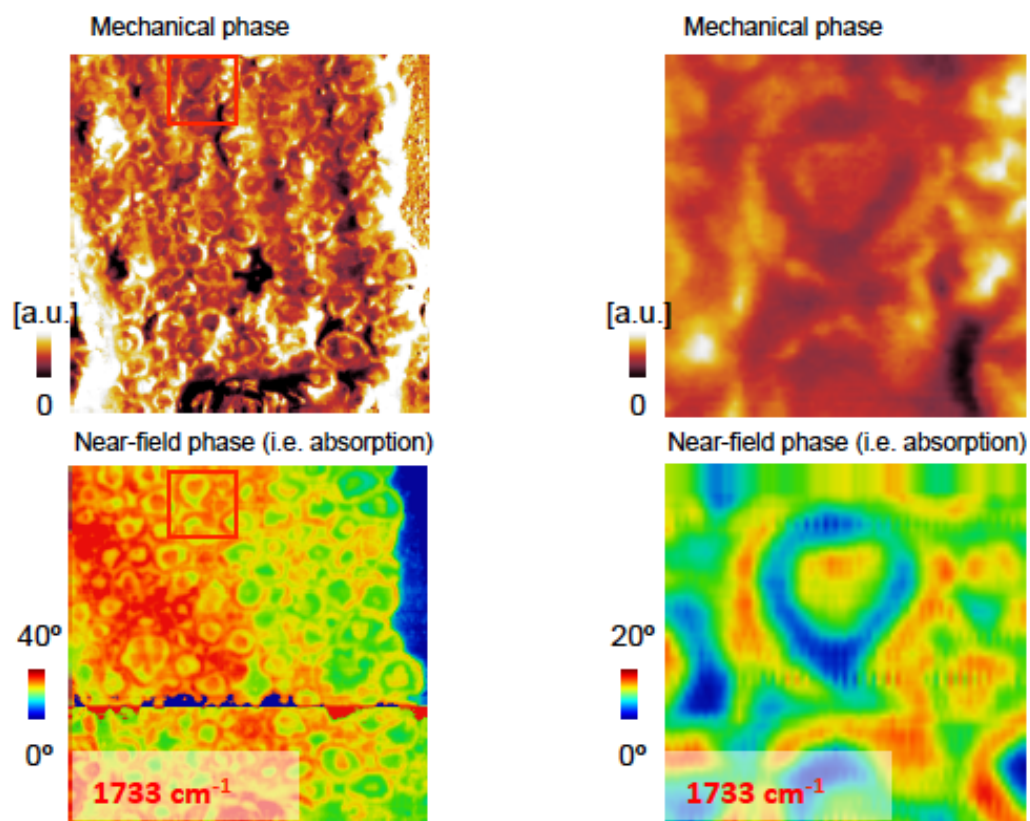


Figure 4.5 Mechanical phase and FTIR spectral (near field phase) image of the PMB thin film analysed by sSNOM ($8 \times 8 \mu\text{m}$ and $1 \times 1 \mu\text{m}$ images size).

This can be also seen in the average FTIR spectra (bottom spectra) that shows the most intense peak at 1250 cm^{-1} to be of the inner shell region (pink color). The average

spectra in the core (dark blue) presents a more intense peak than that in the outer shell (cyan). Note that both are more intense than poly(MMA-co-BA) reference at that wavenumber, which implies that likely there is POA in the three regions. A similar analysis and conclusion can be withdrawn from the peak at 1733 cm^{-1} for the poly(MMA-co-BA) in each region. The region with the lowest intensity at this frequency corresponds to the inner shell. In addition, one can estimate the ratio POA/MMA-co-BA at each spot by reconstructing the spectrum of each spot by linear superposition of the reference spectra. Figure 4.6 shows (right spectra) the reconstructed spectra of each spot and Table 4.1 shows the values of the ratio POA/MMA-co-BA calculated for the reconstructed spectra. As it can be seen, the values for the POA/MMA ratios are below one in all the cases. This indicates that none of the regions is pure POA (neither the inner shell as one could have inferred from the TEM image of Figure 4.3). The highest POA/MMA ratio is measured in the inner shell and the value is substantially higher than the value found in the core (0.66 vs 0.44). The lower value was found for the outer shell, clearly indicating the different compositions of the core and the outer shell that presented very similar contrast in the TEM image (Figure 4.3). Table 4.2 summarizes the information gathered from the TEM and sSNOM techniques for the PMB latex morphology.

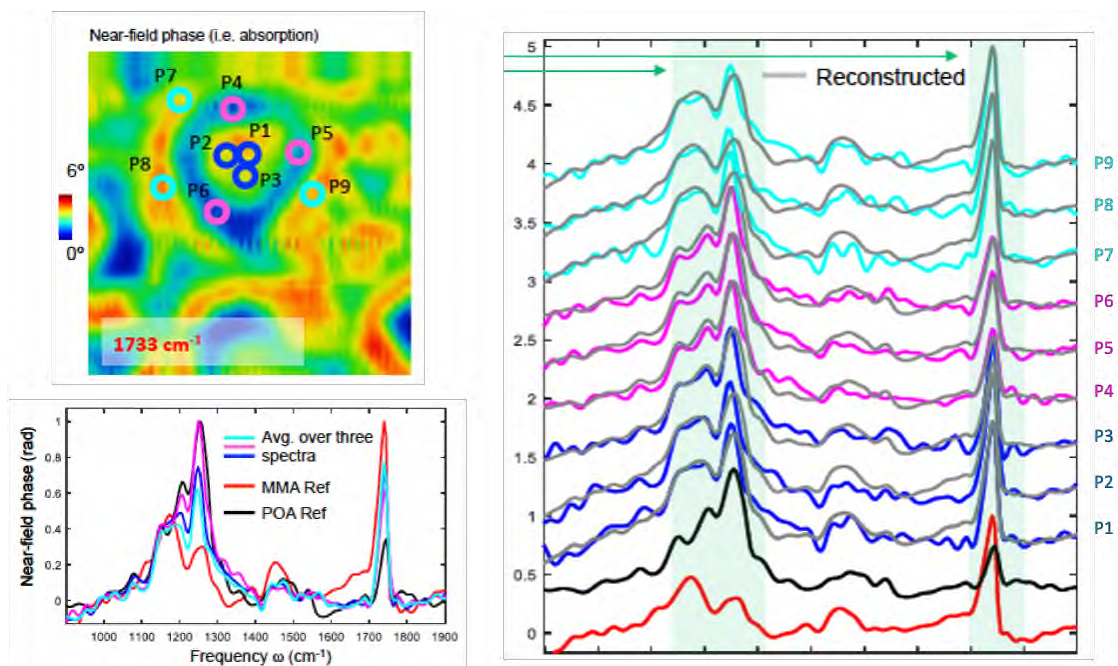


Figure 4.6 Spectral image and FTIR spectra obtained by sSNOM for PMB film. In the spectral image the spots where the FTIR were taken is indicated by P1-P9. The reference spectra, corresponding to pure PolyPOA (black) and pure Poly(MMA-co-BA) (red) are included. The right FTIR spectra also included the reconstructed spectra (in grey) calculated by superposition of the pure spectra for each position (P1-P9). The Bottom FTIR spectra plots the reference and the average values of the three spectra taken in each region (P1-P3 core, P4-P6 the inner shell and P7-P9 the outer shell).

Table 4.1 POA/MMA-co-BA ratio obtained from the superposition of reference spectra with the spectra collected in different particle regions (P1,P2 and P3 in the core, P4, P6 and P7 in the inner shell and P7, P8 and P9 in the outer shell).

	Position								
	Core			Inner shell			Outer shell		
	P1	P2	P3	P4	P5	P6	P7	P8	P9
POA/MMA-co-BA ratio	0.34	0.32	0.55	0.72	0.61	0.67	0.27	0.19	0.27
Average ratio	0.40			0.66			0.24		

Table 4.2. Summary of the data gathered for PMB latex film by TEM and sSNOM.

Morphology phase	POA composition (mol%)‡	Tg*	Fraction of particle's volume†
Core	29	Hard	10
Inner-shell	40	Soft	20
Outer-shell	19	Hard	70

* Topographical phase from sSNOM analysis

† Averaging the size of 20 core/shell/shell particles in TEM images of the thin film

‡ Calculated from POA/MMA-co-BA ratio.

The data in the table suggest that the core/shell/shell morphology is likely a non-equilibrium morphology based on the composition of each phase and their expected hydrophobicity. If an equilibrium morphology had been obtained we would have expected to have the most hydrophobic phase (the one containing higher amount of

POA) in core of the particle; but this was not the case. This might be an indication that a kinetically controlled morphology has been obtained, whose formation cannot be easily predicted without having accurate information of the kinetics of the polymerization, evolution of the individual conversion of each monomer and the evolution of the particle morphology along the reaction. However, the detailed morphology determined by the combination of TEM and sSNOM in a thin film can explain the SEM images for the films (Figure 3.11) and the poor anticorrosion performance of the films. In the SEM image not coalesced particles of size in the range 450-500 nm can be visualized, and interestingly this size is in good agreement with the size of the inner shell particles (see Figure 4.3) of the core-shell-shell morphology obtained. Due to the immiscibility of the POA rich inner shell in the poly(MMA-BA-POA) outer shell (with low POA content as revealed by sSNOM), this phase did not coalesce and phase separated producing non-homogeneous films of worse quality, that are more permeable than pure MMA/BA films.

This is likely the cause of the poorer performance of the fluorinated latexes and a clear example of the impact of the morphology of the polymer particles on the film properties and more specifically on the corrosion protection properties of the film. Therefore, it can be concluded that not only the composition of the polymer particles (more hydrophobic copolymer was sought by incorporating a fluorinated comonomer

in the formulation), but the particle morphology and their phases composition play a key role on the barrier and corrosion protection properties of the films and both must be correctly tuned to produce waterborne binders with outstanding anti-corrosion performance.

4.5 Conclusions

The copolymerization of perfluorooctyl acrylate (POA) comonomer with methyl methacrylate (MMA) and butyl acrylate (BA) by a seeded semibatch emulsion polymerization (as described in Chapter 3) generated latex particles with core-shell-shell morphology, which is likely the reason of the lack of particle coalescence observed in SEM analysis of the cross-sectioned film (Chapter 3). In fact, according to the morphological and compositional analysis, provided by TEM and sSNOM respectively, it has been found that a POA enriched phase separated from the rest of the particle and arranged in the inner-shell of the core-shell-shell morphology.

This result indicates that PMB particles presented a non-equilibrium morphology (if an equilibrium morphology was obtained we would have expected to have the POA enriched phase to be in core of the particle) and that a clear understanding of the causes that brought to this morphology is the key to overcome the film formation problem and hence to achieve outstanding anticorrosive properties.

4.4 References

1. Michler, G. H., *Electron microscopy of polymers*. Springer Science & Business Media: **2008**.
2. Michler, G. H., *Chapter 10-Preparation of Thin Sections: (Cryo)ultramicrotomy and (Cryo)microtomy*. Springer Science & Business Media: *Electron Microscopy of Polymers*, **2008**.
3. Stubbs, J. M.; Sundberg, D. C., A round robin study for the characterization of latex particle morphology—multiple analytical techniques to probe specific structural features. *Polymer* **2005**, *46* (4), 1125-1138.
4. Stubbs, J. M.; Sundberg, D. C., Core-shell and other multiphase latex particles—confirming their morphologies and relating those to synthesis variables. *Journal of Coatings Technology Research* **2008**, *5* (2), 169-180.
5. Keddie, J.; Routh, A. F., *Fundamentals of latex film formation: processes and properties*. Springer Science & Business Media: **2010**.
6. Brun, A.; Dhang, H.; Brunel, L., Film formation of coatings studied by diffusing-wave spectroscopy. *Progress in Organic Coatings* **2008**, *61* (2), 181-191.
7. Keilmann F; Hillenbrand R, *Nano-optics and near-field optical microscopy*. Artech House: Boston/London, **2008**.

8. Fritz, K.; Hillenbrand, R., Near-Field Microscopy by Elastic Light Scattering from a Tip. *Philosophical Transactions: Mathematical, Physical and Engineering Sciences* **2004**, *362* (1817), 787-805.
9. Hillenbrand, R.; Taubner, T.; Keilmann, F., Phonon-enhanced light-matter interaction at the nanometre scale. *Nature* **2002**, *418* (6894), 159-162.
10. Amenabar, I.; Poly, S.; Goikoetxea, M.; Nuansing, W.; Lasch, P.; Hillenbrand, R., Hyperspectral infrared nanoimaging of organic samples based on Fourier transform infrared nanospectroscopy. *Nature communications* **2017**, *8*, 14402.
11. Hermann, P.; Hoehl, A.; Patoka, P.; Huth, F.; Rühl, E.; Ulm, G., Near-field imaging and nano-Fourier-transform infrared spectroscopy using broadband synchrotron radiation. *Optics express* **2013**, *21* (3), 2913-2919.

Chapter 5

Use of ZnO nanoparticles as corrosion inhibitors in fluorinated acrylic polymer latexes

Part of this Chapter has been published in “**Effective incorporation of ZnO nanoparticles by miniemulsion polymerization in waterborne binders for steel corrosion protection**” *Journal of Coating Technology and Research* (2017) 14: 829.

5.1	Introduction.....	135
5.2	ZnO nanoparticles preliminary characterizations.....	137
5.2.1	ZnO nanoparticles wettability.....	137
5.2.2	Miniemulsion stability.....	139
5.3	Encapsulation of ZnO nanoparticles in perfluorinated latexes	142
5.3.1	Batch miniemulsion polymerization	142
5.3.2	ZnO nanoparticles encapsulation.....	144
5.3.3	Film formation on steel substrate.....	146
5.3.4	Corrosion evaluation.....	150
5.4	Encapsulation of ZnO nanoparticles in perfluorinated latexes containing Sipomer PAM200.....	155
5.4.1	Seeded semibatch emulsion polymerization.....	155
5.4.2	Nanohybrid latex morphology.....	156
5.4.3	Corrosion properties.....	158
5.5	Conclusions.....	160
5.6	References.....	162

5.1 Introduction

In the last two decades, helped by the advent of nanotechnology, inorganic nanoparticles have been also incorporated as pigments (e.g. cerium oxide (CeO_2)^{1,2}, silica (SiO_2)³, zinc oxide (ZnO)⁴⁻⁶ and zinc phosphate (ZnPO_4)⁷) in formulations of corrosion protection coatings⁸. The main advantage of the nanometric scale is the huge surface area provided by the interaction of the nanoparticles with the matrix that enhances substantially the properties of the hybrid material. Thus, ZnO nanoparticles have been incorporated to commercial alkyd resin dispersions and it was observed that small amounts (0.01-0.03 wt%) produced noticeable improvement in corrosion and mechanical properties of the coating⁹⁻¹¹. In fact, thanks to the nanometric scale and hence to the high surface area, the corrosion inhibition was efficiently distributed in the whole hybrid material. ZnO nanoparticles were also used in combination with an epoxy-polyamide resin and reduced hydrolytic degradation of the polymer matrix was observed⁶.

One of the main drawbacks of using nanoparticles is their high tendency to agglomerate. In this sense, Alvarez et al. found that the incorporation of 1wt% of ZnO nanoparticles led to agglomeration when incorporated to a sol-gel hybrid film¹². To avoid the agglomeration of the nanoparticles during film formation, different strategies can be used such as surface functionalization, already known as steric stabilization, or

the encapsulation into polymer particles. Miniemulsion polymerization is a powerful technique to obtain hybrid organic-inorganic materials in which nanoparticles are incorporated into or onto the polymer particles^{13,14}. Besides a better dispersion of the inorganic material in the polymeric matrix, this approach reduces the probability of aggregation of the nanoparticles in the film. However, in order to achieve the above-mentioned benefits from miniemulsion polymerization, one needs to efficiently encapsulate the inorganic nanoparticles into the polymer particles. This is not an easy task because several aspects related to the nanoparticles/monomer/polymer interaction play a key role on the successful encapsulation of the nanoparticles¹⁵⁻²¹.

Based on these premises, in this chapter we aimed to enhance the corrosion protection of the hydrophobic acrylic latexes, described in chapter 3 and 4 (PMB), by incorporating ZnO nanoparticles. Two types of commercial ZnO nanoparticles were used (one with hydrophobic and the other with hydrophilic functionalization on the surface) and the best way to incorporate them into the fluorinated acrylic latex have been investigated. Namely, the hydrophilic ZnO nanoparticles have been incorporated by mechanical blending with the already synthesized latex, whereas the hydrophobic ZnO nanoparticles by encapsulation into the polymer particles during the polymerization process. Subsequently, the influence of both the ZnO and the way of

incorporating them onto the corrosion properties of the resulting nanohybrid latexes has been investigated.

5.2 ZnO nanoparticles preliminary characterizations

5.2.1 ZnO nanoparticles wettability

The wettability of the nanoparticles in the monomer mixture plays a key-role affecting both the morphology and application properties of the final hybrid material. For this reason, the compatibility between the two types of commercial ZnO nanoparticles dispersion and different solvents has been evaluated; namely hydrophobic ZnO nanoparticles (NANOBYK 3841, dispersed in methoxy propyl acetate and labelled ZnO(MPA)) and hydrophilic nanoparticles (NANOBYK 3840, dispersed in water and labelled ZnO(H₂O)). The wettability of these ZnO nanoparticles in a monomer mixture composed of MMA/BA was assessed previously by Aguirre et al.²², but since in this case POA is included in the formulation, this test was repeated.

In detail, 1% wbm of ZnO (MPA) nanoparticles were dispersed both in water and in the monomer mixture (POA/MMA/BA =30/40/30 wt%; same composition of PMB latexes). Similar results of those obtained by Aguirre et al. were obtained (Figure 5.1); ZnO (MPA) nanoparticles dispersion in water was not stable whereas in the monomer mixture resulted stable and sedimentation did not occur after 24 hours. The opacity of

the dispersion of ZnO in monomers can be related to the ZnO nanoparticles size (85 nm as average according to the dynamic light scattering analysis). Moreover, powder wettability measurements were carried out for the hydrophobic ZnO. A fraction of ZnO (MPA) was dried at 60 °C overnight, grinded and the powder obtained was compacted to form a powder flat surface. The contact angle of the obtained powder bed to the monomer mixture and to water were measured obtaining values of 35° and 80° respectively. This result confirms the oleophilicity of the ZnO(MPA) nanoparticles.

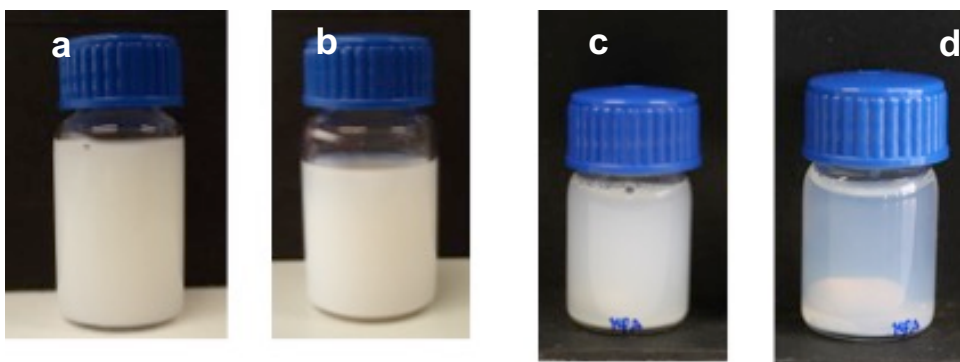


Figure 5.1. Dispersion of ZnO(MPA) nanoparticles in POA/MMA/BA 30/40/30 wt% monomer mixture after (a) 0h and b) 24h), and in water phase after (c) 0h and d) 24h).

The compatibility of ZnO (H₂O) nanoparticles was also evaluated in both monomeric mixture and water. As shown in Figure 5.2, they were not stable in the monomer phase while a good stability was achieved in water phase. As a result, it can be expected that

during the blending of the polymer latex with the ZnO (H₂O) nanoparticles, the ZnO will remain in the water phase.

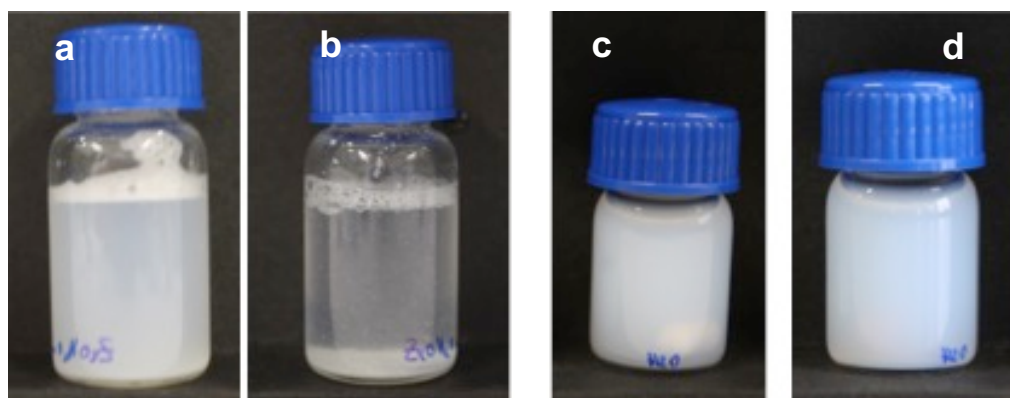


Figure 5.2. Dispersion of ZnO(H₂O) nanoparticles in POA/MMA/BA 30/40/30 wt% monomer mixture after (a) 0h and b) 24h, and in water phase after (c) 0h and d) 24h.

5.2.2 Miniemulsion stability

The evaluation of miniemulsion stability in the presence of ZnO(MPA) nanoparticles is a necessary step for a proper waterborne nanohybrid latex design. In detail, two miniemulsions with 40 wt% monomers phase (based on the total weight) were prepared (composition is listed in Table 5.1). Namely, 2.5 wbm % of ZnO(MPA) nanoparticles were added to the monomer phase and stirred at 700 rpm for 10 minutes. The aqueous phase consisted on 2 wbm% of surfactant dissolved in water. The surfactants employed were the phosphate surfmer Sipomer PAM200, labelled SIP, and a commercial anionic

surfactant DOWFAX 2A1 labelled DOW; as in Chapter 3 when SIP was used, pH was adjusted to avoid hydrolysis. To produce the miniemulsion, both the organic phase and the aqueous phase were brought together and the mixture was stirred for 15 minutes at 700 rpm. Then the coarse preemulsion was sonified for 15 minutes (operating at 8-output control and 70% duty cycle in an ice bath and under magnetic stirring) and the stability of the resulting miniemulsions was evaluated.

Table 5.1 *ZnO(MPA)/POA/MMA/BA hybrid miniemulsion recipes.*

		Miniemulsion (g)	
		A	B
Oil phase	POA	6	6
	MMA	8	8
	BA	6	6
	ZnO (MPA)	0.5	0.5
Water phase	SIP	-	0.4
	DOW	0.4	-
	WATER	30	30
Stability		yes	no

Surprisingly, when SIP was used, the miniemulsion B resulted unstable and massive droplets coagulation occurred instantaneously, whereas a colloidal stable dispersion was achieved by using DOW (A). This finding indicates that ZnO (MPA) nanoparticles could interact with the deprotonated phosphate groups of SIP in neutral pH conditions

and hence cause miniemulsion destabilization. Moreover, the high extent of this detrimental interaction could be related to the fact that ZnO nanoparticles are located preferentially close to the monomer droplet surface as reported in a previous work carried out by Aguirre et al.²².

The interaction of phosphate ions with ZnO has been described in literature^{23,24}; in fact, in a recent study of Everett and co-workers²⁴, they found that ZnO nanoparticles readily react with phosphate ions to form zinc phosphate ($Zn_3(PO_4)_2$) crystallites.

In order to confirm the possible interaction SIP-ZnO (MPA) further stability tests were carried out. 0.5 g of ZnO(MPA) and 0.4 g of SIP were added to 30 g of water and mixed under magnetic stirring at ambient temperature. The resulting mixture was stable at pH=3; however, as soon as the pH was increased to 7, a yellowish coagulum appeared immediately in the solution which corroborate our hypothesis of the fast interaction between the nanoparticles and the phosphate groups of the Sipomer. The presence of SIP in the coagulum has been confirmed by MALDI analysis (Appendix III.4.1), but for the sake of readiness they are not reported here.

Based on these preliminary results, it was concluded that both components cannot be employed in the same reaction step. However, according to the synthetic method proposed by Aguirre et al.²², first we performed the synthesis of a nanohybrid latex stabilized by conventional anionic surfactant (DOWFAX that is not reacting with the

nanoparticles) in order to evaluate the efficiency of ZnO encapsulation and the anticorrosion properties. Then, the incorporation of phosphates functionalities of SIP was carried out by a semibatch process. In this way, we envision that the interaction between the ZnO nanoparticles, encapsulated in the seed particles, and SIP surfmer, added in the second step, would be minimized allowing the production of a stable latex with encapsulated ZnO nanoparticles and with phosphate functionalities that produce a phosphatization layer during the film formation (as shown in Chapter 2).

5.3 Encapsulation of ZnO nanoparticles in perfluorinated latexes

5.3.1 Batch miniemulsion polymerization

All the reactions were performed batchwise. In a typical formulation, POA, MMA and BA (30/40/30 wt%) were mixed to produce the oil phase; in the case of the synthesis of the nanohybrid latex (PMB_DZnO), a certain amount of ZnO(MPA) dispersion (1 weight based on the monomers percent, wbm%, of ZnO) was added to the monomer mixture. The aqueous solution was produced by mixing 3 wbm% of Dowfax 2A1 in MiliQ water. Both oil and aqueous solutions were mixed under magnetic stirring for 15 min and then they were mixed together for 15 additional

minutes. Subsequently, the oil in water coarse emulsion was sonicated for 15 min (operating at 8-output control and 70% duty cycle in an ice bath and under magnetic stirring) allowing the formation of the miniemulsion. Table 5.2 presents the recipes used for the synthesis of the pristine polymer latex (PMB_D) and the ZnO containing nanohybrid polymer latex (PMB_DZnO).

Table 5.2 Batch miniemulsion polymerization recipes of PMB_D and PMB_DZnO.

Sample	POA (g)	MMA(g)	BA (g)	ZnO(MPA) (g)	AIBN (g)	DOW (g)	H ₂ O (g)
PMB_D	14.53	19.04	14.60	-	0.49	1.61	76.90
PMB_DznO	14.57	19.15	14.44	1.26	0.48	1.68	73.34

The batch miniemulsion polymerizations were carried out in a 250 mL glass jacketed reactor fitted with a reflux condenser, sampling device, N₂ inlet and a stainless steel stirrer rotating at 200 rpm. When the temperature reached 70 °C, the initiator was introduced into the reactor (AIBN, 1% wbm) and the reaction was kept running for 4h.

For comparison purposes, a blend of the pristine latex with waterborne ZnO nanoparticles was also prepared (labelled BLEND). A certain amount of ZnO (H₂O) dispersion (1% wbm of ZnO nanoparticles) was blended with the previously synthesized latex (PMB_D). Then the mixture was stirred by magnetic stirring at ambient temperature for 4 hours in order to obtain a homogeneous latex.

5.3.2 ZnO nanoparticles encapsulation

Figure 5.3 displays the time evolution of the overall conversion and average particle size respectively during the batch miniemulsion polymerization of PMB_D and PMB_DznO.

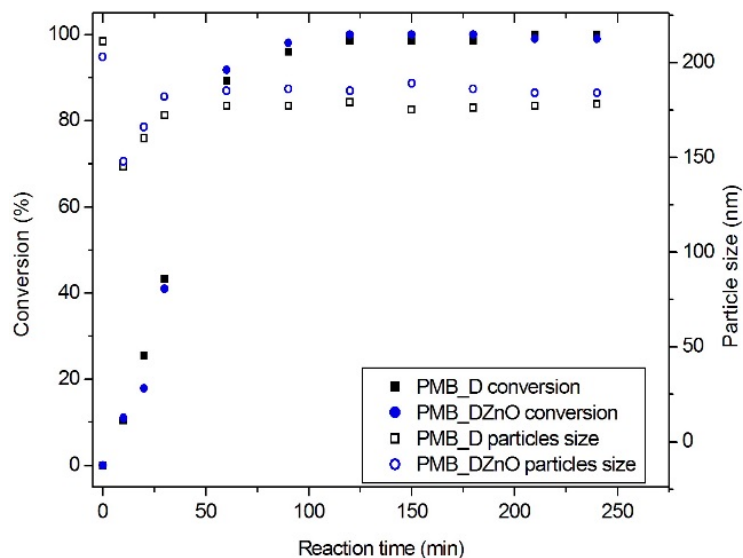


Figure 5.3. Evolution of the overall monomer conversion and z-average particle size for PMB_D and PMB_DznO.

It can be observed that the addition of ZnO (MPA) nanoparticles had no significant effect on the kinetics of the polymerization. On the other hand, slightly larger particle size values were obtained when nanoparticles were present in the formulation.

Similarly to the results of Aguirre et al.²², the micrographs in Figure 5.4 show that not all the polymer particles contain ZnO nanoparticles (darkest regions), and notably no ZnO nanoparticles could be found in the aqueous phase. The incorporation was expected based on the wettability measured for the ZnO(MPA) nanoparticles (Figure 5.1). TEM pictures confirm the incorporation of ZnO nanoparticles in PMB_DZnO latex.

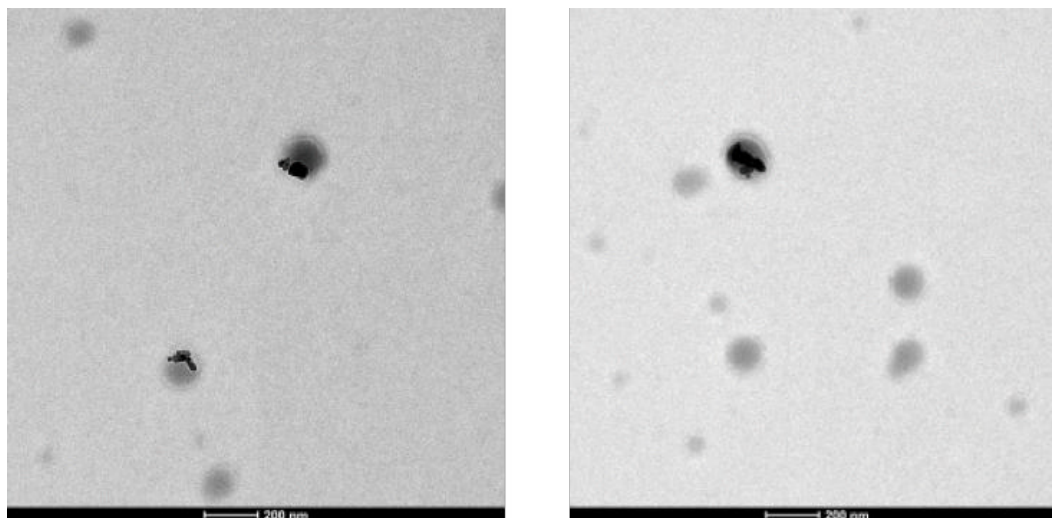


Figure 5.4. *TEM micrographs of PMB_DZnO nanohybrid latex with ZnO(MPA) associated to the polymer particles.*

5.3.3 Film formation on steel substrate

The presence of ZnO nanoparticles did have a huge effect upon casting the latexes on steel substrates at 23 °C and RH=60%. As it can be seen in Figure 5.5, the casting of pristine latex (PMB_D) produced severe flash rust on the steel surface, while films containing ZnO nanoparticles (PMB_DZnO and BLEND) did not produce such a extended flash rust. This reproducible result suggests the beneficial effect of the presence of ZnO (either free in the water phase, or associated to polymer particles) on the anticorrosion properties of waterborne latexes. However, it is worth mentioning that when ZnO (H₂O) were blended with PMB_D (BLEND), the resulting film showed inhomogeneities on the surface (Figure 5.5b) and some flash rust was observed.

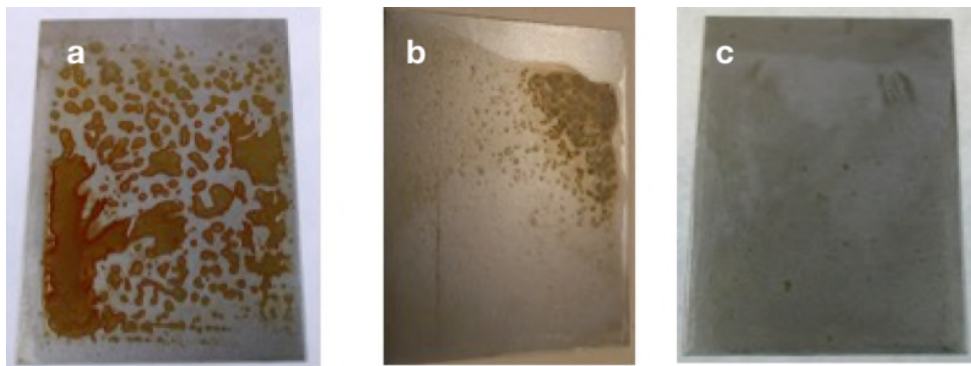


Figure 5.5. *Steel substrates coated with a) PMB_D, b) BLEND and c) PMB_DZnO latexes.*

In order to shed light on the different behaviour of the three latexes regarding flash rust, the water evaporation rate during film formation on steel substrates was determined (Figure 5.6). It can be seen that the water evaporation from the PMB_D latex is 40 min slower than the BLEND (around 200 min versus 160 min), which could be the reason for the formation of the flash rust in the former case. However, the slower water evaporation is likely not the only reason for the substantial flash rust observed for PMB_D latex and, because of that the cross sections of three films were analysed by SEM (Figure 5.7).

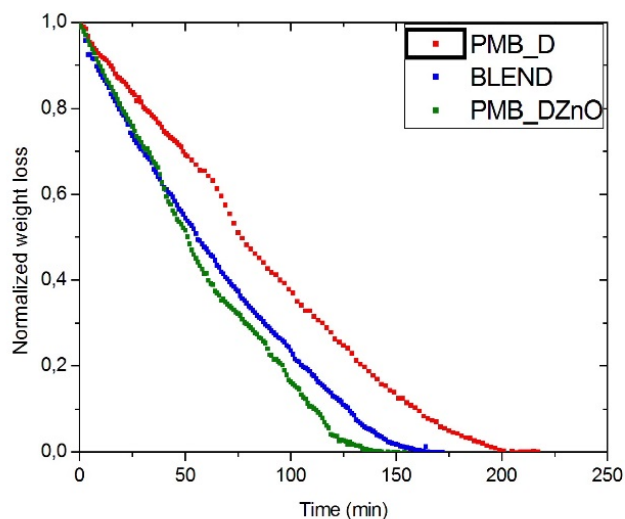


Figure 5.6. *Water loss during the film formation of latexes on steel substrate.*

The first conclusion that can be drawn from these images is the bad film formation of the BLEND where the roughness, likely induced by the ZnO nanoparticles

aggregation, was substantially higher than in the film cast from PMB_DZnO and PMB_D. However, similarly to the latex described in Chapter 3 (PMB with SIP), the lack of particles coalescence during the film formation was appreciated in the case of films cast from PMB_D and PMB_DZnO latexes.

Even if the quantification done with the EDX should be taken with care (due to the low concentration of the nanoparticles used in this work and the thick films employed), in both cases the concentration of Zn on the top of the films (0.2 % for BLEND and 1.1 % for PMB_DZnO) was lower than the concentration found at the bottom (0.7 % for the BLEND and 2.8 % for PMB_DZnO). Therefore, it can be concluded that both ZnO nanoparticles and hybrid polymer particles having a higher density than the neat polymer particles, sedimented faster and consequently water evaporation of these latexes was faster. In the case of BLEND, the ZnO nanoparticles present in the water phase would sediment alone or could drag some polymer particles in their sedimentation to the steel substrate. On the other hand, the polymer particles in PMB_DZnO having ZnO nanoparticles would sediment to the bottom. This faster sedimentation could produce the faster covering of the steel substrate with a ZnO/polymer layer, which would then prevent the contact between the steel and the water, and subsequently the flash rust that this contact could produce.

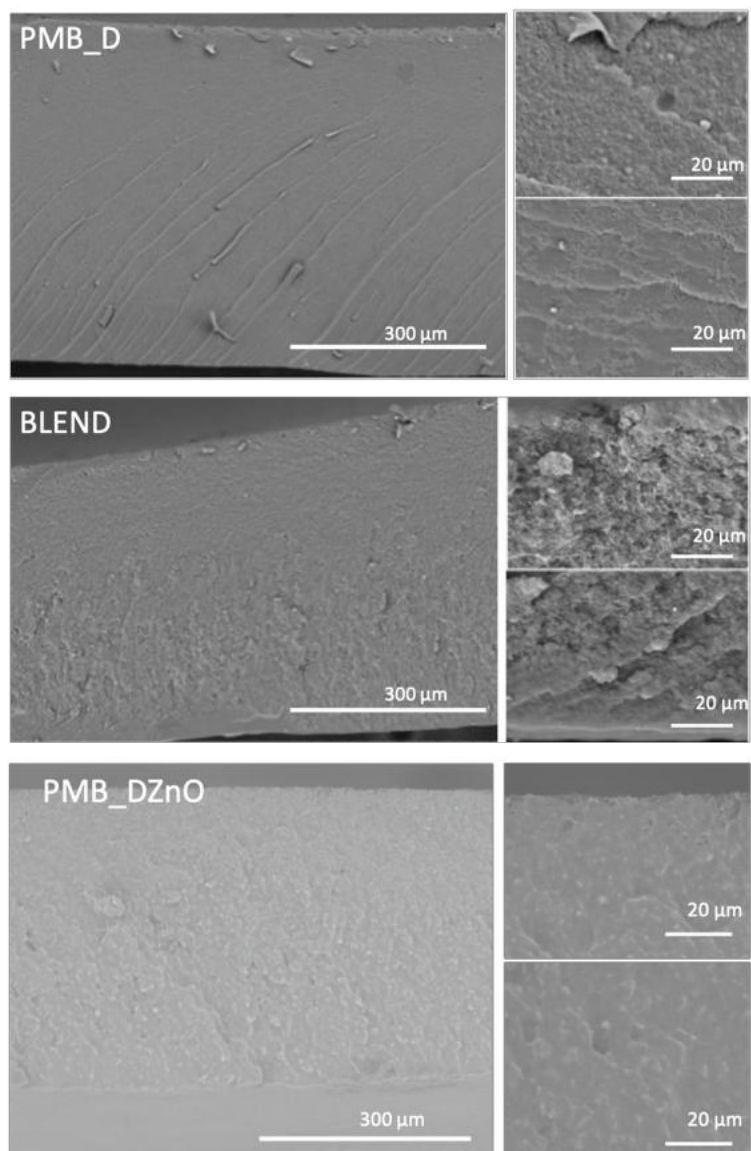


Figure 5.7. SEM of the cross sections of the films formed from latexes *PMB_D*, *BLEND* and *PMB_DZnO*.

5.3.4 Corrosion evaluation

In order to evaluate the corrosion protection of ZnO nanoparticles present in the waterborne binders, bare steel (used as a reference material) and coated steel specimens (PMB_D, PMB_DZnO and BLEND) were tested by electrochemical impedance spectroscopy (EIS).

Figure 5.8 presents the Bode plot for all the systems studied. Film cast from PMB_D latex showed poor corrosion protection; in fact, due to the lack of coalescence of PMB films, corrosive species are free to permeate through the coating, to reach the metal surface and then to trigger the corrosion (in PMB films of Chapter 3, the presence of passive iron phosphate layer held back the corrosion). Contrary to our expectations, although the flash rust was restrained, the addition of hydrophilic ZnO nanoparticles to the latex by mechanical blending did not produce any enhancement with respect to corrosion protection and low impedance value at low frequency range was measured. Indeed, corrosion protection provided by either ZnO or the presence of a hydrophobic surface may be hindered by the bad film formation observed through the film (BLEND in Figure 5.7) and the heterogeneity in the nanoparticle distribution in the film. On the other hand, the corrosion resistance notably increased four orders of magnitude (with respect to PMB_D) when hybrid acrylic/ZnO binders with encapsulated ZnO nanoparticles were used as coating. This substantial improvement in the corrosion

protection is likely due to lack of aggregation of ZnO nanoparticles and the accumulation of ZnO containing polymer particles (higher density) at the film-substrate interface, which reduced electrolyte penetration and increased coating resistance.



Figure 5.8. a) Bode plots and b) phase angle plot after 3h of immersion in 3.5 wt% NaCl.

Undoubtedly, corrosion protection has been enhanced by the incorporation of ZnO nanoparticles in acrylic binders (PMB_DZnO). Moreover, the decrease in the flash rust for this system might be due to the increase of the local shifting of the pH by the presence of ZnO²⁵ (an increase of the pH can impair the corrosion by shifting the reaction equilibrium towards the metal in the reduced state) and to the faster water evaporation (Figure 5.6) rather than an effective corrosion inhibition.

This finding confirms that the incorporation of ZnO into polymer particles during miniemulsion polymerization has a synergistic effect improving homogeneity and barrier properties as can be drawn from the impedance diagram presented in Figure 5.9 in which the variation of impedance modulus of PMB_DZnO, at different immersion times in NaCl 3.5 wt% solution (0, 11, 70 and 115 h), is plotted.

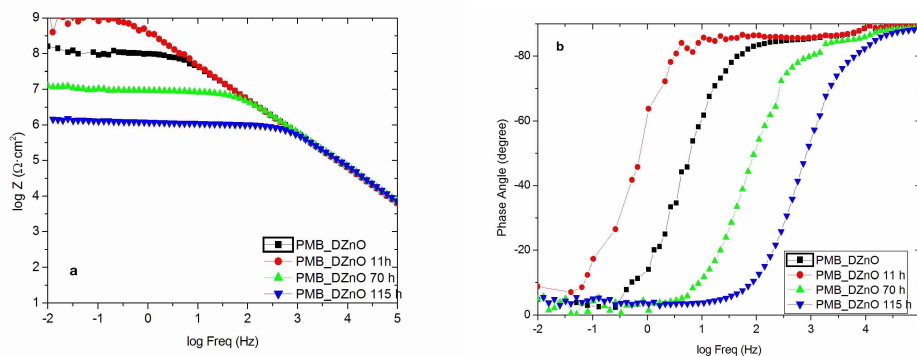


Figure 5.9. *a) Bode plots and b) phase after different time of immersion (3, 11, 70 and 150 h) in 3.5 wt % NaCl for PMB_DZnO coated specimens.*

Initially, the impedance diagrams show a single time constant at any time. However, electrolyte uptake or permeation through the coating was expected due to the presence of pinholes in the PMB polymer matrix (see Chapter 4 for detailed descriptions) and hence the contact between the nanoparticles and electrolyte occurred. It is well known that the stable form of zinc in aqueous solutions is Zn^{2+} , which favors tetrahedral coordination and undergoes significant hydrolysis forming several mononuclear and polynuclear species²⁶. This means that the surface of zinc oxide in water suspension is transformed to hydroxide (eg. $Zn(OH)_2(s)$) and it is in equilibrium with the solution which contains hydroxide complexes that can be represented by the formula $Zn(OH)_{i(aq)}^{2-i}$ ($i=1-4$)²⁷. The solubility of zinc oxide/hydroxide is strongly dependent of the pH (i.e., ZnO has an isoelectric point at $pH \approx 9.0$ ²⁸ and it is not stable in the pH range between 7.2 – 12.0²⁷) and therefore it is expected to have leaching of soluble species from the ZnO nanoparticle to the coating since the beginning of the test, once local alkalization or acidification takes place to dissolve zinc oxide/hydroxide.

Then, the increase of impedance in one order of magnitude from 3 h to 11 h of immersion for PMB_DZnO system may be explained by (i) the migration of aqueous species of zinc to damaged areas (e.g., cracks)¹² and (ii) active inhibition thanks to the role of ZnO nanoparticles⁵ (e.g. local pH changes in the defects/pinholes can trigger the precipitation of insoluble compounds or recrystallization of mixed zinc corrosion

products that act as passive sealants). Later on, the impedance decreased progressively with time (70 and 115 h, respectively) as it is shown in Figure 5.9. Such variation indicates that the resistance is decreasing most probably due to depletion of the corrosion protection capabilities of the ZnO nanoparticles rather than a degradation of the coating itself. Therefore, the role of well-distributed pigments (i.e. ZnO nanoparticles), acting as a corrosion inhibitor in a polymeric matrix, is crucial as it is shown here for coating cast from PMB_DZnO latex.

To sum up, the highlights of this section are the following; ZnO nanoparticle encapsulation has been carried out by batch miniemulsion polymerization with DOWFAX as stabilizer. ZnO nanoparticles showed the ability to enhance the corrosion protection of “relatively bad” film like PMB_D; in fact, despite the presence of a defective polymeric film, corrosion protection is quite high at the beginning of the EIS measurement. Nevertheless, such protection seems to be affected with immersion time due to the depletion of the active protection provided by the ZnO nanoparticles.

In the next section, we aimed at incorporating phosphate surfactant (SIP) to the nanohybrid latex PMB_DZnO by means of seeded semibatch emulsion polymerization, while increasing the solids content up to 50%.

5.4 Encapsulation of ZnO nanoparticles in perfluorinated latexes containing Sipomer PAM200

5.4.1 Seeded semibatch emulsion polymerization

Due to the strong interaction between the phosphate groups of SIP and the ZnO, the employment of seeded semibatch emulsion polymerization in which the ZnO nanoparticles were incorporated in the seed while the SIP was added in the second step (as in Chapter 3) resulted a successful strategy that provides a final coating with homogeneous ZnO nanoparticles distribution.

Seeded semibatch emulsion copolymerizations were carried out according to the procedure described in section 3.2 (Chapter 3) with the addition of ZnO nanoparticles in the seed preparation. The resulting latex was labelled PMB_DSZnO.

In order to produce hybrid latexes with the highest ZnO nanoparticle incorporation efficiency and the lowest coagulum content, several process variables were varied such as the way ZnO nanoparticles were incorporated or the emulsifier amount used in the seed polymerization (list of reactions is reported in the Appendix III.4.2). In Table 5.3 a representative optimum formulation is presented.

Table 5.3. Formulation used to synthesize PMB_DSZnO waterborne binder.

Component		Miniemulsion (seed) (g)	Preemulsion (g)
Oil phase	POA	28.5	-
	MMA	3.75	34.25
	BA	3.75	24.75
	AIBN	0.36	-
	ZnO	0.36	-
Aqueous phase	Water	84	11
	DOW	0.72	-
	SIP	-	1.9

5.4.2 Nanohybrid latex morphology

The nanohybrid latex produced by seeded semibatch emulsion polymerization of POA/MMA/BA comonomers with the incorporation of ZnO nanoparticles led to a final latex with average particle size of 489 nm, close to the theoretical value of 506 nm. Similarly to the polymerization of PMB latex in Chapter 3, this result indicates stable particle growth with some secondary in the presence of ZnO nanoparticles.

The ZnO encapsulation has been confirmed by TEM analysis; in fact, a significant number of polymer particles (Figure 5.10) contained ZnO aggregates with an average size of 120 nm (ZnO nanoparticles aggregate average size in the initial dispersion in MPA was 85 nm). Furthermore, the nanoparticles were mainly located near the surface of the polymer particles, which was also confirmed by a tilt series of TEM images

(Figure 5.11). This result indicates that the ZnO nanoparticles have been encapsulated in the polymer particles, although close to the interface, and that they were not present in the aqueous phase.

Similar morphology was already found in recent works where CeO₂ or ZnO^{29,30} and CdSe/ZnS with CeO₂³¹, have been encapsulated using the same method (seeded semibatch emulsion polymerization) incorporating the inorganic nanoparticles in the seed production process by miniemulsion polymerization.

In the following section the anticorrosion properties have been evaluated and compared with the ones of the latex synthesized in the batch process.

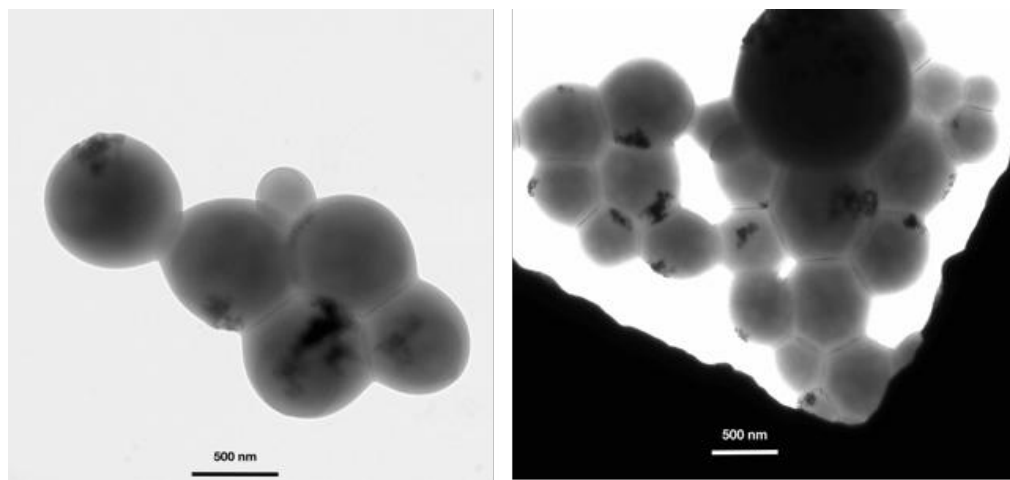


Figure 5.10. TEM micrographs of hybrid latex PMB_DSZnO.

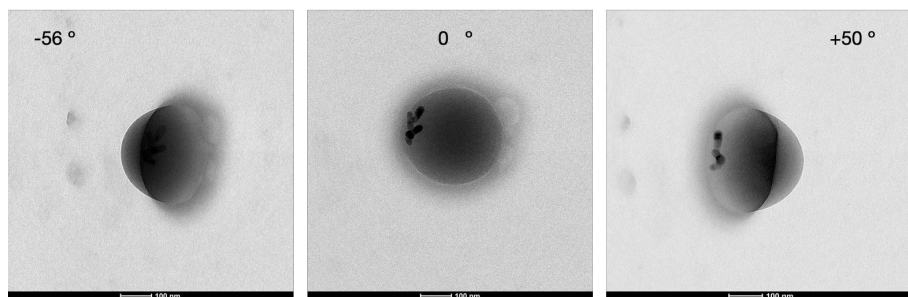


Figure 5.11. TEM micrographs of tilted hybrid latex particle (-56° and $+50^\circ$).

5.4.3 Corrosion properties

The Bode plot of PMB_DSZO after different immersion time in NaCl 3.5 wt% solution (0 and 500 h) is reported in Figure 5.12 and for comparison purposes, the Bode plot of the latex that did not contain SIP (after 0 and 144 h of immersion), is also included (see section 5.3 (PMB_DZnO)).

Notably corrosion protection has been enhanced by introducing the SIP in the formulation of PMB_DZnO; in fact, the impedance modulus at low frequency range presents high values after 500 h of immersion in NaCl 3.5 wt% solution, whereas in the case of films cast from latex that did not contain SIP in the formulation (PMB_DZnO), the impedance were lower and dropped to $10^6 \Omega \text{ Cm}^2$ after 115 h of immersion.

Nevertheless, despite the improved corrosion resistance in mild condition, with respect to the film cast from PMB_DZnO, specimens coated with PMB_DSZO did

not provide sufficient corrosion protection in harsh conditions of salt spray test. As it can be seen in Figure 5.13, the specimens underwent a significant degradation after 144 h of exposure to salt-spray. It is noteworthy that, in comparison with specimens coated with PMB_S (Figure 3.9 in Chapter 3), in this case the film, cast from PMB_DSZnO latex, was able to protect the steel substrate at least for 24 h (the specimen resulted rust-free after 24 h). This result indicates that the incorporation of ZnO nanoparticles provide additional corrosion protection but, due to the intrinsic bad film morphology of films containing the perfluorinated monomer (PMB), is not able to provide complete protection in harsh conditions.

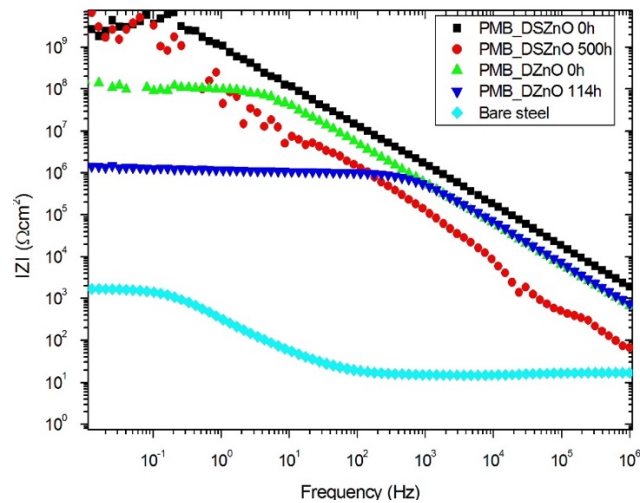


Figure 5.12 Bode plot of specimens coated PMB_DSZnO and PMB_DZnO after 0 and 500 h and 0 and 144 h of immersion in 3.5 wt% NaCl solution respectively.

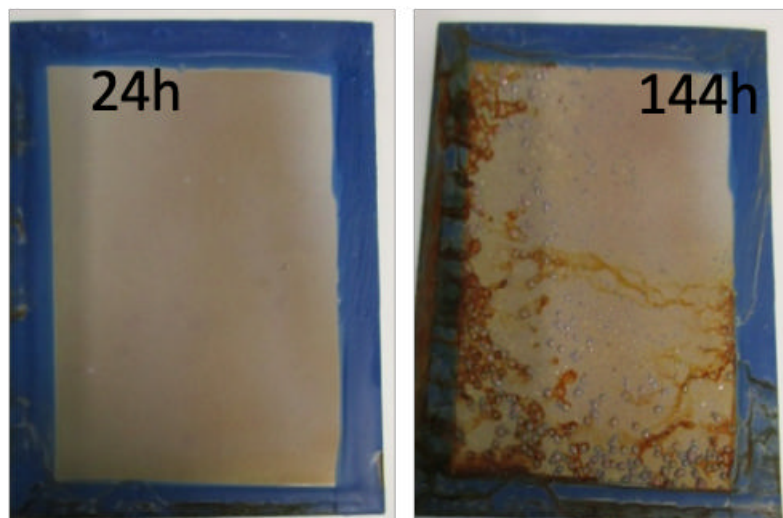


Figure 5.13 *PMB_DSZnO specimens after 24 and 144 h of exposure to salt spray test.*

5.5 Conclusions

PMB/ZnO waterborne hybrid latexes were developed and their anticorrosion protection on steel substrates was evaluated. The coatings cast from the neat PMB_D and blends of a pristine latex and ZnO water dispersion (BLEND) latexes showed negligible improvement against an aggressive electrolyte (NaCl 3.5 wt% solution), due to their heterogeneity in the morphology and to oxidation of the metallic interface during the film formation. The incorporation of ZnO nanoparticles by merely blending is not enough to improve the corrosion protection, despite it was able to reduce the flash rust formation.

The improvement of the corrosion resistance was much more significant when the ZnO nanoparticles were homogeneously distributed in the film by their encapsulation in the polymer particles achieved by batch miniemulsion polymerization. This indicates a synergetic effect between the ZnO nanoparticles and the polymeric matrix in terms of corrosion protection which was confirmed by the increase of the coating resistance (barrier effect), and by the active protection thanks to the release of Zn^{2+} based compounds during exposure to NaCl 3.5% solution.

Thereafter, the incorporation of phosphate functionalities on the surface of the nanohybrid polymer particles was achieved by a seeded semibatch emulsion polymerization process in which the ZnO nanoparticles were incorporated in the seed preparation process (by miniemulsion polymerization) and the phosphate groups, belonging to the SIP, were gradually added during the semibatch process. In this way, the interaction between the inorganic nanoparticles and the SIP was avoided in favour of the corrosion protection synergy of the in-situ phosphatization (provided by SIP) and the inhibition properties of ZnO nanoparticles. Unfortunately, despite the good corrosion protection in mild conditions, the encapsulation of ZnO nanoparticles produce just a moderate enhancement of the corrosion protection in harsh conditions, when compared with the analogous system without the nanoparticles (substrate coated with PMB_DSZnO start to corrode after 24 h of exposure in salt spray chamber instead

of immediately after being exposed to the salt spray like PMB coated substrate; see Chapter 3). This result indicates that the incorporation of ZnO nanoparticles is not enough to overcome the problem of the lack of coalescence of polymer particles containing perfluorinated moieties that induces phase separation.

5.6 References

1. Montemor, M. F.; Ferreira, M. G. S., Analytical characterization of silane films modified with cerium activated nanoparticles and its relation with the corrosion protection of galvanised steel substrates. *Progress in Organic Coatings* **2008**, *63* (3), 330-337.
2. Ecco, L.; Fedel, M.; Ahniyaz, A.; Deflorian, F., Influence of polyaniline and cerium oxide nanoparticles on the corrosion protection properties of alkyd coating. *Progress in Organic Coatings* **2014**, *77* (12), 2031-2038.
3. Ji Yeon, S.; Mijeong, H., Multi-functional hybrid coatings containing silica nanoparticles and anti-corrosive acrylate monomer for scratch and corrosion resistance. *Nanotechnology* **2011**, *22* (2), 025601.
4. El Saeed, A. M.; El-Fattah, M. A.; Azzam, A. M., Synthesis of ZnO nanoparticles and studying its influence on the antimicrobial, anticorrosion and mechanical behavior of polyurethane composite for surface coating. *Dyes and Pigments* **2015**, *121*, 282-289.

5. Rostami, M.; Rasouli, S.; Ramezanzadeh, B.; Askari, A., Electrochemical investigation of the properties of Co doped ZnO nanoparticle as a corrosion inhibitive pigment for modifying corrosion resistance of the epoxy coating. *Corrosion Science* **2014**, *88*, 387-399.
6. Ramezanzadeh, B.; Attar, M. M., Studying the effects of micro and nano sized ZnO particles on the corrosion resistance and deterioration behavior of an epoxy-polyamide coating on hot-dip galvanized steel. *Progress in Organic Coatings* **2011**, *71* (3), 314-328.
7. Nabih, N.; Herrmann, U.; Glasser, G.; Lieberwirth, I.; Landfester, K.; Taden, A., Water-based hybrid zinc phosphate-polymer miniemulsion as anticorrosive coating. *Progress in Organic Coatings* **2013**, *76* (4), 555-562.
8. Zheludkevich, M. L.; Serra, R.; Montemor, M. F.; Ferreira, M. G., Oxide nanoparticle reservoirs for storage and prolonged release of the corrosion inhibitors. *Electrochemistry communications* **2005**, *7* (8), 836-840.
9. Dhoke, S. K.; Khanna, A. S., Study on electrochemical behavior of Nano-ZnO modified alkyd-based waterborne coatings. *Journal of Applied Polymer Science* **2009**, *113* (4), 2232-2237.
10. Dhoke, S. K.; Khanna, A. S.; Sinha, T. J. M., "Effect of nano-ZnO particles on the corrosion behavior of alkyd-based waterborne coatings. *Progress in Organic Coatings* **2009**, *64* (4), 371-382.

11. Shi, H.; Liu, F.; Han, E.; Wei, Y., Effects of nano pigments on the corrosion resistance of alkyd coatings, *Journal of Materials Science and Technology* **2007**, *23* (4), 551-558.
12. Álvarez, D.; Collazo, A.; Nóvoa, X. R.; Pérez, C., Assessment of ZnO nanoparticles as anticorrosive pigment in hybrid sol–gel films. *Progress in Organic Coatings* **2016**, *96*, 3-12.
13. Landfester, K.; Weiss, C. K., Encapsulation by Miniemulsion Polymerization. In *Modern Techniques for Nano- and Microreactors/-reactions*, Caruso, F., Ed. Springer Berlin Heidelberg: Berlin, Heidelberg, **2010**; pp 1-49.
14. Asua, J. M., Miniemulsion polymerization. *Progress in Polymer Science* **2002**, *27* (7), 1283-1346.
15. Mičušík, M.; Bonnefond, A.; Reyes, Y.; Bogner, A.; Chazeau, L.; Plummer, C.; Paulis, M.; Leiza, J. R., Morphology of Polymer/Clay Latex Particles Synthesized by Miniemulsion Polymerization: Modeling and Experimental Results. *Macromolecular Reaction Engineering* **2010**, *4* (6-7), 432-444.
16. Liu, Y.; Chen, X.; Wang, R.; Xin, J. H., Polymer microspheres stabilized by titania nanoparticles. *Materials Letters* **2006**, *60* (29–30), 3731-3734.
17. Zhang, S.-W.; Zhou, S.-X.; Weng, Y.-M.; Wu, L.-M., Synthesis of SiO₂/Polystyrene Nanocomposite Particles via Miniemulsion Polymerization. *Langmuir* **2005**, *21* (6), 2124-2128.

18. Cauvin, S.; Colver, P. J.; Bon, S. A. F., Pickering Stabilized Miniemulsion Polymerization: Preparation of Clay Armored Latexes. *Macromolecules* **2005**, *38* (19), 7887-7889.
19. Tiarks, F.; Landfester, K.; Antonietti, M., Silica Nanoparticles as Surfactants and Fillers for Latexes Made by Miniemulsion Polymerization. *Langmuir* **2001**, *17* (19), 5775-5780.
20. Asua, J. M., Mapping the Morphology of Polymer–Inorganic Nanocomposites Synthesized by Miniemulsion Polymerization. *Macromolecular Chemistry and Physics* **2014**, *215* (5), 458-464.
21. Paulis, M.; Leiza, J. R., Encapsulation with Miniemulsion Polymerization. In *Encyclopedia of Polymeric Nanomaterials*, Kobayashi, S.; Müllen, K., Eds. Springer Berlin Heidelberg: Berlin, Heidelberg, 2014; pp 1-10.
22. Aguirre, M. Waterborne acrylic/metal oxide binders for UV blocking clear coats. *PhD Thesis UPV/EHU*, Donostia-San Sebastian 2014.
23. Lv, J.; Zhang, S.; Luo, L.; Han, W.; Zhang, J.; Yang, K.; Christie, P., Dissolution and Microstructural Transformation of ZnO Nanoparticles under the Influence of Phosphate. *Environmental Science & Technology* **2012**, *46* (13), 7215-7221.

24. Everett, W. N.; Chern, C.; Sun, D.; McMahon, R. E.; Zhang, X.; Chen, W.-J. A.; Hahn, M. S.; Sue, H. J., Phosphate-enhanced cytotoxicity of zinc oxide nanoparticles and agglomerates. *Toxicology Letters* **2014**, *225* (1), 177-184.
25. Kalenda, P., Anticorrosion pigments and derived coating systems on their basis. *Dyes and Pigments* **1993**, *23* (3), 215-223.
26. Zhang, Y.; Muhammed, M., Critical evaluation of thermodynamics of complex formation of metal ions in aqueous solutions: VI. Hydrolysis and hydroxo-complexes of Zn²⁺ at 298.15 K. *Hydrometallurgy* **2001**, *60* (3), 215-236.
27. Degen, A.; Kosec, M., Effect of pH and impurities on the surface charge of zinc oxide in aqueous solution. *Journal of the European Ceramic Society* **2000**, *20* (6), 667-673.
28. Müller, B.; Kläger, W., The effect of pH on the corrosion inhibition of zinc pigments by phenol derivatives. *Corrosion Science* **1996**, *38* (11), 1869-1875.
29. Aguirre, M.; Paulis, M.; Leiza, J. R.; Guraya, T.; Iturrondobeitia, M.; Okariz, A.; Ibarretxe, J., High-Solids-Content Hybrid Acrylic/CeO₂ Latexes with Encapsulated Morphology Assessed by 3D-TEM. **2013**, *214* (19), 2157-2164.
30. Aguirre, M.; Barrado, M.; Iturrondobeitia, M.; Okariz, A.; Guraya, T.; Paulis, M.; Leiza, J. R., Film forming hybrid acrylic/ZnO latexes with excellent UV absorption capacity. *Chemical Engineering Journal* **2015**, *270* (0), 300-308.

31. De San Luis, A.; Paulis, M.; Leiza, J. R., Co-encapsulation of CdSe/ZnS and CeO₂ nanoparticles in waterborne polymer dispersions: enhancement of fluorescence emission under sunlight. *Soft Matter* **2017**, *13* (44), 8039-8047.

Chapter 6

Synergic effect of semicrystalline nanodomains and in-situ phosphatization on the anticorrosion properties of waterborne latexes

Part of this chapter has been included in an international patent application (PCT/EP-2019/052860) entitled "**A Method for Providing Coating Systems with Corrosion-Protective Properties**"

6.1	Introduction	171
6.2	Synthesis of phosphate Poly(SA-co-MMA-co-BA) latexes with core-shell morphology	173
6.3	Influence of nanocrystalline domains on the barrier properties of the final coating.....	178
6.4	Corrosion protection of waterborne latexes containing nanocrystalline domains.....	184
6.5	Conclusions	192
6.6	References	193

6.1 Introduction

An efficient way to enhance the barrier properties of coatings, is the incorporation of nanometric fillers, with high aspect ratio, in the polymeric phase. Van der Wel and Adan ¹ stated that the use of inorganic fillers, can lower the water diffusion in the coating provided that they are homogeneously dispersed; in fact, it has been seen that incomplete dispersion could lead to the formation of absorption sites and hence to an overall rise in water permeability ^{2, 3}. Within the large variety of nanofillers, the incorporation of high aspect ratio of two dimensional (2D) nanoparticles into polymeric matrices, such as graphene sheets (GO) or inorganic clays (IC) nanoplatelets, notably decreased the permeability to moisture and gases of hybrid coatings ⁴⁻⁶. Nevertheless, it is worth mentioning that, for 2D nanoparticles the orientation play a key role; randomly dispersed platelets are less effective in reducing the permeability than when they are well aligned and perpendicularly oriented with respect to the penetrating molecules direction ⁷. In solventborne systems, well aligned and homogeneously dispersed GO and IC have been successfully prepared by melt processing or simply solution casting^{4, 8}. However, it is more challenging to obtain the same grade of homogeneity and order, in waterborne polymer dispersions. Homogeneity can be easily obtained by mechanical blending, for fillers stable in the water phase, and through miniemulsion polymerization⁹⁻¹³ or by RAFT initiated polymerization from the surface

of the nanofiller^{14, 15, 16} in the case of hydrophobic particles. On the other hand, perpendicular alignment of the filler during the film formation has not been obtained so far. Additionally, in the case of incorporation into the polymer particles, platelets-shape inorganic nanoparticles have a tendency to be located at the interface of the polymer particles- aqueous phase rather than in the interior of the polymer particles¹⁴. This morphology might favor the aggregation of the nanofillers during film formation and hence a reduction in the barrier properties of the film. In fact, water can accumulate at the interface platelet-polymer and provide a pathway for its diffusion. Since water clustering at the interface happens with different extent in all hybrid systems^{17, 18}, a potential alternative to avoid lack of cohesion between the permeable polymer and the impermeable filler, could be obtained by using of semicrystalline polymers¹⁹⁻²¹. For instance, Mehravar et al. have found that the introduction of semicrystalline poly stearyl acrylate (PSA) nanodomains or methacrylate side-chain liquid crystal polymers (SCLCPs), in waterborne latexes formulation, lowers water and oxygen permeability combined with good cohesion between the crystalline and the amorphous phase²²⁻²⁴. Based on the promising barrier performance achieved by the incorporation of semicrystalline nanodomains in waterborne binders, we have designed a waterborne binder for corrosion protection that will combine the ability to in-situ produce a phosphatization layer during the film application (as already seen in Chapter 2), and

the enhanced barrier properties characteristic of coatings containing crystalline nanodomains that would reduce the permeability of agents that might initiate corrosion. The influence of the introduction of nanocrystalline domains onto the film formation and barrier properties have been deeply investigated. Furthermore, anticorrosion properties were assessed in both mild and harsh corrosive environments by immersion in liquid (NaCl 3.5 wt% solution) and by salt-spray exposure (NaCl 5 % salty fog) respectively. For all the tested samples, electrochemical impedance spectroscopy (EIS) has been used as non-destructive test to monitor the evolution of the coating with the time.

6.2 Synthesis of phosphated Poly(SA-co-MMA-co-BA) latexes with core-shell morphology

Core-shell latexes (PSA core and poly (MMA-co-BA) shell) were synthesized following the polymerization strategy proposed by Mehravar et al.^{23, 25, 26}, but using the surfmer Sipomer PAM200 as polymerizable surfactant. The polymerization strategy is briefly described in this section. Latexes were synthesized by seeded semibatch emulsion polymerization and the recipes for the synthesis of the seeds and for the final latexes are summarized in Tables 6.1 and 6.2.

In a typical formulation to produce a latex of 45 % solids content, the whole amount of SA, that represents the oil phase of the seed miniemulsion, was added to the aqueous phase composed by Dowfax 2A1 surfactant (DOW) and deionized water in a solution at 2 wt%. Both oil and aqueous phases were mixed together under magnetic stirring for 15 minutes. Subsequently, the oil/water dispersion was sonicated using a Branson Sonifier 450 for 15 min (operating at 8-output control and 70% duty cycle in an ice bath and under magnetic stirring), allowing the formation of the miniemulsion. The polymerization was started by loading the miniemulsion in the reactor and heating up to 70 °C. Once the reaction temperature was reached, the initiator was introduced as a shot (1% wbm of AIBN) and the miniemulsion was left to polymerize to produce in-situ the seed latex (labelled SA40s or SA50s). After 3 hours, a second shot of initiator (0.5 % wbm of KPS) was introduced into the reactor and a preemulsion based on the shell monomer mixture (MMA/BA), water and 2 wbm% of Sipomer PAM200 (SIP) was fed for 3 hours (Table 6.2). pH neutralization, by addition of ammonia solution, of the preemulsion containing SIP was necessary to incorporate the surfmer into the system, as very acid or very basic conditions would hydrolyze the ester linkage of the phosphate group. After the end of the preemulsion feeding, the reaction was post-polymerized for an additional hour to get rid of any unreacted monomer and to reach a final solids content of 45 %. The difference between SA40 and SA50 latexes was the

SA comonomer amount in the polymer composition; namely 40 and 50 wbm%, respectively.

Table 6.1. *Batch miniemulsion polymerization recipes to produce the seeds.*

SEED		Miniemulsion (g)	
		SA40s	SA50s
Oil phase	SA	90	112.5
	DOW	1.8	2.25
Water phase	WATER	247.5	247.5
	NaHCO ₃	0.144	0.144
Initiator shot	AIBN*	0.45	0.56

* *Solution in 5 g of monomer.*

Table 6.2. *Seeded semibatch emulsion polymerization recipes to obtain semicrystalline latexes.*

LATEX	Seed (g)	MMA (g)	BA (g)	KPS (g)	SIP (g)	Water(g)
SA40	339.9	67.5	67.5	0.675	4.5	27.5
SA50	362.9	56.2	56.2	0.560	4.5	27.5

The poly(MMA/BA) latex synthesized using Sipomer PAM200 (labeled as MB, see Chapter 2) was used as reference (latex without nanocrystalline domains).

Table 6.3 presents the sizes of the miniemulsion droplets, seed particles and the final latex for SA40 and SA50 experiments as well as the theoretical particle size predicted for the final latexes assuming that no secondary nucleation occurs during the semibatch polymerization.

Table 6.3. *Droplet and particles size of miniemulsion, SA seed and final latexes.*

LATEX	Droplet size (nm)	Seed particles size (nm)	Final particles size (nm)	Theoretical final particles size (nm)*
SA40	199	187	176	229
SA50	167	173	173	192

* *Calculated assuming that the number of particles of the seed was maintained constant during the semibatch process, without coagulation or secondary nucleation.*

Table 6.3 shows that the PSA seed particles have similar sizes than the miniemulsion droplets, which is an indication of a predominant droplet nucleation mechanism during the miniemulsion polymerization. In the subsequent semibatch polymerization the final particle sizes were substantially smaller than the expected sizes. The reason was the low ratio of seed particles surface area to the volume of water (low number of seed particles at the beginning of the semibatch polymerization). These results are in good

agreement with the results of Mehravar et al. that also observed a substantial amount of secondary nucleation during the feeding of MMA/BA to PSA seed particles²³.

Despite secondary nucleation, most of the polymer particles presented core-shell morphology as it can be seen in Figure 6.1, that presents TEM images of the SA40 and SA50 final latexes. Figure 6.1 shows a distinctive core-shell morphology; in fact, it is clearly visible a sharp boundary between the darker core, which is related to the electron dense semicrystalline domains of PSA, and the rather transparent shell that belongs to the acrylate moieties (poly(MMA-co-BA)).

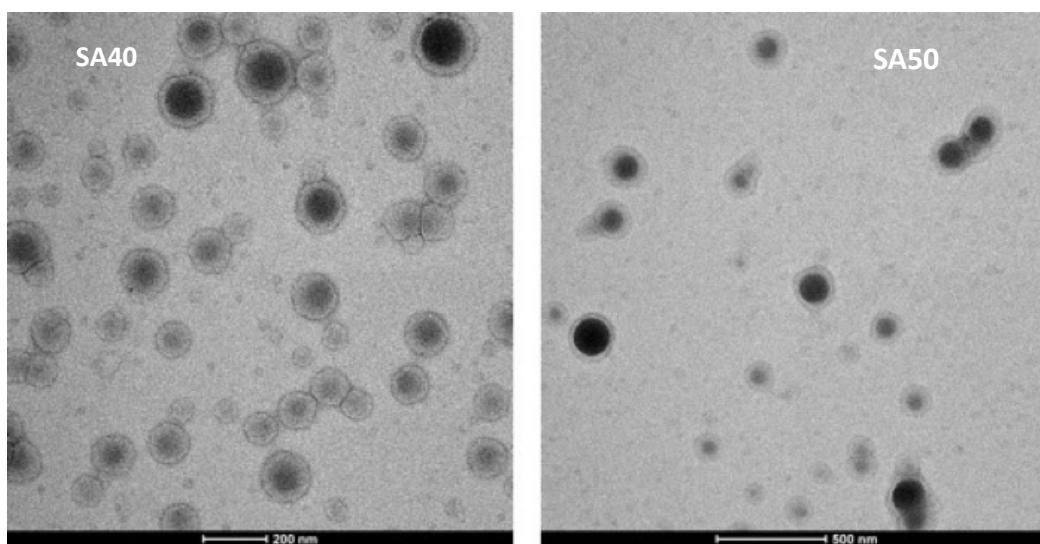


Figure 6.1. TEM micrographs of SA40 and SA50 latex particles.

6.3 Influence of nanocrystalline domains on the barrier properties of the final coating

TEM micrographs (Figure 6.2) of cross sectioned films cast from latexes SA40 and SA50 offer the opportunity to observe the homogeneous dispersion of the PSA nanodomains into the polymeric matrix by the presence of well defined dark zones which belong to the electron dense crystals.

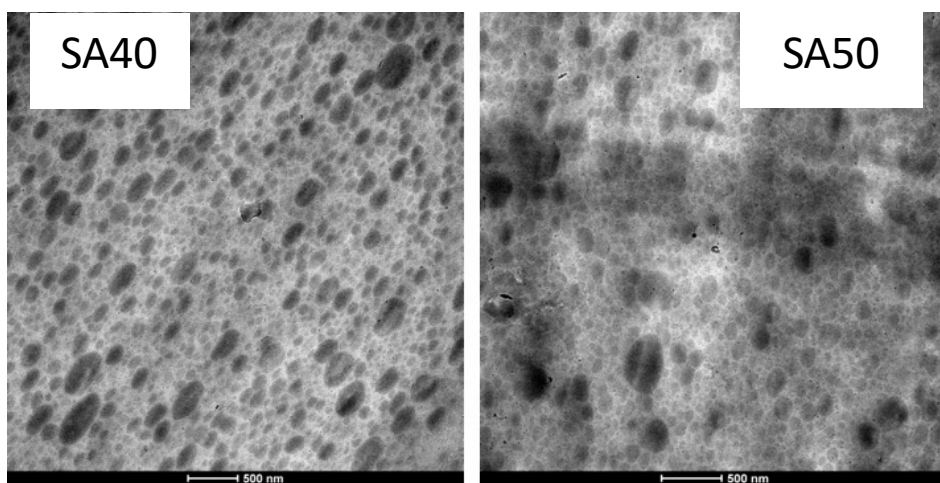


Figure 6.2. TEM micrographs of cross section of films cast from SA40 and SA50 latexes at room temperature.

As already mentioned before, the aim of this work is to enhance the barrier properties of the coating through the design of a composite like material in which the semicrystalline PSA nanodomains, that are cohesive with the amorphous matrix, act as

physical barrier against the diffusion of water. The total amount of water transported through the coating per unit of time can be determined by the water flux equation (Equation 1)^{27,28}:

$$\text{Water flux} = -P * \left(\frac{\Delta p}{\text{film thickness}} \right) \quad (\text{Eq. 1})$$

Where Δp is the water concentration gradient and P is the permeability coefficient that characterizes the water transport through the coating. It is well known that the permeation mechanism is a combination of diffusion and dissolution processes and hence the permeability coefficient (P) can be defined as the product of solubility (S) and diffusivity coefficients (D)²⁸⁻³⁰ (Equation 2).

$$P = D * S \quad (\text{Eq. 2})$$

The diffusivity (D) is a kinetic factor that represents the rate of permeant molecules sorption in the polymer. It is influenced by the morphology of the coating and is described by the Fickian diffusion model³¹⁻³³. On the other hand, the solubility (S) is a thermodynamic factor that is related to the interactions that could occur between the permeant molecules and the polymer matrix and it is described by different sorption isotherms (Henry's isotherm^{33,34} for water sorption in hydrophilic polymers while Flory-Huggins or BET isotherms³³ for water sorption in relatively hydrophobic polymers). As it can be seen, these coefficients are strongly related to both the physico-

chemical nature and the morphology of the polymer coating. For instance, it has been reported that composite materials^{35, 36} and semicrystalline polymers^{20, 37} reduce the permeability of water through the coating (when compared with the pristine polymer). The inclusion of fillers or crystals, in which water is not soluble, reduces the availability of the permeable volume of polymer (decrease in S value) and increases the tortuosity of the diffusion path (decrease in D value).

One way to determine quantitatively the extent of water permeation through a polymer is by the water uptake analysis. Figure 6.3 presents the water uptake results for SA40 and SA50 films cast at room temperature and at 60 °C, and that of MB (poly(MMA-co-BA)) reference film cast at room T.

As it can be seen in Figure 6.3, the water uptake in the SA films, dried at ambient temperature (SA40 and SA50), was higher than in of the reference (MB) film without the semicrystalline domains. Although there is no information in the open literature about the influence of crystalline cores on the film formation of core-shell latexes, we think that a possible explanation to this unexpected result might be attributed to the presence of the crystalline nanodomains. Thus, they could impose certain constrain to the amorphous phase surrounding them and reduce the mobility of polymer chains during the coalescence. This would cause the formation of excess of free volume, that would act as adsorption sites for water molecules.

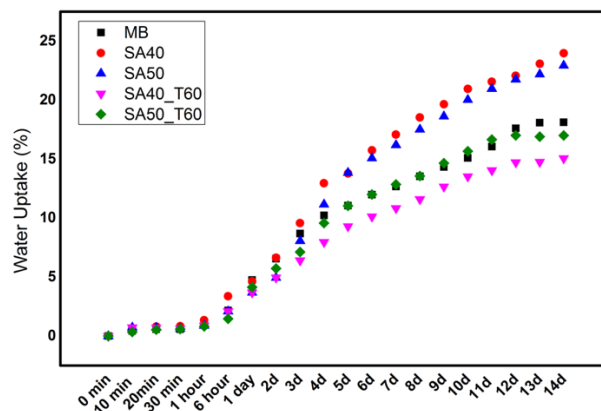


Figure 6.3. *Liquid water uptake of the films cast at 23 °C and 60 °C.*

Generally, the diffusion of water into a polymeric film is influenced by the availability of sorption sites and by the amount of water in the dried film; the more water is present, the higher is the dielectric constant of the system and hence the more water will be able to diffuse through the polymeric matrix^{38,39}. For this reason, in order to compensate the mobility constrain imposed by the crystalline cores and to reduce the amount of interstitial water⁴⁰, a drying temperature above the melting point of PSA crystals was used (60 °C) and the water uptake was measured again. Figure 6.3 shows that for SA40 and SA50 latexes cast at 60 °C, the water uptake substantially reduced

with respect to latexes cast at ambient temperature and moreover the water uptake was similar or lower than the one of the reference MB latex.

The reduction of water uptake when drying the films at higher temperature could be related with an increase of the crystallinity of the films. In order to asses if this was the cause DSC analysis of the SA40 and SA50 films produced at 23 °C and at 60 °C were performed. Figure 6.4 presents the second heating scan DSC traces.

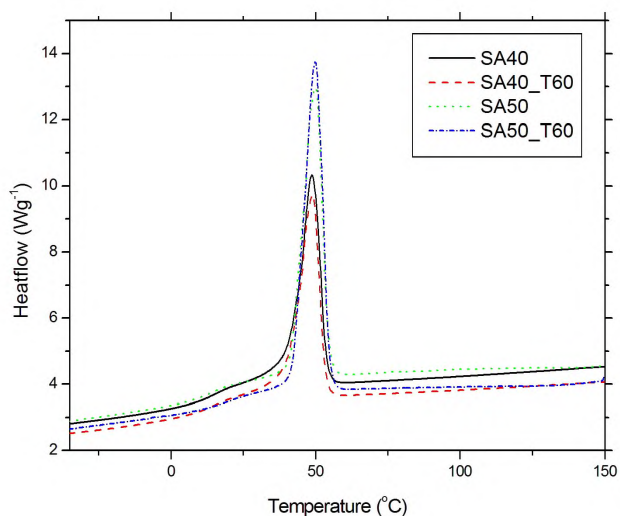


Figure 6.4. *Second DSC heating scan for SA40 and SA50 dried at 23 °C and at 60 °C.*

All the traces presented the endothermic peak at 50 °C corresponding to the crystalline poly(SA) and a second order transition which corresponded to the

amorphous poly(MMA-co-BA) phase at around 15 °C. (Detailed information on DSC analysis are reported in Appendix III.5). Moreover, there were no substantial differences between the endothermic peak of films, cast from either SA40 or SA50 latexes, dried at 23 °C and 60 °C, which means that the crystallinity remained constant independently of the drying temperature. Therefore, it is discarded that the crystallinity causes the reduced water uptake observed for the films dried at 60 °C.

Water vapor transmission rate was also measured for the films cast at the two temperatures and the results are listed in Table 6.4.

Table 6.4. *WVTR data for latex films cast from SA40 and SA50 and dried at different temperatures (23 and 60 °C).*

	gmm/m ² of H ₂ O by Day	
	23 °C	60 °C
MB	12	12
SA40	5	3
SA50	11	4

As it can be seen in the WVTR test, the increase of the drying temperature from 23°C to 60°C led to a reduction in the water vapour transmission rate of SA films. However, if we consider MB specimens, the permeation of water (g of H₂O mm/m² day) resulted higher than that of SA films, independently of the drying temperature, which is

different from what was seen in water uptake test, where water sorption of MB was lower than that of SA40 and SA50 films dried at 23°C.

To better explain these results, it is necessary to consider Equation 1. From the WVTR data it is clear that the presence PSA semicrystalline nanodomains reduced the water flux through films dried at 23 °C, if compared with MB, and hence the permeability (P) as they are directly correlated ($P_{SA}^{23\text{ }^{\circ}\text{C}} < P_{MB}^{23\text{ }^{\circ}\text{C}}$). On the other hand, water uptake test showed higher values for SA films (dried at 23°C), which might mean higher water solubility ($S_{SA}^{23\text{ }^{\circ}\text{C}} > S_{MB}^{23\text{ }^{\circ}\text{C}}$). According to these results and to Equation 2, it can be concluded that to have lower value of $P_{SA}^{23\text{ }^{\circ}\text{C}}$ with respect to MB films, the diffusivity coefficient of SA film should be low enough ($D_{SA}^{23\text{ }^{\circ}\text{C}} \ll D_{MB}^{23\text{ }^{\circ}\text{C}}$) to counteract the higher value of $S_{SA}^{23\text{ }^{\circ}\text{C}}$, which is consistent with the presence of impermeable crystalline nanodomains homogeneously distributed in the polymer matrix.

6.4 Corrosion protection of waterborne latexes containing nanocrystalline domains

In order to evaluate the anticorrosion performances, SA40 and SA50 latexes were applied on steel substrates and dried at 23°C with 60% of RH or 60°C with 30% of RH,

respectively. The resulting coatings are shown in Figure 6.5. On the one hand, when the latexes were dried at 23 °C with 60% of RH the substrate phosphatization occurred thanks to the interaction between the phosphate groups, belonging to SIP, and the hydroxyl groups on the steel surface⁴¹.

On the other hand, when films were dried at 60 °C with 30% of RH, substrate phosphatization was not as evident as in the sample dried at 23°C and just a feeble stain was noticed on the surface. However, scanning electron microscopy assisted with energy dispersive X-ray analysis (SEM-EDX) of the detached coating confirmed the substrate phosphatization. For the sake of brevity only SA40 films dried at different temperature (23 and 60 °C) are reported (Figure 6.6).

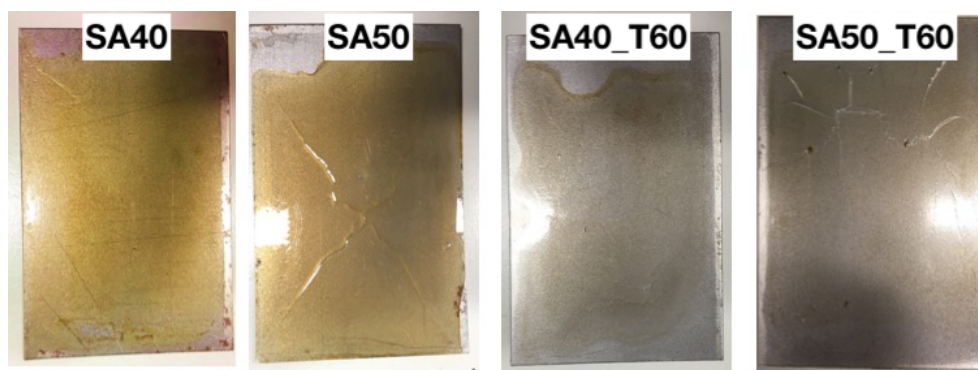


Figure 6.5. Steel substrate coated with SA40 and SA50 latexes dried at 23 °C with 60% RH (SA40 and SA50) and 60 °C with 30% RH (SA40_T60 and SA50_T60).

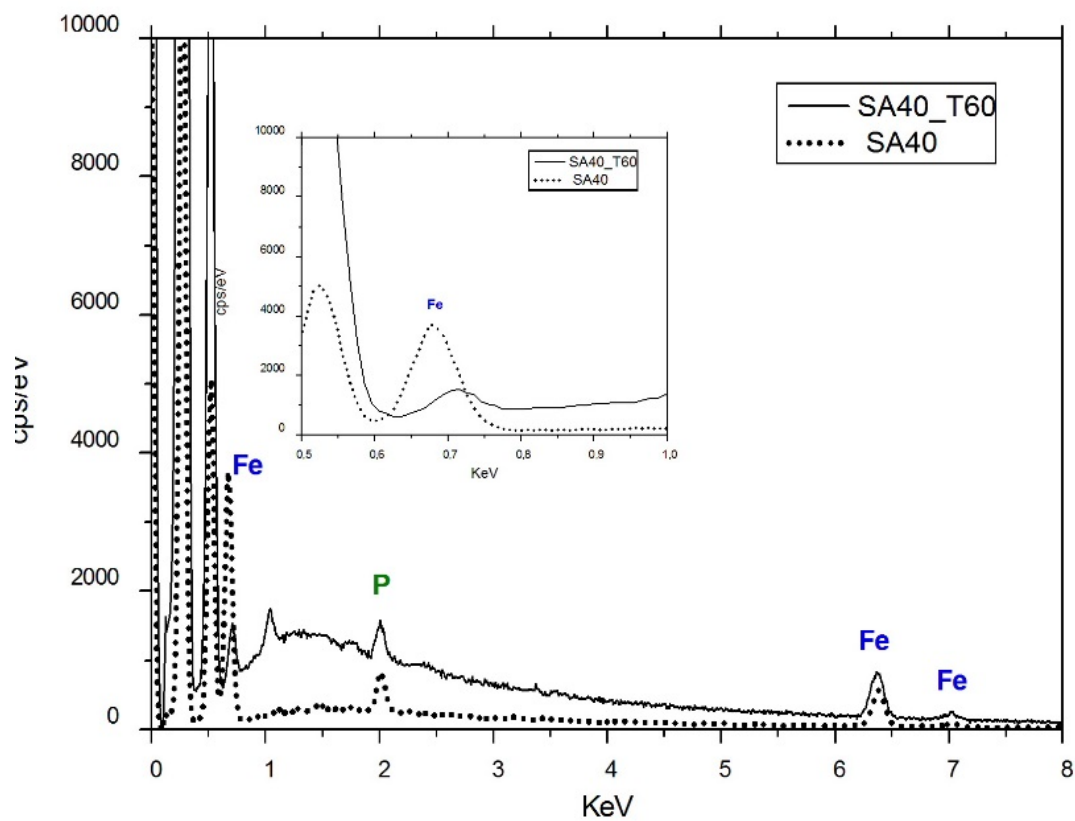


Figure 6.6. EDX spectrum of SA40 and SA40_T60 films detached from the steel substrates.

Figure 6.6 shows that, the characteristic peaks of iron, centered at 0.7, 6.2 and 7.0 KeV, were clearly visible in the detached films dried either at 23 °C (dotted line) or at 60 °C (line). This finding indicates that, independently from the drying conditions, the iron atoms get covalently bonded to the polymer (possibly as iron phosphate) and when

the coating is detached from the steel surface, the iron phosphates stay attached to the polymeric film. However, the intensity of the iron peak at 0.7 KeV is considerably lower when the latex is dried at 60 °C, which suggests that the formation of iron phosphate at the coating-substrate interface occurred, but at lower extent than after drying at 23 °C. As shown in Chapter 2, the faster the drying (achieved at higher temperature and/or lower relative humidity conditions) the lower the likelihood to produce the phosphatization layer.

Electrochemical impedance spectroscopy (EIS) was used to evaluate the corrosion protection of the synthesized latexes on the coated steel and the values of impedance modulus (IZI, collected after 500 h of immersion in 3.5 wt% NaCl solution) are summarized in Table 6.5.

At first glance, all the coatings showed good corrosion protection with impedance values higher than $10^9 \Omega \text{ cm}^2$ compared to that of bare steel at $10^3 \Omega \text{ cm}^2$ and similar to the reference (MB). Figure 6.7 reports the Bode plot of all the coatings tested. Considering the low frequency range, the impedance modulus was similar for all coatings and substantially higher than the uncoated substrate (more than 6 orders of magnitude higher than bare steel).

Table 6.5. *Anticorrosion properties after 500 hours of immersion in 3.5 wt% NaCl solution.*

Specimen tag	Drying Temperature (°C)	IZI ($\Omega \text{ cm}^2$)
SA40	23	$10^9 - 10^{10}$
SA40_T60	60	$10^9 - 10^{10}$
SA50	23	$10^9 - 10^{10}$
SA50_T60	60	$10^9 - 10^{10}$
MB	23	$10^9 - 10^{10}$
Bare steel	-	10^3

Independently from the drying temperature and from the presence of nanocrystalline domains, none of the coatings presented any noticeable difference in the whole frequency range of Bode plot; namely, at the mild conditions of exposure (500 h in a solution of 3.5 wt% of NaCl) the performance of all the coatings was very similar.

In order to mimic the harsh real corrosion conditions, accelerated neutral salt spray tests (NSS) were carried out. The results for steel specimens coated with these latexes after different exposition times are summarized in Table 6.6 and Figure 6.8.

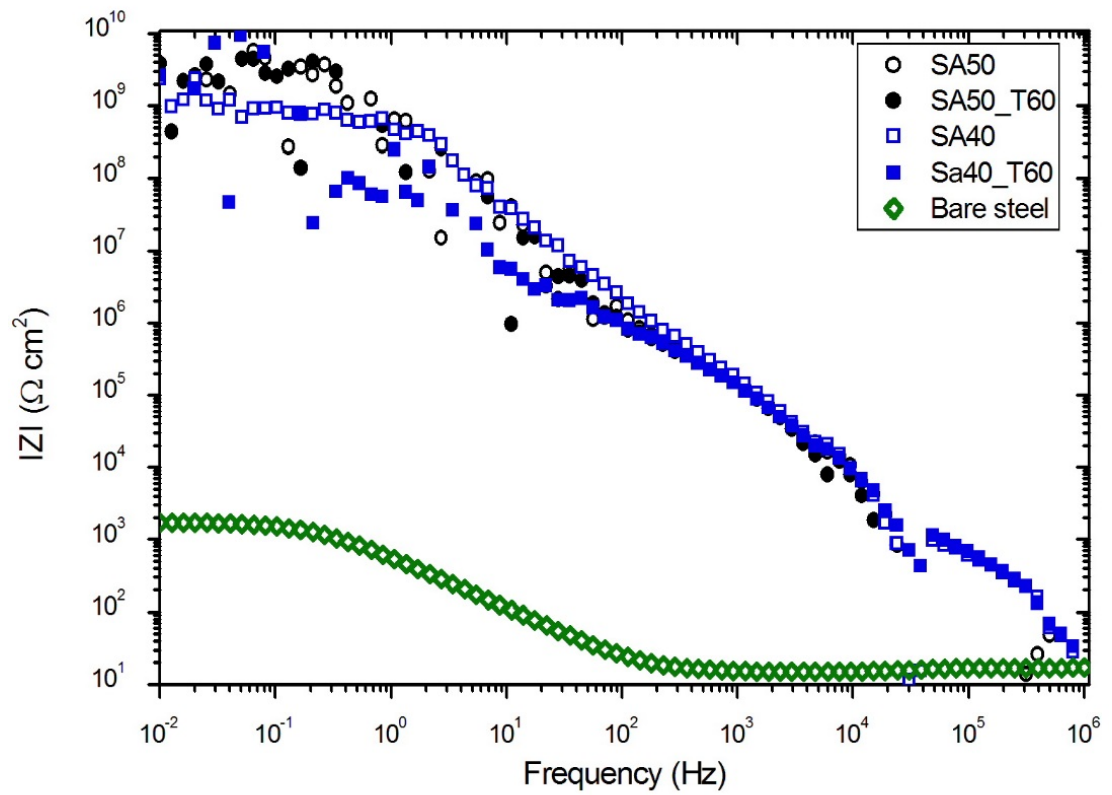


Figure 6.7. Bode plot of SA40 and SA50 dried at different temperatures (23 or 60 °C) after 500 h immersion in 3.5 wt% NaCl solution.

Table 6.6. Impedance modulus values at 10^{-2} Hz after 24, 200, 400, 600 hours in salt spray test.

Exposition Time (h)	Impedance modulus value				
	SA40*	SA40_T60**	SA50*	SA50_T60**	MB*
24	10^5-10^8	10^9-10^{10}	10^5	10^9-10^{10}	10^9-10^{10}
200	-	10^9-10^{10}	-	10^9-10^{10}	10^9-10^{10}
400	-	10^9-10^{10}	-	10^9-10^{10}	10^9-10^{10}
600	-	10^9-10^{10}	-	10^6-10^7	10^4
800	-	10^9-10^{10}	-	-	-
1000	-	10^5	-	-	-

* Film dried at 23 °C and 60 % of RH

** Film dried at 60 °C without RH control

As reported in Table 6.6, films containing nanocrystalline domains and dried at 60°C (SA40_T60 and SA50_T60) showed the same corrosion protection as the film cast from the reference latex (MB), while films dried at 23 °C suffered corrosion since the beginning of the salt spray test. In fact, after 24 hours of exposure to NSS, the impedance modulus of either SA40 and SA50 (at low frequency range) dropped to $10^5-10^8 \Omega \text{ cm}^2$ and to 10^5 , respectively, while it remained at values of $10^9-10^{10} \Omega \text{ cm}^2$ in the case of SA40_T60 and SA50_T60. The lower corrosion resistance of SA films dried at ambient temperature is consistent with the higher water sensitivity previously reported in Figure 6.3.

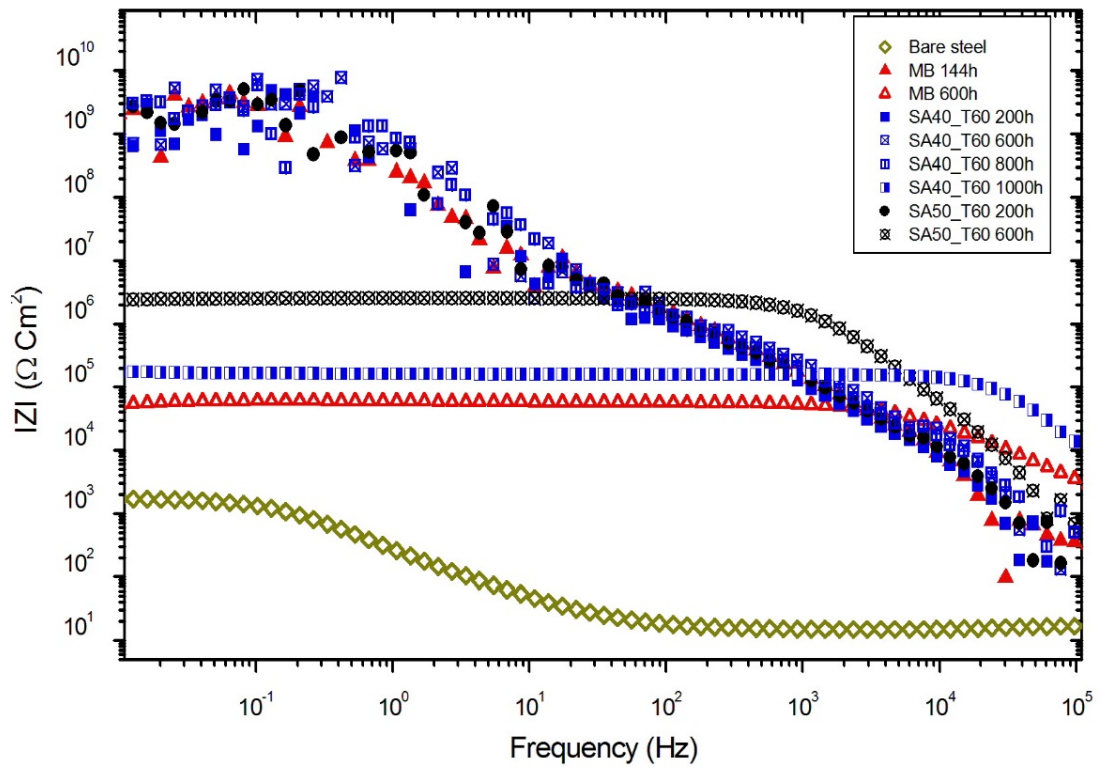


Figure 6.8. Bode plots of SA films and MB after salt spray test.

The barrier protection of SA films dried at 60 °C remained intact after 400 h of exposure, and the influence of nanocrystalline domains showed up after 600 h. In fact, while the specimen coated with MB suffered corrosion and the impedance critically dropped to $10^4 \Omega \text{ cm}^2$, the impedance modulus of SA40_T60 (at low frequency range)

remained at 10^9 - 10^{10} Ω cm² until 800 h of exposure and it dropped to 10^5 Ω cm² only after 1000 h.

Specimen coated with SA50_T60 started to corrode at 600 h as reported in Figure 6.8 by a drop of IZI to 10^6 - 10^7 Ω cm². This result reflects somehow what had been seen previously in WVTR analysis where the SA50 presented a higher WVTR than SA40. This finding indicates that the 40 % of SA comonomer in the polymer composition represents the optimal concentration of nanocrystalline domains per volume of polymer, while higher amount of crystalline PSA impair the barrier properties. However, it is worth to point out that the drop of drop of IZI was not as critical as in the case of MB (10^6 - 10^7 Ω cm² instead of 10^4 Ω cm²), which means that the coating was still providing some protection to the metal substrate.

6.5 Conclusions

Film forming latexes with core-shell morphology having semicrystalline polymer in the core and amorphous polymer surrounded by phosphate functionalities on the particles surface (SA40 and SA50) were synthesized by seeded semibatch emulsion polymerization. The seed was synthesized by miniemulsion polymerization using SA monomer. During the semibatch stage MMA/BA monomers were incorporated in a preemulsion stream that contains a phosphated polymerizable surfactants (Sipomer

PAM200). The presence of semicrystalline nanodomains in the polymer matrix enhances the barrier properties of the films when they were dried at 60 °C (as compared to the fully amorphous film (MB)). Moreover, by means of SEM-EDX analysis, the formation of the phosphatization layer at the coating-substrate interface was confirmed even after drying at 60 °C.

The synergic effect of enhanced barrier properties and substrate phosphatization play a key role on the anticorrosion protection and it was seen that 40% of stearyl acrylate in the polymer composition represents the critical amount of SA comonomer in the formulation, above which the enhancement in corrosion protection is not that significant. It was found that in harsh exposure conditions (exposition to 5 wt% NaCl aqueous salt spray) the SA40_T60 coating was able to present excellent corrosion protection after 800 h of exposure, which is double the time that the fully amorphous coating was able to tolerate (400 h) in the salt spray chamber.

6.6 References

1. Van der Wel, G. K.; Adan, O. C. G., Moisture in organic coatings — a review. *Progress in Organic Coatings* **1999**, 37 (1), 1-14.

2. Diaconu, G.; Paulis, M.; Leiza, J. R., High Solids Content Waterborne Acrylic/Montmorillonite Nanocomposites by Miniemulsion Polymerization. *Macolecular Reaction Engineering*, **2008**, 2 (1), 80-89.
3. Diaconu, G.; Paulis, M.; Leiza, J. R., Towards the synthesis of high solids content waterborne poly(methyl methacrylate-co-butyl acrylate)/montmorillonite nanocomposites. *Polymer* **2008**, 49 (10), 2444-2454.
4. Tan, B.; Thomas, N. L., A review of the water barrier properties of polymer/clay and polymer/graphene nanocomposites. *Journal of Membrane Science* **2016**, 514, 595-612.
5. Bhattacharya, M., Polymer Nanocomposites-A Comparison between Carbon Nanotubes, Graphene, and Clay as Nanofillers. *Materials* **2016**, 9 (4), 262-297.
6. Choudalakis, G.; Gotsis, A. D., Permeability of polymer/clay nanocomposites: A review. *European Polymer Journal* **2009**, 45 (4), 967-984.
7. Wolf, C.; Angellier-Coussy, H.; Gontard, N.; Doghieri, F.; Guillard, V., How the shape of fillers affects the barrier properties of polymer/non-porous particles nanocomposites: A review. *Journal of Membrane Science* **2018**, 556, 393-418.

8. Pavlidou, S.; Papaspyrides, C. D., A review on polymer-layered silicate nanocomposites. *Progress in Polymer Science* **2008**, *33* (12), 1119-1198.
9. Chimenti, S.; Vega, J. M.; Aguirre, M.; García-Lecina, E.; Díez, J. A.; Grande, H.-J.; Paulis, M.; Leiza, J. R., Effective incorporation of ZnO nanoparticles by miniemulsion polymerization in waterborne binders for steel corrosion protection. *Journal of Coatings Technology and Research* **2017**, *14* (4), 829-839.
10. Faucheu, J.; Gauthier, C.; Chazeau, L.; Cavaille, J.-Y.; Mellon, V.; Lami, E. B., Miniemulsion polymerization for synthesis of structured clay/polymer nanocomposites: short review and recent advances. *Polymer* **2010**, *51* (1), 6-17.
11. Diaconu, G.; Paulis, M.; Leiza, J. R., High solids content waterborne acrylic/montmorillonite nanocomposites by miniemulsion polymerization. *Macromolecular Reaction Engineering* **2008**, *2* (1), 80-89.
12. Diaconu, G.; Asua, J. M.; Paulis, M.; Leiza, J. R. In *High-Solids Content Waterborne Polymer-Clay Nanocomposites*, Macromolecular symposia, Wiley Online Library: 2007; pp 305-317.

13. Mittal, V., Polymer Nanocomposites in Emulsion and Suspension: an Overview. In *Polymer Nanocomposites by Emulsion and Suspension Polymerization*, Royal Society of Chemistry: 2010; pp 1-31.
14. Loiko, O. P.; Spoelstra, A. B.; van Herk, A. M.; Meuldijk, J.; Heuts, J. P. J. P. C., An ATRP-based approach towards water-borne anisotropic polymer–Gibbsite nanocomposites. *Polymer Chemistry* **2016**, 7 (20), 3383-3391.
15. Samakande, A.; Sanderson, R. D.; Hartmann, P. C., Encapsulated clay particles in polystyrene by RAFT mediated miniemulsion polymerization. *Polymer Science part. A* , **2008**, 46 (21), 7114-7126.
16. Bourgeat-Lami, E.; Lansalot, M., Organic/inorganic composite latexes: the marriage of emulsion polymerization and inorganic chemistry. In *Hybrid latex particles*, Springer: 2010; pp 53-123.
17. Donkers, P.; Huinink, H.; Erich, S.; Reuvers, N.; Adan, O., Water permeability of pigmented waterborne coatings. *Progress in Organic Coatings* **2013**, 76 (1), 60-69.
18. Okhamafe, A. O.; York, P., Effect of solids-polymer interactions on the properties of some aqueous-based tablet film coating formulations. I. Moisture permeability. *International Journal of Pharmaceutics* **1984**, 22 (2-3), 265-272.

19. Lin, J.; Shenogin, S.; Nazarenko, S., Oxygen solubility and specific volume of rigid amorphous fraction in semicrystalline poly (ethylene terephthalate). *Polymer* **2002**, *43* (17), 4733-4743.
20. Hedenqvist, M.; Gedde, U., Diffusion of small-molecule penetrants in semicrystalline polymers. *Progress in Polymer Science* **1996**, *21* (2), 299-333.
21. Weinkauff, D. H.; Paul, D. R., Effects of Structural Order on Barrier Properties. In *Barrier Polymers and Structures*, American Chemical Society: 1990; Vol. 423, pp 60-91.
22. Mehravar, E.; Leiza, J. R.; Asua, J. M., Performance of latexes containing nano-sized crystalline domains formed by comb-like polymers. *Polymer* **2016**, *96*, 121-129.
23. Mehravar, E.; Leiza, J. R.; Asua, J. M., Synthesis and characterization of comb-like acrylic-based polymer latexes containing nano-sized crystallizable domains. *Polymer* **2016**, *84*, 167-177.
24. Mehravar, E.; Iturrospe, A.; Arbe, A.; Asua, J. M.; Leiza, J. R., Phase behavior of side-chain liquid-crystalline polymers containing biphenyl mesogens with different spacer lengths synthesized via miniemulsion polymerization. *Polymer Chemistry* **2016**, *7* (29), 4736-4750.

25. Asua, J. M., Challenges for industrialization of miniemulsion polymerization. *Progress in Polymer Science* **2014**, 39 (10), 1797-1826.
26. Asua, J. M., Miniemulsion polymerization. *Progress in Polymer Science* **2002**, 27 (7), 1283-1346.
27. Barrer, R. M.; Rideal, E. K., Permeation, diffusion and solution of gases in organic polymers. *Transactions of the Faraday Society* **1939**, 35 (0), 628-643.
28. Jiang, B.; Tsavalas, J. G.; Sundberg, D. C., Water whitening of polymer films: Mechanistic studies and comparisons between water and solvent borne films. *Progress in Organic Coatings* **2017**, 105, 56-66.
29. Ashley, R. J., Permeability and Plastics Packaging. In *Polymer Permeability*, Comyn, J., Ed. Springer Netherlands: Dordrecht, 1985; pp 269-308.
30. Liu, Y.; Soer, W.-J.; Scheerder, J.; Satgurunathan, G.; Keddie, J. L., Water Vapor Sorption and Diffusion in Secondary Dispersion Barrier Coatings: A Critical Comparison with Emulsion Polymers. *ACS Applied Materials & Interfaces* **2015**, 7 (22), 12147-12157.

31. Liu, Y.; Soer, W.-J.; Scheerder, J. r.; Satgurunathan, G.; Keddie, J. L., Water vapor sorption and diffusion in secondary dispersion barrier coatings: A critical comparison with emulsion polymers. *ACS applied materials & interfaces* **2015**, *7* (22), 12147-12157.
32. Masaro, L.; Zhu, X. X., Physical models of diffusion for polymer solutions, gels and solids. *Progress in Polymer Science* **1999**, *24* (5), 731-775.
33. Van Krevelen, D. W.; Te Nijenhuis, K., Chapter 18 - Properties Determining Mass Transfer In Polymeric Systems. In *Properties of Polymers (Fourth Edition)*, Elsevier: Amsterdam, 2009; pp 655-702.
34. Thomas, N. L., The barrier properties of paint coatings. *Progress in Organic Coatings* **1991**, *19* (2), 101-121.
35. Blahník, R., Problems of measuring water sorption in organic coatings and films, and calculations of complicated instances of moistening. *Progress in Organic Coatings* **1983**, *11* (4), 353-392.
36. Hare, C., Water permeability in pigmented films. *Journal of Protective Coatings & Linings* **1997**, *14* (10).
37. Vieth, W. R., *Diffusion in and through polymers : principles and applications*. München : Hanser Verlag: 1991.

38. Deflorian, F.; Fedrizzi, L.; Rossi, S.; Bonora, P. L., Organic coating capacitance measurement by EIS: ideal and actual trends. *Electrochimica Acta* **1999**, *44* (24), 4243-4249.
39. van Westing, E. P. M.; Ferrari, G. M.; de Wit, J. H. W., The determination of coating performance with impedance measurements—II. Water uptake of coatings. *Corrosion Science* **1994**, *36* (6), 957-977.
40. Feng, J.; Winnik, M. A., Effect of Water on Polymer Diffusion in Latex Films. *Macromolecules* **1997**, *30* (15), 4324-4331.
41. Chimenti, S.; Vega, J. M.; García-Lecina, E.; Paulis, M.; Leiza, J. R., In-situ phosphatization and enhanced corrosion properties of films made of phosphate functionalized nanoparticles. *Submitted to Reactive and Functional Polymers*, **2019**.

Chapter 7

Performance of phosphated waterborne binders in Direct to Metal (DTM) Paints

7.1	Introduction.....	203
7.2	Synthesis of waterborne binders for DTM paint.....	205
7.3	DTM paint preparation	207
7.4	Performance of DTM paints	208
7.4.1	Adhesion resistance	210
7.4.2	Flash rust resistance	213
7.4.3	High Humidity resistance.....	213
7.4.4	Weathering cyclic test.....	222
7.4.5	Salt spray test.....	224
7.5	Conclusions.....	225
7.6	References.....	226

7.1 Introduction

In a waterborne paint formulation, the polymer latex accounts for about 50% of the total weight whereas the remaining part is made of inorganic pigments and other agents such as defoamers, dispersants, thickeners, wetting and coalescing agents and anticorrosion inhibitors. Typically, the inorganic pigments have several roles such as providing colour (colour pigments such as white (TiO_2 , ZnO^1), red (Fe_2O_3^2) or blue ($\text{CoAl}_2\text{O}_4^{2-4}$)), reducing the cost (extender pigments, such as coarse CaCO_3 , which reduces cost by filling coating volume with minimal impact on performance) and also providing anticorrosion protection ($\text{Zn}_3(\text{PO}_4)_2$, $\text{Ce}(\text{NO}_3)_3$ and $\text{La}(\text{NO}_3)_3^5$).

In the previous chapters, the performance of neat latexes was assessed. Even though the binder is the key component in the paint formulation, the addition of the additives may affect the final properties of the paint. Therefore, it is essential to evaluate the performance of the binder as part of the paint formulation as well as the compatibility between all the paint components.

Formulating a good paint coating is not straightforward. Typically, it requires an extensive analysis of the effect of the multiple ingredients of the formulation on the final properties of the paints and this is out of the scope of this work. The objective of the present Chapter is to make a preliminary and brief evaluation of the performance of some of the more promising latexes synthesized in this work, in a standard direct to

metal paint formulation (DMT). DTM paint is a type of coating which is applied directly onto a metal substrate without the use of a conversion coating beforehand. Usually, DMT coatings have an acrylic composition that allows them to successfully adhere to a metal surface when directly applied.

In the present case, the substrate adhesion as well as the anticorrosion protection of three binders-based paint systems have been tested and then compared with a commercially available DMT paint. The binders selected have been:

- MB (MMA/BA=50/50) synthesized by seeded semibatch emulsion polymerization with 2 wmb% of SipomerPAM200 phosphated surfmer (Chapter 2);
- SA40 (SA/MMA/BA=40/30/30) and SA50 (SA/MMA/BA=50/25/25) synthesized by seeded semibatch emulsion polymerization (the seed prepared by miniemulsion polymerization) with 2 wmb% of SipomerPAM200 phosphated surfmer (Chapter 6).

This work was carried out during the internship in the R&D department of VINA VIL SPA (Italy).

7.2 Synthesis of waterborne binders for DTM paint

MB, SA40 and SA50 waterborne binders, were synthesized again in Vinavil in a 3 litres scale, according to the synthetic procedure of Chapter 2 and Chapter 6, respectively. However, additionally to the previous procedure, a REDOX initiator couple was fed at the end of the reaction in order to reduce the concentration of the unreacted monomer below 100 ppm (in compliance with the specification of VINAVIL SPA QA department). Namely, 5 wt% Bruggolite (FF6) solution and 5wt% tertbutyl hydroperoxide (TBHP) solution were fed separately at 0.733 g/min for 30 minutes. The resulting latexes showed final particle size similar to the analogous latexes synthesized in Chapter 2 and in Chapter 6, i.e. 189 nm for MB and, 181 nm and 179 nm for SA40 and SA40, respectively.

Before formulating the DTM paint, the mechanical stability of the selected binders was tested. Mechanical stability test is a rapid, simple method of estimating the colloidal stability of the latex by high-speed stirring⁶. Namely, the latex is loaded in the stability tester and stirred at 10000 ± 200 rpm by means of an impeller. During the test, foaming and progressive flocculation are monitored visually. After 10 minutes of stirring, the amount of coagulum (in ppm) is quantified by filtering the latex with a 325 mesh (44 μ m) steel filters and it is compared with the values of coagulum before the

mechanical test. Increases of coagulum below 100 ppm are acceptable and the latex is considered valid for the subsequent formulation step. The evaluation of mechanical stability after high-speed stirring is important because it represents the latexes processability in the industrial scale. Suffice is to say that a latex has to be formulated after its production, which means high-speed mixing with other paint's components and hence it has to be stable under high shear rate conditions.

As it can be seen in Table 7.1, when the latex pH was increased from 7 to 8 through the addition of ammonia solution, the amount of filtered coagulum at 325 mesh was substantially reduced and it remained under the permitted limit of 100 ppm. The addition of a base increases the double electric layer of the particles and hence their colloidal stability⁷. Therefore, the pH of all the formulated waterborne latexes was corrected to 8.

Table 7.1. *Mechanical stability test of MB, SA40 and SA50 latexes.*

Sample	pH	ppm**
MB	7	333
	8*	30
SA40	7	219
	8*	48
SA50	7	290
	8*	86

* pH correction made by addition of NH₄OH solution

** ppm of coagulum after filtration with 325 mesh filter

7.3 DTM paint preparation

In this chapter the anticorrosion performance of paints based on MB, SA40 and SA50 were compared with a commercial binder (SPA). The waterborne paints were prepared by using a standard formulation for DTM paints in a one step process (the formulation is listed in Table 7.2). Detailed information about the additives used in DTM paints is shown in Appendix III.6.

First of all, the water, defoamer (TEGO AIREX 902 W, Evonik), dispersant (DISPERBYK 191, Byk) and a low amount of the binder (5.9 wt% with respect of the total paint weight) were premixed at 900 rpm using a high-speed disperser blade (DISPERMAT CN10). The pigment (TiO₂ Type R706, Chemours) was then slowly added and stirred at 2000 rpm. After 10 minutes the stirring rate was reduced to 900 rpm and the filler (Talc CHB2), coalescing agent (butyl carbitol) and the binder were incorporated in the systems. At the end, defoamer (Foamex 1488, Evonik), biocide (Acticide MBS, Thor), alkalizing agent (AMP 95, Angus), wetting agent (Byk 3455) and a thickener (Tafigel PUR44, Muzing) were added and the paint was let under stirring at 900 rpm for 10 minutes. The resulting paints were labelled P_MB, P_SA40, P_SA50 and SPA1.

For comparison purpose, the commercial binder was also formulated with the addition of corrosion inhibitors; namely zinc oxide, zinc phosphate (Z-plex 111, Halox) and Naziln FA179 (Elementis) were incorporated in the paint labelled SPA0.

7.4 Performance of DTM paints

It has been already explained in Chapter 1 that the basic features in order to design an efficient waterborne latex for anticorrosion protection are adhesion, barrier protection and flash rust resistance; for this reason, in the present section, the assessment of these properties are presented.

Namely, adhesion resistance, flash rust resistance, high humidity and weathering tests were performed for all the paints formulations.

Two substrate cleaning procedure were considered in this chapter:

- *Acetone cleaning* (Labeled A) in which any wax contamination of the steel substrates was removed simply by means of acetone rinsing.
- *Uniclean cleaning* (Labeled U) in which the substrate was cleaned by means of the procedure described in Appendix II.6, i.e. with HCl and UNICLEAN 251A

Table 7.2. Waterborne paint formulations with corrosion inhibitors (SPA0) and without corrosion inhibitors (P_MB, P_SA40, P_SA50, SPA1).

Ingredients	Name	P_MB, P_SA40, P_SA50, SPA1		SPA0	
		Wt%	Amount (g)	Wt%	Amount (g)
Water		28.2	84.6	20.4	61.2
Defoamer	Tego airex 902W	0.2	0.6	0.2	0.6
Dispersant	Disperbyk 191	0.6	1.8	0.6	1.8
Binder		5	15.0	5	15.0
Pigment	TiO ₂ type R706	15	45.0	15	45.0
Pigment	Zinc oxide	-	-	2.9	8.7
Inhibitor	Z-plex 111	-	-	3.6	10.8
Filler	Talc CHB2	5	15.0	5	15.0
Coalescing agent	Butyl carbitol	2	6.0	2	6.0
Binder		42	126.0	42	126.0
Defoamer	Foamex 1488	0.2	0.6	0.2	0.6
Biocide	Acticide MBS	0.1	0.3	0.1	0.3
Inhibitor	Naziln FA179	-	-	1.3	3.9
Alkalizing agent	AMP95	0.3	0.9	0.3	0.9
Wetting agent	Byk 3455	0.4	1.2	0.4	1.2
Thickener	Tafigel PUR44	1	3.0	1	3.0

7.4.1 Adhesion resistance

The most used test to evaluate the coating adhesion, so far, is the peel test. The test consists of observing whether the film is peeled off when a tape attached to it is removed. In detail, a cross-hatched pattern is cut into the coating, a tape (Tesa 4104) applied and removed, and the coating removal is assessed against the established rating scale described in the ASTM D3359 test method B ⁸ and showed in Figure 7.1.

Generally, the dry-thickness of the film applied according to the method B should be lower than 125 μm . In Table 7.3 and Figure 7.2 the adhesion test results for paints based on MB, SA40 and SA50 latexes dried at 23 and 60 $^{\circ}\text{C}$ (P_SA40 and P_SA50 dried at 23 $^{\circ}\text{C}$ and P_SA40_T60 and P_SA50_T60 dried at 60 $^{\circ}\text{C}$) and SPA (SPA0 and SPA1), applied onto steel substrate, cleaned with the previously mentioned procedures (A and U) are presented.

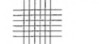


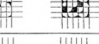


CLASSIFICATION OF ADHESION TEST RESULTS		
CLASSIFICATION	PERCENTAGE OF COHESIVE AREA FROM WHICH PEELING HAS OCCURRED FOR 5X PARALLEL CUTS AND ADHESION RATED BY FORCE*	DIAGRAMS
5B	0%	
4B	<5%	
3B	5-15%	
2B	15-35%	
1B	35-65%	
0B	>65%	

Figure 7.1. Classification of adhesion test results. From ASTM D3359.

Table 7.3. Adhesion test results of the formulated paints on steel.

Sample	P_MB	P_SA40	P_SA50	P_SA40_T60	P_SA50_T60	SPA0	SPA1
Adhesion	A	1B	4B	4B	4B	4B	2B
	U	1B	4B	4B	5B	5B	4B

At first glance it can be seen that P_MB paints showed the lowest adhesion properties in comparison with the other specimens tested. In fact, the coatings have flaked along the edges of the cut in large ribbons, and whole squares have detached. However, if we take a closer look at P_MB A and P_MB U specimens in Figure 7.2, the majority of the coating peeled off results to be at the boundaries of the cross cut while the central part resulted less damaged. This finding may suggest the presence of localized voids or defects that affect the interfacial bonding between coating and substrate and hence the fracture, generated during the tape peeling off, can propagate along the weakest point⁹.

Apart from P_MB coated specimens, all the remaining coatings showed good to excellent adhesion properties. Moreover, in the case of P_SA films, dried at 60 °C and applied on substrate cleaned with procedure U, none of the square of the cross-cut was detached after the peeling (Figure 7.2), which means that the higher drying temperature, according to what has been said in section 6.4 of chapter 6, reduces the concentration of voids and defects and hence the fracture formation and propagation after the tape peeling. Since the only difference between P_MB with P_SA paints is the presence of

semicrystalline nanodomains in the latter; it can be concluded that these crystalline domains provide cohesion to strengthen the amorphous phase.

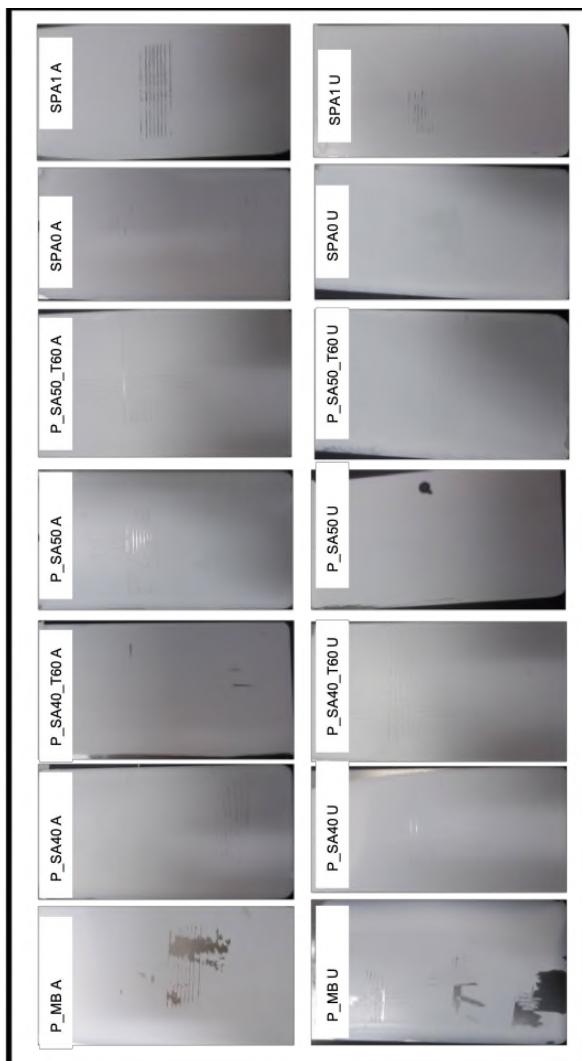


Figure 7.2. Results of adhesion test of the formulated paints onto steel substrates.

7.4.2 Flash rust resistance

As already mentioned in Chapter 2, the flash rust is a phenomenon that occurs when drying a waterborne film on a ferrous substrate. It is generally indicated by the presence of rust spots on the paint film, or sometimes by a tarnishing of larger areas. In fact, flash rust inhibitor additives are usually included in waterborne paints to prevent it. However, we wanted to check the flash rust resistance of our paints without the addition of any of these inhibitors.

A typical procedure to test is to cast a wet film (sufficient to yield a 150-200 μm dry film) on a steel substrate and immediately place the panel in the humidity chamber at 35 °C and 90 % of RH; then let it dry under this condition for 5 h, and evaluate for any rust spots. MB and SA based coatings showed resistance against flash rust as in none of them (considering both cleaning procedures) neither rust spots nor tarnish were detected on the surfaces. For the sake of brevity, and due to the positive response of all the specimens, the pictures after the test are not reported here.

7.4.3 High Humidity resistance

According to the ISO 6270-2:2005¹⁰, the test consists in evaluating the water resistance, and hence corrosion, of coated specimens in an atmosphere maintained at 99 % RH and 40 °C, so that condensation forms on the specimens. In detail, steel panels

were coated with the different paints, then scribed with a knife (6 cm long scribe) and maintained at the testing condition for 250 h. At the end of the test, the presence of rust formation, blistering, loss of adhesion or embrittlement were evaluated.

The beneficial effect of using waterborne latexes containing phosphate functionalities showed up in the High Humidity resistance test. In fact, as it can be seen in Figure 7.3, coatings cast from P_MB, P_SA40_T60 and P_SA50_T60 paints were able to protect the steel substrate without the addition of any anticorrosion inhibitors, whereas substrate protection by paints based on SPA was only achieved for the formulation containing inhibitors (SPA0).

Either SPA1 A and SPA1 U clearly presented signs of corrosion and, in both cases, the rust started to form in the whole specimen and not only in the scribe. In the case of films cast from P_SA paints and dried at 23 °C or at 60 °C (P_SA40 A, P_SA40 U, P_SA50 A and P_SA50 U), corrosion started from the incision and then propagated in the whole surface of the specimen. These results reflect what has been seen in Chapter 6, where drying of the SA based films at 23 °C or 60 °C affected the final barrier properties. Another important feature provided by phosphate containing waterborne latexes resulted in the ability to avoid delamination of the coating as a result of the formation of corrosion products.

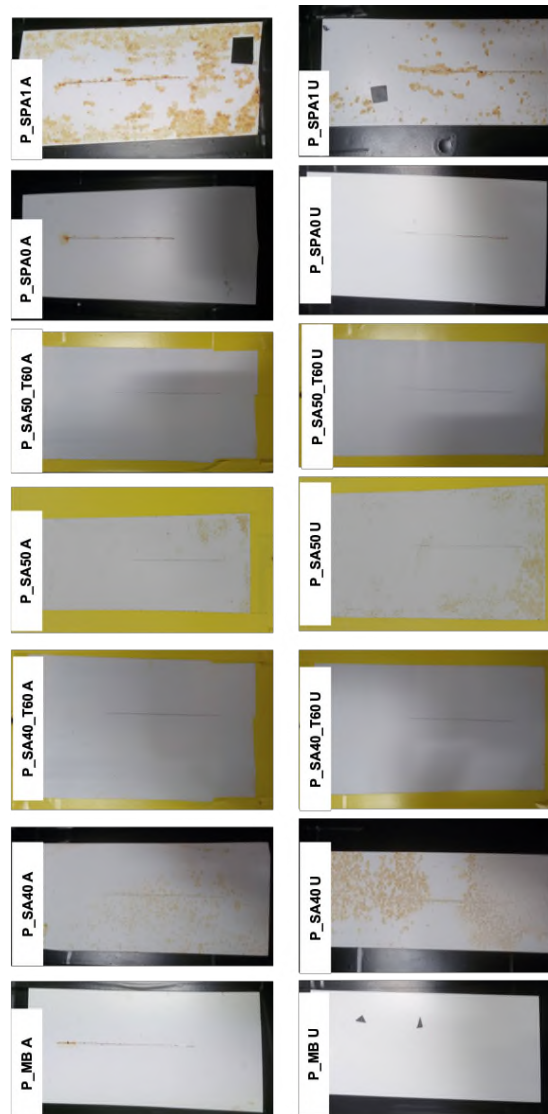


Figure 7.3. Results of high humidity test for scribed specimens coated with the formulated paints on steel cleaned with the different cleaning procedures (A and U) after 250 h of exposure to RH=99% and T=40 °C.

In fact, even if P_MB, P_SA40_T60 and P_SA50_T60 presented some corrosion spot localized at the incision (where the steel surface is directly in contact with oxygen and moisture), the corrosion did not propagate to the near coating-substrate interface, which means that the iron phosphate layer remained tightly attached to both the coating and the steel surface. For comparison purpose, the cross-section of P_MB U, P_SA40_T60 U and P_SPA1 U specimens has been investigated by Scanning Electron Microscopy assisted with energy dispersive X-ray spectroscopy (SEM-EDX). Namely, as it shown in scheme in Figure 7.4, the scribe and a non-scribed region of the cross section have been analyzed.

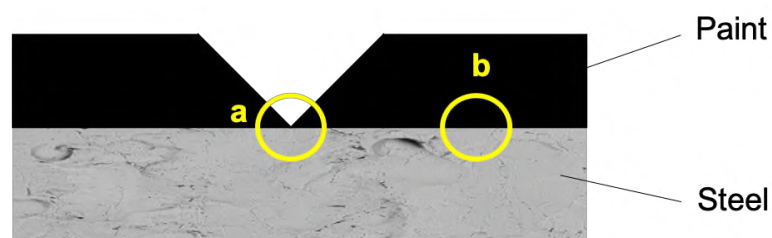


Figure 7.4. Scheme of the cross section of the coated specimens. Note: SEM-EDX analysis was carried out at (a) the scribe and at (b) no-scribed region.

Figure 7.5 b and 7.6 b show the cross-sectioned specimens (P_MB U and P_SA40_T60 U) at the non-scribed region with the tracks in which the EDX linescan analysis were performed marked by a yellow arrow. EDX line scan analysis were carried out because it is a powerful technique that allows to detect qualitatively the

presence of corrosion products, along the selected track, by monitoring the Iron and Oxygen counts profiles (counts is referred to the number of X-Ray photons emitted and hence the intensity of the emitted X-ray radiation¹¹). Figure 7.5d and 7.6d present the profiles of Iron (in blue) and of Oxygen (in red) recorded in the direction of the yellow arrow, from the steel to the paint at the non-scribed region of the cross-section (P_MB U and P_SA40_T60 U). The steel phase appears bright in the micrographs and with higher counts of Iron, with respect to the one of Oxygen, indicating the absence of iron oxides (in the case of the presence of iron oxides the Oxygen profiles should have presented some peaks with counts closer to the ones of Iron). Moreover, moving along the linescan track, from the steel to the coating layer, the drop in the Fe count profile indicates the absence of Iron in the latter and hence the absence of corrosion products.

On the other hand, as expected, some rust was found at the scribe (Figure 7.5a and 7.6 a) as confirmed in the EDX line scan profiles (Figure 7.5c and 7.6c). The presence of peaks (higher counts) in the profiles of either Oxygen (approximately at the linescan track length of 25 and 70 μm in Figure 7.5c and at 5-10 μm in Figure 7.6c) or Iron (approximately at the linescan track length of 50 μm in Figure 7.5c and 30 and 35 μm in Figure 7.6c) in the scribe indicates that some corrosion products developed during the corrosion test. However, it is noteworthy the fact that the corrosion did not propagate in the coating and remained confined in the scribe; in fact, in the nearby

region of the scribe the lower count of Oxygen profile with respect to the count profile of Iron indicates the absence of rust (Figure 7.5 and 7.6).

Figure 7.7a shows the micrograph of SPA1 U at the scribe but, in this case, the scribe was not well defined as in the case of P_MB U and P_SA40_T60 U (Figure 7.5a and Figure 7.6a, respectively). The EDX analysis of the scribe (Figure 7.7c) revealed the presence of several peaks in both the Oxygen and Iron count profiles, which indicated that, during the corrosion test the formation of iron oxides occurred in larger extent filling the scribe. Moreover, it seems that the corrosion propagates to the nearby region as confirmed in the EDX linescan analysis (Figure 7.7c, peaks in both the Oxygen and Iron count profiles are present). Additional proof of the poor protection of SPA1 U is given by the micrograph of the cross section taken in the non-scribed region and its EDX analysis (Figure 7.7 b and 7.7d). The presence of corrosion products in the steel phase (grains-shape iron oxides that appears darker than the steel phase in Figure 7.7b) beneath the paint layer indicated that, despite the integrity of the coating system (no scribe in the analyzed region), the water molecules were able to diffuse to the underlying metal surface and to trigger the corrosion that propagate in both the steel and the coating phase. The presence of several peaks in the count profile (EDX line scan in Figure 7.7d) of both Oxygen and Iron in either the steel phase or in the coating

phase agreed with the previous observation and confirm the propagation of the corrosion.

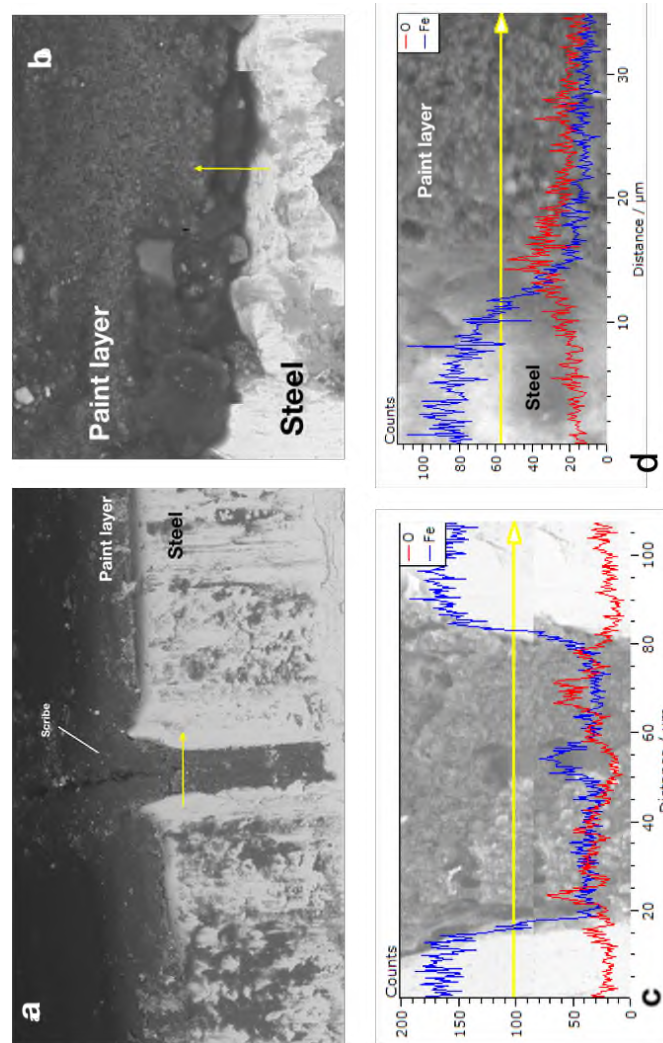


Figure 7.5. SEM micrographs with EDX linescan (c and d) of the cross-section of *P_MB U* coated specimens at (a) the scribe and at (b) no-scribed region.

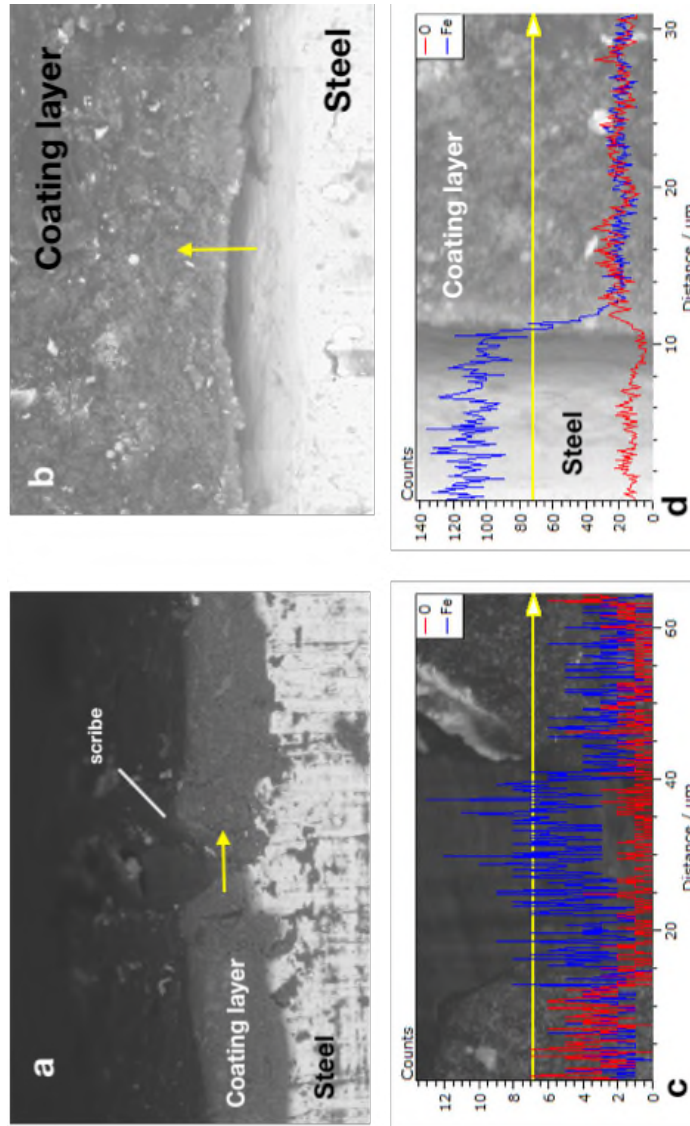


Figure 7.6. SEM micrographs with EDX linescan (c d) of the cross-section of *P_SA40_T60 U* coated specimens at (a) the scribe and at (b) no-scribed region.

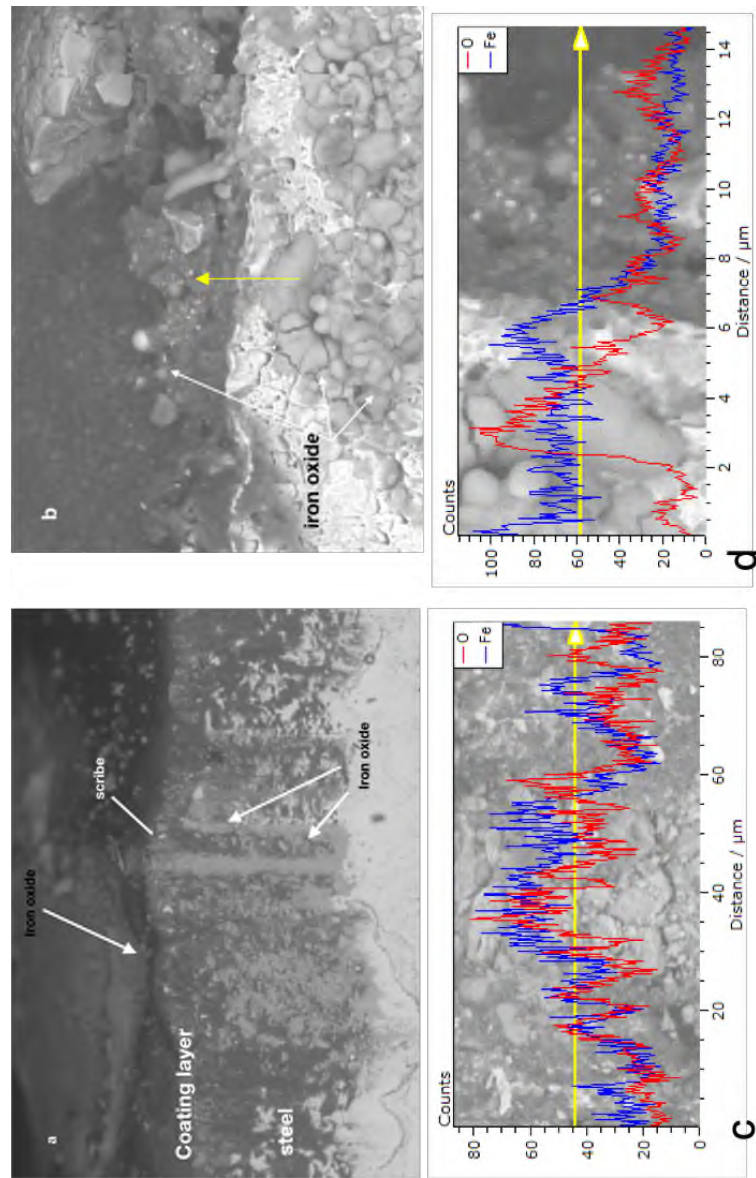


Figure 7.7. SEM micrographs with EDX linescan (c and d) of the cross-section of SPAI P coated specimens at (a) the scribe and at (b) no-scribed region.

7.4.4 Weathering cyclic test

The test described above is referred to constant climate conditions. However, it can be combined with repetitive cyclic variations in temperature, humidity or even radiation. For instance, irradiation with UV is primarily used to assess the photochemical resistance of the binder system, however it may also give a good account on the overall resistance of the entire coating against weather, when combined with humidity¹². This test substantially attempts, more closely than the high humidity test, to simulate the outdoor conditions (non-marine) in a laboratory environment (closely controlling levels of humidity, UV level and temperature) and it is recommended for paint coatings being used in typical (non-marine) atmospheric conditions exposure. In detail, scribed panels were exposed to 200 hours periods of high humidity (as described in section 7.4.3) followed by 200 hours periods of light/condensation exposure (4 h UV light exposure to a Xenon lamp, which simulate the short-wave solar radiation at 340 nm at 60 °C, alternating with 4 h condensation at 50 °C) for a total of 2000 hours. For the weathering component of this test, a standard ultraviolet light condensation cabinet, according to the ASTM G53 standard¹³, was employed. As it can be seen in Figure 7.8, MB and SA40_T60 and SA50_T60 based paints (substrate cleaned with procedure A or U) performed similarly to the commercial DTM paint SPA0 (with corrosion inhibitors in the formulation), but without the

addition of any anticorrosion inhibitors. Notably, the performance of our binders-based paints was similar to the commercial one, which indicates that they were able to provide at least the same protection coverage under cyclic and prolonged corrosion conditions similar to the outdoor exposure.

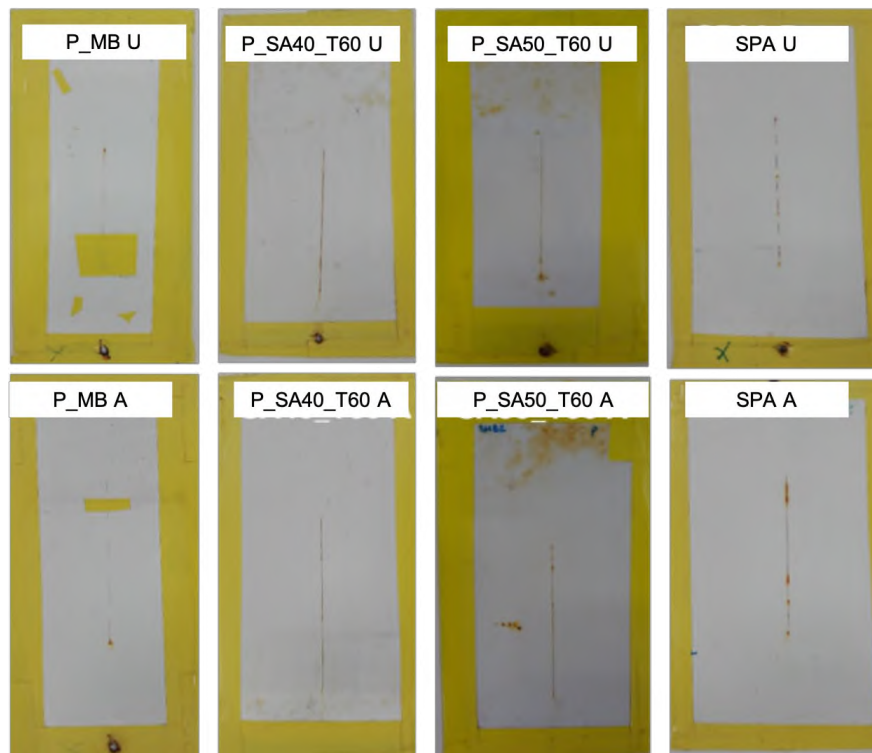


Figure 7.8. Results of cyclic high humidity-weathering test for scribed specimens coated with the formulated paints on steel cleaned with the different cleaning procedure (A and U) after 2000 hours of exposure. Note: P_SA40 and P_SA50 coated specimen and dried at ambient temperature have not been tested due to the degradation of those after the first cycle of exposition at high humidity.

7.4.5 Salt spray test

Accelerated corrosion test, i.e. salt spray test, was also carried out and Figure 7.9 shows the result of coated steel panels after 240 h of exposure to the 5 wt% NaCl fog. Since the cleaning procedure of the steel surface did not show particular difference in the previous paint tests, just the procedure A was carried out.

At first glance, the P_MB coat showed good corrosion protection if compared with the commercial one (SPA0). As it can be noticed, the corrosion occurred at the scribe, but did not propagate whereas in SPA0 signs of corrosion appeared in the whole coating surface area. This result provides further evidences of the anticorrosion protection without the addition of anticorrosion inhibitors provided by MB based paint.

On the contrary, P_SA coats dried at 60 °C showed poor performance in salt spray as coated specimens underwent severe corrosion after 240 h of exposure. This result was not expected especially because the binders presented a better performance (+800 hours in salt spray test, compared to 400 h for MB binder). Admittedly, we do not have an explanation for this inconsistency in the salt-spray test of the binders and the paints formulated from these. However, it is worth to recall, as discussed in section 7.1, that formulating a paint is a complex and sophisticated technique that relies in trial-and-error. Furthermore, it is known that small changes in the binder composition might require substantial adjustment in the formulation of the optimal paint. However

optimization of the paint formulation for each binder was out of the scope of this work.

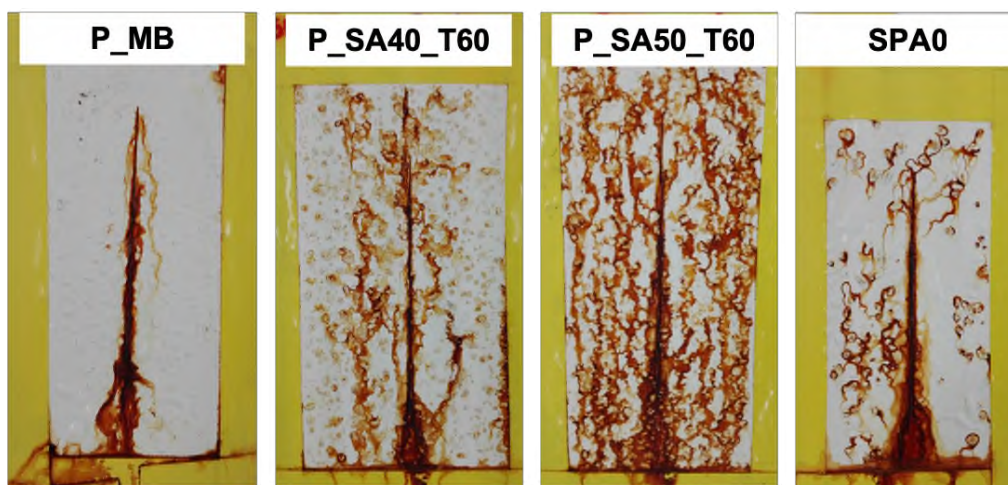


Figure 7.9 Results of salt spray test for scribed specimens coated with the formulated paints after 240 hours of exposure to 5 wt% NaCl salty fog.

7.5 Conclusions

The incorporation of phosphated waterborne latexes (MB, SA40 and SA50) into commercial paint formulations for direct to metal (DTM) application was addressed in this chapter and compared with a commercially available DTM paint. The presence of phosphate functionalities, that showed in the previous chapter the ability to enhance the anticorrosion properties of waterborne binders, allow to design and formulate paints that provide anticorrosion properties comparable with the one provided by the

commercial system, but notably without the use of corrosion inhibitors. In fact, contrary to the commercial binder formulated without the corrosion inhibitors, P_MB, P_SA40_T60 and P_SA50_T60 coatings successfully protected the steel substrate at high humidity conditions, as well as in a weathering test of 2000 h (cyclic exposure to UV radiation and high humidity conditions). It is noteworthy to mention that in the case of SA based coating, drying the film at 60 °C was critical to provide corrosion protection, which is consistent with the results described in Chapter 6.

The outcome of the corrosion and weathering tests provided an important proof of the powerful outlook of these systems in the corrosion protection, especially because they could reduce the cost of the final coating systems avoiding the addition of corrosion inhibitors. On the other hand, despite the good corrosion protection provided in the salt spray test by P_MB coat, P_SA coats presented poor protection against more aggressive corrosive condition of the salt-spray, which indicates the necessity of an optimization of the formulation.

7.6 References

1. *Chapter 19- White Pigments, Paint and Coating Testing Manual, Philadelphia, PA.* 14th Edition ed.; American Society of Testing and Materials: **1995**; Vol. 20, p 270-270.

2. Chapter 22- *Inorganic Colored Pigments, Paint and Coating Testing Manual, Philadelphia, PA.* 14th Edition ed.; American Society of Testing and Materials: **1995**; Vol. 20, p 234-239.
3. McKeen, L. W., 5 - Pigments, Fillers, and Extenders. In *Fluorinated Coatings and Finishes Handbook*, William Andrew Publishing: Norwich, NY, **2006**; pp 59-76.
4. Chapter 24- *Extender Pigments, Paint and Coating Testing Manual, Philadelphia, PA.* 14th Edition ed.; American Society of Testing and Materials: **1995**; Vol. 20, p 242-249.
5. Chapter 28- *Protective Coatings and Inorganic Anti-Corrosion Pigments, Paint and Coating Testing Manual, Philadelphia, PA.* 14th Edition ed.; American Society of Testing and Materials: **1995**; Vol. 20, p 282-299.
6. Dawson, H. G., Mechanical Stability Test for Hevea Latex. **1950**, *23* (4), 981-994.
7. Ishikawa, Y.; Katoh, Y.; Ohshima, H., Colloidal stability of aqueous polymeric dispersions: Effect of pH and salt concentration. *Colloids and Surfaces B: Biointerfaces* **2005**, *42* (1), 53-58.
8. Standard, A., D3359-09E2," Standard Test Methods for Measuring Adhesion by Tape Test," ASTM International, West Conshohocken, PA, **2009**

9. Paint and Coating Testing Manual, (Gradner-Sward Handbook, 14th Edition) edited by Dr. Joseph V. Koleske, American Society of Testing and Materials, Philadelphia, PA, *Color Research & Application* **1995**, 20 (4), 270-270.

10. ISO 6270-2:2005 - Determination of resistance to humidity — Part 2: Procedure for exposing test specimens in condensation-water atmospheres. In *Paints and varnishes*, **2005**.

11. Michler, G. H., *Electron microscopy of polymers*. Springer Science & Business Media: **2008**.

12. VDA 621-430 - Resistance to cracking- clear coat. In *Tests for Automotive Coatings*.

13. International, A., ASTM G53-96, Practice for Operating Light- and Water-Exposure Apparatus (Fluorescent UV-Condensation Type) for Exposure of Nonmetallic Materials. **2000**.

Chapter 8.

Conclusions

The design of thin and multifunctional waterborne latexes for anticorrosion application has been carried out in this thesis. Considering that, usually the corrosion protection in a conventional anticorrosive coating system beneficial is provided either by a phosphate conversion coating and the primer, poly(MMA-co-BA) waterborne latex (MB) with phosphated functionalities (provided by using a polymerizable phosphate surfactant) was synthesized in order to trigger the formation of a passive thin iron phosphate layer at the metal-coating surface during its application. In fact, it was found that the phosphate waterborne latex was able to phosphatize the steel surface when cast onto low carbon steel and dried under slow drying rate ($T=23\text{ }^{\circ}\text{C}$ and $\text{RH}=60\%$).

It was found that in harsh exposure conditions the coatings that contained the in-situ produced phosphatization layer were able to present excellent corrosion protection after 400 h in salt-spray chamber, whereas latexes produced with the same composition but using a conventional non-polymerizable and non-phosphate containing group, failed and corrosion started on the steel substrates.

In an attempt to increase the barrier properties of this initial waterborne phosphate containing latex, the incorporation of high hydrophobic perfluorooctyl acrylate (POA) into the polymer composition was targeted and was successfully performed by seeded semibatch emulsion polymerization in which the seed (with the whole amount of POA

required to obtain a final composition of POA/MMA/BA = 30/40/30) was made by miniemulsion polymerization. However, despite the enhanced hydrophobicity and the presence of iron phosphate layer at the coating-substrate interface, the coating cast from PMB was not able to protect the metal substrate against corrosion in the harsh conditions present in the salt spray chamber. By SEM analysis, it was found that the particles were not able to coalesce and they generated channels through which the corrosive species were able to diffuse till the metal surface.

It has been found that the incorporation of POA comonomer generated latex particles with core-shell-shell morphology (with a POA enriched phase phase-separated from the rest of the particle and arranged in the inner-shell), which is likely the reason of the observed lack of particles coalescence. However, the understanding of the causes that brought to this morphology resulted out of the scope of this thesis and was carried out independently.

In order to overcome the poor anticorrosive performance of POA containing latex, the encapsulation of ZnO nanoparticle was chosen as possible route. Nanohybrid latexes containing ZnO nanoparticles and phosphate functionalities was successfully carried out by a seeded semibatch emulsion polymerization process in which the ZnO nanoparticles were encapsulated in the seed preparation process (by miniemulsion polymerization) and the phosphate groups, belonging to the SIP, were gradually added

during the semibatch process. In this way the observed detrimental interaction between the phosphate groups of the SIP and the ZnO nanoparticles was avoided. Unfortunately, the encapsulation of ZnO nanoparticles produced just a slight enhancement of the corrosion protection in harsh conditions if compared with the analogous system without the nanoparticles (substrate coated with PMB_DSZnO started to corrode after 24 h of exposure in salt spray chamber instead of immediately after being exposed to the salt spray like PMB coated substrate; see Chapter 3). This result indicates that the incorporation of ZnO nanoparticles is not enough to overcome the problem of the lack of coalescence of polymer particles of PMB latexes.

Due to the observed lack in the film formation of latex containing POA, the incorporation of hydrophobic Stearyl Acrylate into the latex composition was implemented as alternative. Film forming latexes with core-shell morphology having semicrystalline polymer in the core and amorphous polymer surrounded by phosphate functionalities on the particles surface (SA40 and SA50) were synthesized by seeded semibatch emulsion polymerization. The synergic effect of enhanced barrier properties and substrate phosphatization play a key role on the anticorrosion protection. It was found that in harsh exposure conditions (exposition to 5 wt% NaCl aqueous salt spray) the SA40_T60 coating was able to present excellent corrosion protection after 800 h of

exposure, which is double the time that the fully amorphous coating was able to tolerate (400 h) in the salt spray chamber.

Finally, the incorporation of phosphated waterborne latexes (MB, SA40 and SA50) into commercial paint formulations for direct to metal (DTM) application provide paints with comparable anticorrosion properties of a commercial DMT paint but without the use of corrosion inhibitors, which suggest that the synergy of the in-situ phosphatization ability (provided by the presence of phosphate functionalities) with the barrier protection of a coherent film might be used as strategy to reduce or eliminate the addition of anticorrosion inhibitors.

List of publications and conference presentations

Part of this Thesis has been published or will be published soon. The list of papers that would be issued from this work is as follows (variation in the authors list and/or paper title might be possible).

“Effective incorporation of ZnO nanoparticles by miniemulsion polymerization in waterborne binders for steel corrosion protection” Stefano Chimenti, Jesús Manuel Vega, Miren Aguirre, Eva García-Lecina, José Antonio Díez, Hans-Jurgen Grande, María Paulis, Jose Ramón Leiza. *Journal of Coating Technology and Research* (2017) 14: 829.

PCT/EP-2019/052860 International patent application entitled **"A Method for Providing Coating Systems with Corrosion-Protective Properties"** Stefano Chimenti, Jesús Manuel Vega, Eva García-Lecina, María Paulis, Jose Ramón Leiza (06-Feb-2019).

“In-situ phosphatization and enhanced corrosion properties of films made of phosphate functionalized nanoparticles”. Stefano Chimenti, Jesús Manuel Vega , Eva García-Lecina, María Paulis, Jose Ramón Leiza. Submitted to *Reactive and Functional Polymers* (04/04/2019).

“Synergic effect of semicrystalline nanodomains and in-situ phosphatization on the anticorrosion properties of waterborne latexes” Stefano Chimenti, Jesús Manuel Vega, Eva García-Lecina, María Paulis, Jose Ramón Leiza. To be submitted to *Industrial & Engineering Chemistry Research*.

“Evaluation of the anticorrosion properties of fluorinated-phosphate based waterborne binder by EIS and SKP” Stefano Chimenti, Jesús Manuel Vega, Eva García-Lecina, María Paulis, Jose Ramón Leiza. To be submitted to *Progress in Organic Coating*.

“The Influence of incorporation of perfluorinated monomer on the particles morphology and film formation of waterborne acrylic latex” Stefano Chimenti, Jesús Manuel Vega, Eva García-Lecina, María Paulis, Jose Ramón Leiza. To be submitted

Part of this work have been presented in national and International conferences, as well as in internal meetings from the Industrial Liaison Program (ILP).

Oral presentations

“Influence of phosphate-based surfactants on the corrosion protection properties of waterborne coatings” Stefano Chimenti, Jesús Manuel Vega, Eva García-Lecina, María Paulis, Jose Ramón Leiza. *12th Coatings Science International Conference (COSI-2016)*.

“Improved adhesion and corrosion protection using novel waterborne binders” Stefano Chimenti, Jesús Manuel Vega , Eva García-Lecina, María Paulis, Jose Ramón Leiza. *European Corrosion Congress (EUROCORR 2016)*.

“Synthesis of waterborne binders for anticorrosive applications” Stefano Chimenti , Jesús Manuel Vega , Eva García-Lecina, María Paulis, Jose Ramón Leiza, *ILP Meeting (2016)*.

“Evaluation of the anticorrosion properties of fluorinated-phosphate based waterborne binder by EIS and SKP” Stefano Chimenti, Jesús Manuel Vega , Eva

García-Lecina, María Paulis, Jose Ramón Leiza. *11th International workshop on Application of Electrochemical Techniques to Organic Coatings (AETOC 2019)*.

Poster presentations

“Incorporation of ZnO nanoparticles in waterborne binders as steel corrosion inhibitors”. Stefano Chimenti, Jesús Manuel Vega, Eva García-Lecina, María Paulis, Jose Ramón Leiza. *International Polymer Colloids Group meeting (IPCG 2017)*.

“Waterborne binders for anticorrosion coatings” Stefano Chimenti, Jesús Manuel Vega, Eva García-Lecina, María Paulis, Jose Ramón Leiza. *WindEurope conference & exhibition 2019*.

Appendix I

Materials and experimental setup

I.1	Materials.....	240
I.2	Experimental setup	241

I.1 Materials

Methyl methacrylate (MMA) and n-butyl acrylate (BA) (Quimidroga), 1H,1H,2H,2H-Perfluorooctyl acrylate (POA, Interchim) and stearyl acrylate (SA, Aldrich) monomers were used as received.

Dodecyl diphenyloxide disulfonate (Dowfax 2A1 45%, Dow Chemical company, DOW) was used as anionic emulsifier. Phosphate esters of polypropylene glycol monomethacrylate Sipomer[®] PAM200, (Solvay, SIP) was used as surfmer. Sipomer[®] PAM 200 is a surfmer characterized by a short polypropylene glycol chain (Mn = 500 g/mol) with a polymerizable acrylic end group and a phosphate group as polar chain end.

Potassium persulfate (KPS, Fluka) and Azobisisobutyronitrile (AIBN, Fluka) radical initiators and Bruggolite (FF6, Brüggeman), Tertbutyl Hydroperoxide (TBHP, Sigma Aldrich) were used as received.

The hydrophilic and hydrophobic ZnO nanoparticles dispersions were kindly supplied by ALTANA (Germany) with nanoparticles concentration of 40 wt%. Hydrophobic ZnO were dispersed in methoxypropyl acetate (ZnO(MPA), NANOBYK 3841, 40 nm), while the hydrophilic nanoparticles were dispersed in water (ZnO(H₂O), NANOBYK 3840, 40 nm).

Sodium bicarbonate (NaHCO_3 , Sigma Aldrich) was used as a buffer, to reduce the electrostatic interaction among droplets and to control the viscosity of the miniemulsion. Deionized water (MiliQ quality) was used in all reactions.

Steel substrates (medium carbon steel with 0.5% of C) were purchased from Urduri S.L. UniClean 251 (Atotech) was used as degreasing agent for the steel substrates. HCl 1M solution (Aldrich) was used in the cleaning treatment of the steel substrates. High purity NaCl (Corrosalt, Ascott-Analytical) was used for the preparation of a 5 wt% solution that was used in the salt spray test.

I.2 Experimental setup

Batch and semibatch emulsion polymerizations were carried out in 1 L jacketed glass reactor equipped with reflux condenser, steel anchor stirrer, and nitrogen inlet (flow rate: 10 mL/min). The control of the reaction temperature and inlet flows of the semi-continuous feeds was carried out by means of an automatic setup that uses the commercial software CamileTG (Biotage). The scheme of the polymerization setup is presented in Figure I.1.

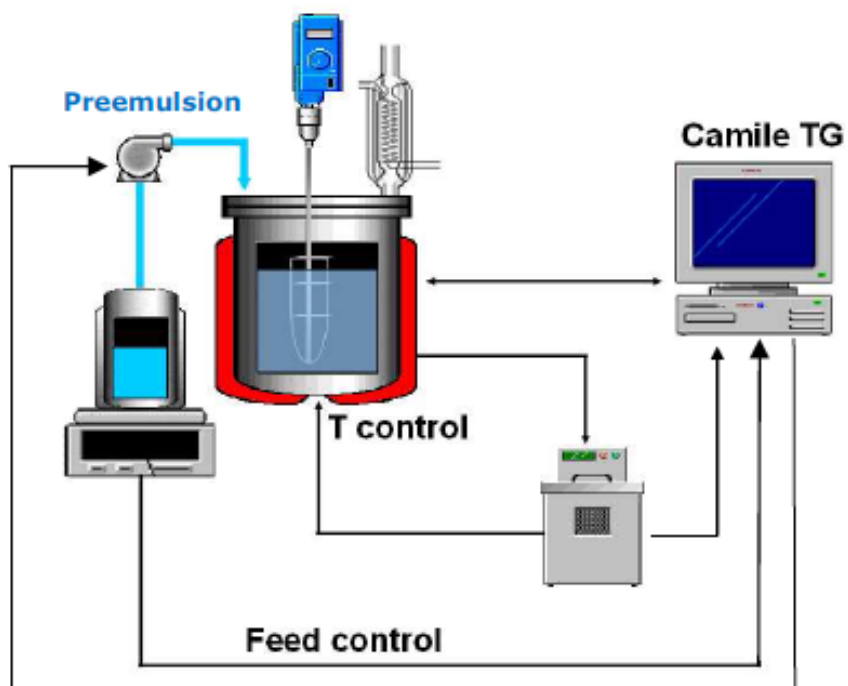


Figure I.1. *Scheme of the polymerization setup*

Appendix II

Characterization and preparation methods

Appendix II

II.1	Conversion	245
II.2	Contact Angle measurement	246
II.3	Dynamic light scattering	246
II.4	Differential Scanning calorimetry (DSC)	246
II.5	Electrochemical Impedance Spectroscopy (EIS)	247
II.6	Film application on steel substrates	248
II.7	FTIR	249
II.8	MALDI-TOF	250
II.9	Multispeckle Diffusing Wave Spectroscopy (MDWS)	250
II.10	Nuclear Magnetic Resonance (NMR)	252
II.11	Powder Wettability test	253
II.12	Scanning electron microscopy with Energy dispersive X-rays analysis (SEM/EDX)	254
II.13	Scattering-type Scanning Near-field Optical Microscope (sSNOM)	255
II.14	Salt Spray test	255
II.15	Transmission Electron Microscopy (TEM)	256
II.16	Water sensitivity	257
II.17	References	257

The following characterization methods (listed in alphabetical order) were used during the study.

II.1 Conversion

Approximately 2 mL of the latex were withdrawn from the reactor during the polymerization process, placed in a pre-weighted aluminum pan and immediately thereafter a drop of 1 wt% hydroquinone solution was added to stop the reaction. The pan was dried until constant weight was achieved. The solids content (SC) was obtained gravimetrically and is given by:

$$SC = \frac{\textit{Weight of the dried solid material}}{\textit{weight of the latex}}$$

The instantaneous conversion (X) was determined by the following equation

$$X(t) = \frac{\textit{Polymerized Monomer}}{\textit{Total Monomer}} = \frac{(SC \cdot \textit{Latex}) - \textit{NPS}}{\textit{TM}}$$

Where, NPS is the non-polymerizable material (inorganic nanoparticles, surfactants, buffer and initiator).

II.2 Contact Angle measurement

Water contact angles were measured in a OCA 20 instrument (Dataphysics). Films from the different latexes were cast on glass substrates and then dried for 24 hours at 23 °C and 60 % RH. The measurement of contact angle was done by placing 10 µl droplets of distilled water on the surface of the films. The values given are an average of twenty measurements per film.

II.3 Dynamic light scattering

Monomer droplet and particle sizes were measured by dynamic light scattering in a Zetasizer Nano Z (Malvern Instruments). The samples were prepared by dilution of the latex in distilled water. The values given are z-average values obtained through cumulants analysis. The equipment was operated at 20 °C and the values reported were the average of two repeated measurements.

II.4 Differential Scanning Calorimetry (DSC)

The thermal transitions of the analysed polymers were determined by differential scanning calorimetry (DSC, Q1000, TA instruments). The samples were prepared by casting at 23 °C the final latexes. The scanning cycles consisted of first cooling to -50 °C at 10 °C/min, then heating from -50 to 150 °C at 10 °C/min, cooling again from

150 to -50 °C at 10°C/min, and then heating to 150 °C at a rate of 10°C/min. The first heating scan is a better representative of the film cast at 23 °C. This heating scan allows greater phase separation and hence in the second run the transitions are often better defined. The crystallinity of the polymers containing SA, Xc, was calculated as $\Delta H_f / \Delta H_{f0}$, where ΔH_f is the observed calorimetric heat of fusion of the existing crystals and ΔH_{f0} is the heat of fusion for the 100% crystalline phase that, for pure PSA has been reported to be 219.5 J/g.

II.5 Electrochemical Impedance Spectroscopy (EIS)

Electrochemical tests were performed using a multichannel potentiostat BIO-LOGIC VMP3 to evaluate the corrosion behaviour of the systems. A typical three electrodes cell, with a saturated Ag/AgCl (saturated with KCl) as reference electrode, platinum mesh counter electrode and the different coatings (cast from the synthesized latexes) as working electrode were used. Electrochemical experiments were carried out at least by triplicate using an area of 1 cm². The electrochemical tests were conducted in 3.5 wt% NaCl solution at room temperature. OCP was measured continuously with time although it was interrupted to carry out EIS measurements (once per hour). Frequency scans were carried out by applying ± 10 mV sinusoidal wave perturbation versus OCP.

The frequency range was from 100 Hz to 10 mHz, obtaining 10 points per decade.

Figure II.1 depicts the scheme of a typical EIS measurement.

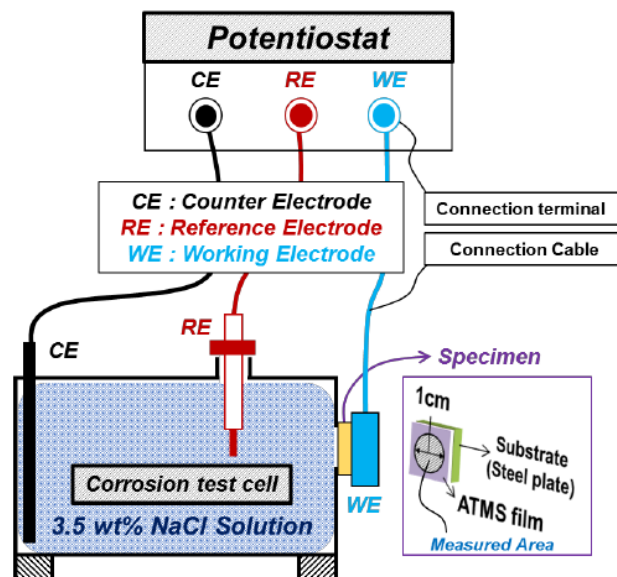


Figure II.1 Scheme of EIS setting.

II.6 Film application on steel substrates

The latexes and the paints were cast onto steel substrates according to two different procedures. The first procedure was used as the general cleaning procedure and only in Chapter 7 the second procedure was implemented.

1. Cleaning with Uniclean (Procedure U); Before casting the latex, steel substrates were degreased with UniClean 251 solution at 70 °C in a shaking

bath for 5 minutes followed by 1 min decapping in HCl solution (1:1). Then the waterborne latexes (or paints) were uniformly applied on the steel substrates with quadruple film applicator (Khushbooscientific) in the case of latex application, whereas a roll bar applicator was used for the paint casting.

2. Cleaning with acetone (Procedure A); Before casting the paint, steel substrates were degreased with acetone at ambient temperature. Then the paints were uniformly applied on the steel substrate with a roll bar applicator.

Subsequently the coatings were dried under different conditions (changing temperature and Relative Humidity) using a temperature and humidity chamber (ESPEC SH-641).

II.7 FTIR

The FTIR absorption spectra were recorded using a Bruker Single reflection ATR with Platinum module in the range of wavelength comprised within 400 and 4000 cm^{-1} with a resolution of 1.0 cm^{-1} . The samples were prepared from the casting of the latex at ambient conditions and letting them dry for 24 hours. For each sample an average of 5 spectra were recorded in order to check the reproducibility.

II.8 MALDI-TOF

Matrix Assisted Laser Desorption Ionization Time of Flight Mass Spectrometry (MALDI-TOF MS) measurements of Sipomer PAM200 and Sipomer PAM200 with ZnO nanoparticles dispersion, were carried out on a Bruker Autoflex Speed system (Bruker, Germany). The instrument was equipped with a 355 nm Nd:YAG laser. All spectra were acquired in the positive-ion linear and reflectron modes. The samples were diluted in milliQ water just before analysis at 2 g L^{-1} . Approximately $0.25 \text{ }\mu\text{L}$ of the dissolved sample were hand spotted onto a PACII target. This target contained α -cyano-4-hydroxycinnamic acid (CHCA, Aldrich) matrix. When the sample was air dried, the MALDI sample plate was inserted into the spectrometer and spectra were acquired under high vacuum conditions. For each spectrum, 5000 laser shots were accumulated.

II.9 Multispeckle Diffusing Wave Spectroscopy (MDWS)

Adaptive Speckle Imaging Interferometry (ASII) optical technique, which is based on the Multispeckle wave spectroscopy (DWS), was used to analyze the film formation process¹. The Horus® (Formulation) was used to perform the analyses. The principle

of the measurements consists on sending a laser light into the film. Part of incident coherent light is absorbed by the sample and the other part is scattered back and detected by the video camera through an interference image, also called Speckle image. During film formation the sample undergoes some changes such as particle movement or refractive index changes; this activity causes temporal fluctuations in the scattered light and, consequently, random changes of light intensity on the Speckle image. The speed of light fluctuations (the Speckle rate) during the drying process is directly related to the motion of the scatterers inside the sample (i.e. the latex particles). The motion of the particles is strongly dependent on the viscosity of the film in the way that as water evaporates, viscosity rises and the scatterers motion (Speckle rate) slows down. The main stages during film formation can thereof be associated with changes in the Speckle rate as shown in Figure II.2. In all the cases the measurements were done for 60 μm (wet thickness) films cast from the synthesized latexes drying at a relative humidity of 60% and a temperature of 23°C.

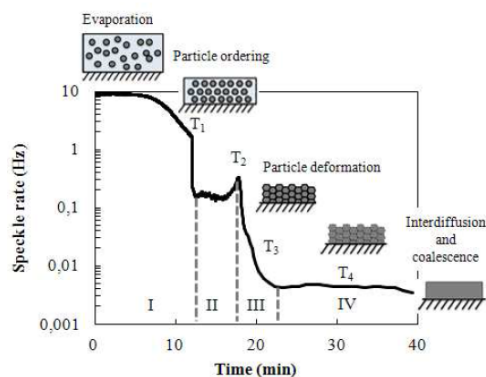


Figure II.2 Drying kinetics of water-borne PSA as interpreted in the application notes of the Horus® (<http://www.formulaction.com/microrheology-horus.html>).

To perform gravimetric analysis of water loss during latex drying, 60 μm wet films were cast onto glass substrate (10cm x 5cm), and immediately samples were placed on a digital balance and the weight was recorded every minute during 1 hour.

II.10 Nuclear Magnetic Resonance (NMR)

Conversions were measured by ^1H -NMR spectroscopy employing the watergate sequence using a Bruker AVANCE 400 MHz instrument. 500 μL of the withdrawn sample were added to the NMR tube followed by the addition of 50 μL of deuterated water (D_2O).

II.11 Powder Wettability test

Powder wettability measurements were carried out to measure the compatibility between inorganic ZnO nanoparticles and water and monomer phase; KSV Sigma 700/701 tensiometer was used for this purpose. The wetting of a powder involves contact angle phenomena but in this study the static contact angle measurement is characterized by the absorption in a porous architecture. In detail, a rough estimation of wettability can be done by placing the powder in contact with a liquid and observing if the liquid rises into the pores of the solid. This phenomenon is described by the Washburn relationship²:

$$T = [\eta / C \rho^2 \gamma \cos\theta] M^2$$

The terms are defined as follows;

T = Time after contact

η = viscosity of the liquid

C= material constant characteristic of the solid sample

ρ = density of liquid

γ = surface tension of the liquid

θ = Contact angle

M= mass of liquid absorbed in solid

According to the Washburn method, the powder, placed in the equipment support, is tested firstly with a completely wetting liquid, assuming the $\theta = 0$ and solving for C . Then assuming C is constant, the powder can be tested against various liquids to find the contact angles.

II.12 Scanning Electron Microscopy with Energy Dispersive X-rays analysis (SEM/EDX)

SEM with Energy Dispersive X-Ray analysis (SEM-EDX), was used to visualize the morphology of the coatings cross section and to define their composition. The cross sections of the film cast on silicon molds were produced by immersing them into liquid nitrogen until their fracture. All the measurements were performed using a table top SEM 3030 Hitachi operating at 15 kV and at low vacuum. Furthermore, the composition profile of the coating applied onto the steel substrate was obtained using a Quantax EDS Bruker operating at 8 kV and in charge up reduction mode.

In the case of coated steel specimen, the coating was detached from the steel surface by immersion in liquid nitrogen after being applied and then analyzed according to the same procedure previously described.

II.13 Scattering-type Scanning Near-field Optical Microscopy (sSNOM)

The IR s-SNOM images and nano-FTIR spectra, as well as the corresponding AFM images, were recorded with a neaSNOM system (Neaspec GmbH, Germany) comprising both s-SNOM and nano-FTIR capabilities. Pt-Si coated AFM tips were used. IR s-SNOM imaging of the film cross sections were performed with illumination from a grating-tunable CO₂ laser. Nano-FTIR spectroscopy of the sample was performed with illumination from amid-infrared laser supercontinuum, using Au coated AFM tips. The final nano-FTIR spectra were obtained by averaging 25 individual spectra. The total acquisition time was 15 min and the spectral resolution 16 cm⁻¹. The spectra were normalized to that obtained on a clean gold surface (reference measurements).

II.14 Salt Spray test

Three specimens were used to perform neutral salt spray tests (NSS) for each system. Experiments were conducted using a DYCOMETAL MODEL SCC-400 salt spray chamber for 800 h. Test parameters were set according to ASTM B117 standard. Visual evaluation was carried out according to ISO 10289:1999 standard.

II.15 Transmission Electron Microscopy (TEM)

The morphology of latex particles and films was studied by means of transmission electron microscopy (TEM). TEM analysis was carried out with a Tecnai TM G2 20 Twin device at 200 kV (FEI Electron Microscopes). The latexes were diluted with deionized water (with a concentration of 0.05 wt%) placed on copper grids covered with Formvar R and dried at ambient temperature. The films were cryosectioned with a Leica EMUC6 cryoultramicrotome at 30 °C below the T_g of the sample, with a Diatome 45° diamond 30 knife, and the observations were made in the microscope described above.

High-angle annular dark-field scanning transmission electron microscopy (HAADF-STEM) analysis was also used for study the latex particles morphology by means of the same microscope described above. STEM_HAADF is a STEM method which receives inelastically scattered electrons or thermal diffuse scattering (TDS) at high angles using an annular dark-field (ADF) detector ($\sim 50^\circ$ to sufficiently high angle; e.g. ~ 200 mrad). A STEM image is acquired by displaying the integrated intensities of the electrons in synchronism with the incident probe position. As the HAADF image intensity is reported to be proportional to 1.4 square to a square of the atomic number, heavy atoms are observed brighter. The HAADF image is easily interpreted due mainly

to two reasons. 1) No multiple scattering arises because the scattering cross section of TDS at high angles used for the imaging is small. 2) The interference effect of electrons does not take place for the imaging (non-interference image).

II.16 Water sensitivity

Water sensitivity and barrier properties were assessed by liquid water uptake (WU) test, that consists in monitoring for 15 days the relative weight gain of circular polymeric specimens (diameter = 24 mm, thickness= 2.3 mm) in water, and by water vapor transmission rate (WVTR), in which circular polymeric specimens, of the same dimensions as before, follow the cup test described in the ASTM E96.

II.17 References

1. Brun, A.; Dihang, H.; Brunel, L., Film formation of coatings studied by diffusing-wave spectroscopy. *Progress in Organic Coatings* **2008**, *61* (2), 181-191.
2. Washburn, E. W., The dynamics of capillary flow. *Physical review* **1921**, *17* (3), 273.

Appendix III

Supporting Information

III.1	Chapter 1	261
III.2	Chapter 2	263
III.3	Chapter 3	265
III.4	Chapter 5	266
	III.4.1 MALDI-TOF characterization	266
	III.4.2 ZnO encapsulation semibatch reaction screening	268
III.5	Chapter 6	269
III.6	Chapter 7	269
	III.6.1 Pigments	270
	III.6.2 Thickeners	270
	III.6.3 Dispersing agent	271
	III.6.4 Defoamer	272
	III.6.5 Biocide	272
III.7	Reference	273

III.1 Supporting information for Chapter 1

Emulsion and miniemulsion polymerization technology

Is it known that typically the monomer solubility in water is limited, however, by means of emulsion polymerization the synthesis of a stable polymer colloid in water phase is achievable. Emulsion polymerization is an oil-in-water emulsion stabilized by surfactant which is polymerized using a free-radical initiator. In this process the nucleation of polymer particles takes place by entry of radicals into micelles (heterogeneous or micellar nucleation) or by precipitation of growing oligoradicals in the aqueous phase (homogeneous nucleation)¹⁻⁴. Once the particles are formed in emulsion polymerization, the polymer particles undergo substantial growth by polymerization. The monomer required for the polymerization is to be transported from the monomer droplets by diffusion through the aqueous phase. This represents, in many cases, a limitation of the emulsion polymerization technique because it is very difficult to incorporate very hydrophobic monomers into the polymer particles due to their limited or negligible diffusion through the aqueous phase. The need of mass transport of monomer through the aqueous phase would be greatly reduced if all (or a large fraction) of the droplets are nucleated. The nucleation in monomer droplets can be enhanced if the droplet size is reduced and the surface area of the droplets is large as

compared with that of the micelles and hence droplet nucleation prevails over the other nucleation mechanisms.

What is known as miniemulsion polymerization is basically an oil-in-water emulsion where the size of the monomer droplets has been considerably reduced (50-500 nm) by combining a suitable emulsifier and an efficient emulsification technique and stabilizing the resulting miniemulsion against diffusional degradation. Under this condition, the surfactant is adsorbed on the large surface area of the monomer droplets and hence (ideally in a well formulated miniemulsion) the available surfactant to form micelles is negligible and micelles are not present in the dispersion.

Therefore, if a water-soluble initiator is added to the system and oligoradicals are formed in the aqueous phase, they preferentially enter into monomer droplets that become polymer particles; namely, the main nucleation mechanism is droplet nucleation. The droplet nucleation is a unique feature of the miniemulsion polymerization⁵, which allows the production of polymers that cannot be produced by any other polymerization technique⁶⁻¹¹. If all the monomer droplets present in the original dispersion (monomer miniemulsion) capture radicals, all the droplets become polymer particles. This has been taken as an inherent feature of the miniemulsion polymerization, but it hardly takes place in practice⁹; namely, in addition to droplet

nucleation other nucleation mechanisms such as homogeneous and micellar nucleation might also take place as well as droplet coagulation and degradation.

III.2 Supporting information for Chapter 2

Figure III.1 shows the FTIR adsorption spectra (recorded range of $400\text{-}4000\text{ cm}^{-1}$) of the surface of the detached coating, cast from MB_S under fast drying rate (RH=43%), at the coating-air (a) and coating-steel (b) surface respectively. The measurement was carried out in order to prove the absence of iron phosphate and hence to confirm the fact that at higher drying rate the phosphate groups of the latex particles did not have enough time to interact with the hydroxyl groups of the steel surface. As it can be seen, both surfaces, the one in contact with air and the one in contact with the steel present the same spectra, showing that no Fe phosphates were produced in this case (Figure III.2)

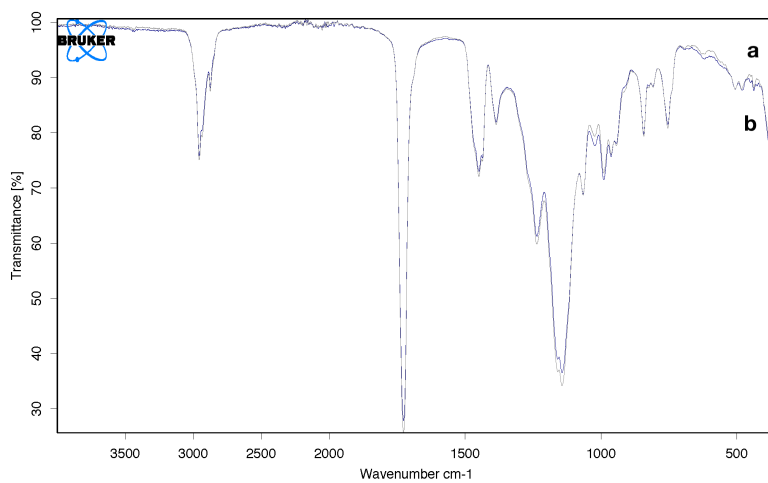


Figure III.1 FTIR spectra of the film surface at the coating-air (a) and coating-steel (b) interface.

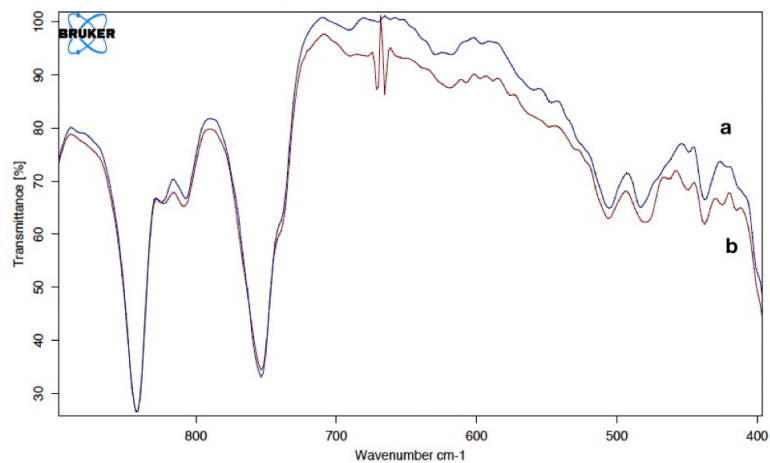


Figure III. 2. FTIR spectra of the MB-S film surface dried at at RH =43 % at the coating-air (a) and coating-steel (b) interface.

III.3 Supporting information for Chapter 3

The composition of the latex described in Chapter 3 was a result a preliminary screening of several polymer compositions (Table III.1) containing perfluoro octyl acrylate (POA) in different amounts, in combination with different amounts of methyl methacrylate (MMA) and n - butyl acrylate (BA) comonomers and different amounts of surfactants (DOWFAX (Dow) and SIPOMER PAM200 (SIP)).

Table III.1 List of reactions containing Perfluorooctyl acrylate (POA) carried out during the thesis.

RUN	COMPOSITION (%)			REACTION	Surfactant	NOTE
	POA	MMA	BA			
pPOA_D	100	-	-	batch	2% Dow	
pPOA_S1	100	-	-	batch	3% SIP	Coagulum pH = 2/3
pPOA_S2	100	-	-	batch	3% SIP	No coagulum (pH = 7 corrected by ammonia)
pPOA_S3	100	-	-	batch	2% SIP	No coagulum (pH = 7 corrected by ammonia)
PM_S	80	20	-	batch	2% SIP	Tg= 10 °C
PM_D	80	20	-	batch	2% Dow	Tg=27 °C
MPB_S1	40	40	20	batch	3% SIP	
MPB_S2	30	40	30	batch	2% SIP	Tg= 10 °C
MPB_S3	30	40	30	batch	2% SIP	
PMB_S1	30	40	30	semibatch	2 % SIP	Tg= 15 °C

III.4 Supporting information for Chapter 5

III.4.1 MALDI-TOF characterization

In order to confirm the possible interaction between SIP and ZnO(MPA), further stability tests were carried out; 0.5 g of ZnO(MPA) and 0.4 g of SIP were added to 30 g of water and mixed under magnetic stirring at ambient temperature. The resulting mixture was stable. However, as soon as the pH was increased to 7, a yellowish coagulum appeared immediately in the solution which justify our hypothesis. Figure III.3 compares the MALDI mass spectra of a solution of Sipomer (a) with the spectra of the ZnO-SIP dispersion, acquired before (b) and after (c) the pH correction. As it can be seen in spectrum c, after increasing the pH from 3 to 7, the characteristic repeating unit of poly propylene glycol (PPG) bearing to SIP (58 g/mol) was not present anymore. The coagulum was also analyzed and the resulting spectrum (Figure III.3 d) confirms the precipitation of SIP by the presence of PPG chain repeating unit.

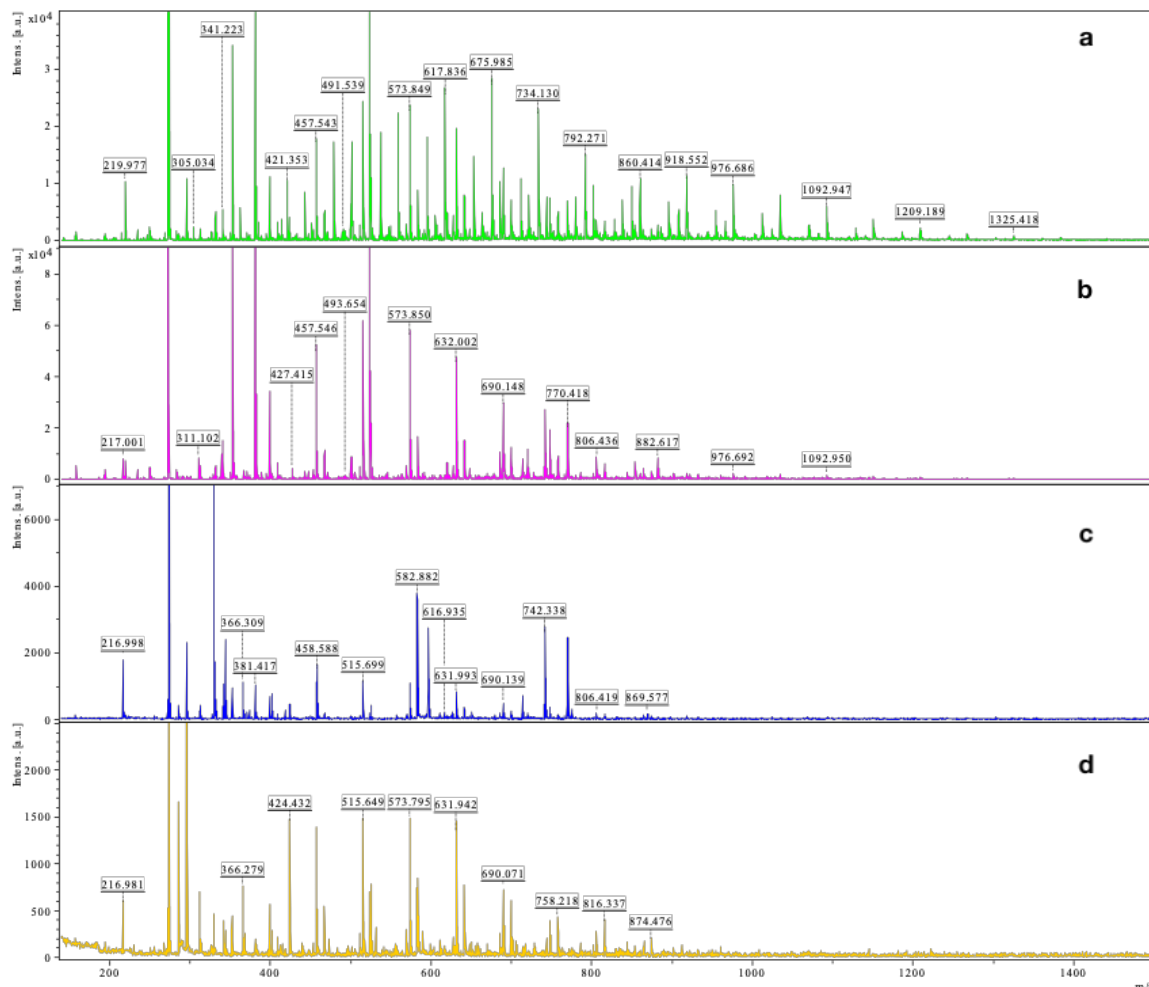


Figure III.3. MALDI-TOF mass spectra of a) SIPOMER PAM200 solution, b) ZnO-SIP solution pH=3 c) ZnO-SIP solution pH=7 and d) the coagulum formed after the increase of the solution pH.

III.4.2 ZnO encapsulation semibatch reaction screening

The composition of the hybrid latex described in section 5.4 of Chapter 5 was a result a preliminary screening of several latexes compositions (the polymer composition is POA/MMA/BA =30/40/30 and remained unvaried) changing the amount of ZnO nanoparticles (0.5, 1, 1.25 and 2%) and the overall amount of surfactants (SIPOMER PAM200 and DOWFAX). A list of the preliminary reactions carried out with the respective amount of ZnO nanoparticles and surfactants is reported in Table III.2.

Table III.2 *List of screening reactions carried out to find out the optimum reaction recipe*

SAMPLE	ZnO(MPA) (%)*	Surfactant		note
		DOW	SIP	
Z2D1S2	2	1	2	>50% coagulation
Z2D2S2	2	2	2	>50% coagulation
Z2D2S1	2	2	1	>50% coagulation
Z2D1S1	2	1	1	>50% coagulation
Z1.5D1S2	1.25	1	2	12 % coagulation
Z1.5D2S1	1.25	2	1	8 % coagulation
Z1D2S2	1	2	2	<1 % coagulation
Z1D1S2	1	1	2	<1 % coagulation
Z0.5D1S2	0.5	1	2	<1 % coagulation

* with respect to the monomer amount in the seed

III.5 Supporting information for Chapter 6

The thermal properties of latex with core shell morphology synthesized in Chapter 6 (SA40 and SA50 with 40 and 50 % of stearyl acrylate comonomer in the polymer composition respectively) were studied by means of Differential Scanning Calorimetry (DSC). Table III.3 reports the thermal transitions (T_g and T_m), the enthalpy related to the melting transition (ΔH_f) and the crystallinity (X_c) observed in the first heating ramp for films cast from SA40 and SA50 latex, dried at ambient temperature and at 60 °C.

Table III.3. Heat of fusion (ΔH_f), crystallinity (X_c), melting temperature T_m and glass transition temperature (T_g).

		First Heating			
		ΔH_f (J/g)	X_c (%)*	T_m (°C)	T_g (°C)
SA40	Tamb	34.5	15.7	49.0	14.7
	T60 1D	35.6	16.2	49.6	13.8
SA50	Tamb	43.5	19.8	50.3	16.3
	T60 1D	42.0	19.1	49.9	17.3

* calculated considering $\Delta H_f^0 = 219.5 \text{ J/g}^{12}$

III.6 Chapter 7

Waterborne paints are constituted by a large amount of raw of materials. Some of them are briefly described here.

III.6.1 Pigments

The pigment is the discontinuous phase giving additional or improved properties to the coatings. They are solid particles insoluble in the application medium and although most pigments are natural minerals, some are synthesized. Pigments can be divided into two different categories: functional or extenders. Functional fillers, such as titanium dioxide and precipitated calcium carbonate, improve or provide film properties whereas extenders, such as clay, chalk and ground calcium carbonate (GCC) are cheaper and they are primarily used to increase the volume of a given coating and therefore to lower the formulation costs of the final product.

III.6.2 Thickeners

Among the additives, the thickeners are very important in order to achieve the optimum rheology profile desirable for the final applications. If the rheology of the paint is not the proper one, it can affect the paint in terms of manufacturing, storage and application. Paints based on binders that are dissolved in organic solvents exhibit a rheological profile that is very favourable with respect to application and film formation. However, when a water based binder dispersion

is mixed with a pigment dispersion, a completely different rheological profile is obtained. For such systems the viscosity over the whole shear rate is usually too low. This disadvantage makes the use of rheology modifiers necessary for water based dispersion paints.

III.6.3 Dispersing agent

During the production of waterborne paints, pigments particles have to be dispersed in water at high speed. In this dispersing process, due to the high speed, pigments agglomerates are dispersed to primary particles. However, in the absence of a dispersing agent these primary particles can flocculate again. The flocculation is due to the Brownian motion of the particles. Small particles move randomly in a suspension, collide with each other and flocculate, reducing their total surface energy. Therefore, when formulating a coating, the role of the dispersing agent is very important, to ensure well dispersed pigmented coatings with good final performances. If pigment particle aggregates are present, final properties such as gloss, opacity, strength, colour distribution and storage stability will be highly affected.

III.6.4 Defoamer

Foam is created when air is introduced into paint during manufacturing or application. Complex paint formulations include several vehicles that promote foam stabilization, i.e., wetting agents, dispersants, and emulsifiers. These surfactants stabilize the foam due to one or several mechanism available to them including hydrogen bonding, ionic, and van der Waals forces. Foaming is highly undesirable and almost unavoidable. It reduces manufacturing efficiency and causes film defects. This necessitates the use of foam control agents—surface-active additives that prevent, reduce, or eliminate foaming during manufacturing and application.

III.6.5 Biocide

Water-based paints are prone to contamination and spoilage by bacteria and occasionally unicellular fungi (i.e., yeast) and filamentous fungi. Bacterial growth requirements include water, a carbon source, an energy source, oxygen for aerobes, and other macroelements, such as nitrogen and phosphorus. The majority of bacteria grow between 10 and 50 °C and pH range of 3–11. Paint formulations provide an adequate supply of the minimal nutrients at the ideal

pH and temperature to maintain bacterial growth. To prevent these problems from occurring, the appropriate Biocide must be incorporated into the coating formulation. In addition to being cost-effective, the biocide should be compatible with all coating components, be stable within a range of pH, temperature, and time period, have no effect on rheology, impart no discoloration or odors to the coatings, be water soluble in concentrations used, and be environmentally acceptable.

III.7 Reference

1. van Herk, A. M., *Chemistry and technology of emulsion polymerisation*. John Wiley & Sons: **2013**.
2. Lovell, P. A.; El-Aasser, M. S.; Lovell, P., *Emulsion polymerization and emulsion polymers*. Wiley New York: **1997**.
3. Li, B.; Brooks, B., Semi-batch Processes for Emulsion Polymerisation. *Polymer international* **1992**, 29 (1), 41-46.
4. Barandiaran M.J., de la Cal J.C., Asua. J.M., Emulsion Polymerization. In *Polymer Reaction Engineering* Wiley, **2007**.

5. Ugelstad, J.; El-Aasser, M. S.; Vanderhoff, J. W., Emulsion polymerization: Initiation of polymerization in monomer droplets. *Journal of Polymer Science*, **1973**, *11* (8), 503-513.
6. Hutchinson, R. A.; McMinn, J. H.; Paquet, D. A.; Beuermann, S.; Jackson, C., A Pulsed-Laser Study of Penultimate Copolymerization Propagation Kinetics for Methyl Methacrylate/n-Butyl Acrylate. *Industrial & Engineering Chemistry Research* **1997**, *36* (4), 1103-1113.
7. Thickett, S. C.; Gilbert, R. G., Emulsion polymerization: State of the art in kinetics and mechanisms. *Polymer* **2007**, *48* (24), 6965-6991.
8. Braunecker, W. A.; Matyjaszewski, K., Controlled/living radical polymerization: Features, developments, and perspectives. *Progress in Polymer Science* **2007**, *32* (1), 93-146.
9. Asua, J. M., Miniemulsion polymerization. *Progress in Polymer Science* **2002**, *27* (7), 1283-1346.
10. Chern, C.; Chen, T., Miniemulsion polymerization of styrene using alkyl methacrylates as the reactive cosurfactant. *J Colloid Polymer Science*. **1997**, *275* (6), 546-554.
11. Wang, S.; Schork, F.; Poehlein, G.; Gooch, J., Emulsion and miniemulsion copolymerization of acrylic monomers in the presence of alkyd resin. *Journal of Applied Polymer Science* **1996**, *60* (12), 2069-2076.

12. Jordan, E. F.; Feldeisen, D. W.; Wrigley, A. N., Side-chain crystallinity. I. Heats of fusion and melting transitions on selected homopolymers having long side chains. *Journal of Polymer Science Part A: Polymer Chemistry* **1971**, *9* (7), 1835-1851.

Acronyms list

A	Acetone cleaning
AFM	Atomic Force microscopy
AIBN	Azobisisobutyronitrile
BA	Butyl acrylate
BLEND	Blend of Poly(POA-co-MMA-co-BA) with ZnO nanoparticles
CMC	Critical Micelle concentration
CA	Static contact angle
D	Diffusion coefficient
DLS	Dynamic light scattering
DOW	DOWFAX 2A1
Dp	Particles diameter
DSC	Differential scanning calorimetry
DTM	Direct to Metal paint
E_{cell}	Electrochemical cell potential

Acronyms list

E_{ox}	Electrochemical half cell potential (Anode)
E_{red}	Electrochemical half cell potential (Cathode)
EDX	Energy dispersive X-ray analysis
EIS	Electrochemical impedance spectroscopy
FF6	Bruggolite
FTIR	Fourier transform infrared spectroscopy
KPS	Potassium persulphate
MALDI	Matrix Assisted Laser Desorption/Ionization analysis
MB	Poly(MMA-co-BA)
MDWS	Multi-speckle diffusive wave spectroscopy
MFFT	Minimum film formation temperature
MMA	Methyl methacrylate
NSS	Neutral salt spray
P	Permeability coefficient
P_MB	Paint based on MB
P_SA	Paint based on SA
POA	Perfluorooctyl acrylate

PMB	Poly(POA-co-MMA-co-BA)
PSA	Poly stearyl acrylate
PUD	Polyurethane dispersion
RH	Relative humidity
S	Solubility coefficient
SA	Stearyl acrylate
SA40	Poly(SA-co-MMA-co-BA) = 40/30/30
SA50	Poly(SA-co-MMA-co-BA) = 50/25/25
SA40_s	Seed of SA40
SA50_s	Seed of SA50
SC	Solids contents
SEM	Scanning Electron Microscopy
SIP	Sipomer PAM200®
sSNOM	Scattering type near field optical microscopy
TBHP	Terbutyl hydroperoxide
T_g	Glass transition temperature
TEM	Transmission electron microscopy

Acronyms list

U	Uniclean 251 cleaning procedure
VOC	Volatile organic compounds
 Z 	Impedance modulus
ZnO	Zinc Oxides nanoparticles
ZnO(H₂O)	ZnO nanoparticles water dispersion
ZnO(MPA)	ZnO nanoparticles methoxy propyl acetate dispersion
WU	Water Uptake
WVTR	Water vapour transmission rate

Resumen y conclusiones

Resumen y conclusiones

En esta tesis se ha llevado a cabo el diseño de látex multifuncionales para aplicaciones en anticorrosión. Teniendo en cuenta que normalmente la protección a la corrosión en un sistema de recubrimiento anticorrosivo viene dado por el recubrimiento de conversión y el primer, se ha diseñado un látex de poly(MMA-co-BA) (MB) con funcionalidad fosfato (dada por un emulsificante fosfatado polimerizable), capaz de formar una capa de pasivación de fosfato de hierro en la interfase entre el polímero y el acero. De hecho se encontró que dicha capa de fosfatización pasivante se producía sobre acero con bajo contenido en carbono en condiciones de secado lentas ($T=23\text{ }^{\circ}\text{C}$ y $\text{HR}=60\%$).

Se encontró que en condiciones de exposición extremas, los recubrimientos que habían creado dicha capa de fosfatización in-situ, mantenían una excelente protección frente a la corrosión hasta 400 horas de exposición a cámaras de niebla salina, mientras que los recubrimientos producidos con látex de la misma composición polimérica pero con emulsificantes convencionales (no polimerizables y no fosfatados) provocaban la corrosión del acero que se encontraba bajo ellos.

En un intento de aumentar las propiedades barrera de este latex inicial conteniendo unidades fosfato, se incorporó un acrilato perfluorado altamente hidrofóbico a la formulación del látex. La incorporación de dicho acrilato perfluorado se llevó a cabo

Resumen y conclusiones

por polimerización en emulsión sembrada en semicontinuo, en la que la siembra se había producido por polimerización en miniemulsión, incorporando todo el monómero fluorado. La composición final del látex fue POA/MMA/BA = 30/40/30 %. Sin embargo, aunque la hidrofobicidad del polímero había aumentado y se seguía disponiendo de los grupos fosfatados en la superficie de las partículas, estos látex no fueron capaces de proteger la superficie metálica contra la corrosión en la cámara de niebla salina. Por microscopía SEM se observó que las partículas no habían coalescido completamente en la etapa de formación de film, lo cual podía estar generando canales por los cuales las especies corrosivas podían estar llegando más fácilmente a la superficie del metal.

Se demostró que la incorporación del monómero fluorado generaba partículas con morfología núcleo-corteza-corteza (con una fase rica en el monómero fluorado en la primera corteza, separada del resto de fases). La falta de coalescencia se atribuyó a dicha separación de fases. Sin embargo, las causas por las que ocurría la separación de fases no se investigó más en profundidad en el ámbito de esta tesis.

Con el objetivo de mejorar la deficiente actuación anticorrosiva del látex conteniendo el monómero fluorado, se decidió estudiar la incorporación de nanopartículas de ZnO en dichos látex. La encapsulación de las nanopartículas de ZnO fue posible gracias a la producción inicial de una siembra por polimerización en miniemulsión conteniendo la

totalidad de las nanopartículas de ZnO, el monómero fluorado y un emulsificante convencional, y a la alimentación y polimerización posterior del resto de monómeros con el emulsificante polimerizable fosfatado. De este modo se evitó la interacción entre las nanopartículas de ZnO y el emulsificante fosfatado, que hacía que el sistema se desestabilizara. Desafortunadamente, la encapsulación de nanopartículas de ZnO sólo produjo una ligera mejora de las propiedades anticorrosivas de los látex fluorados; 24 horas de resistencia a la corrosión en niebla salina frente a corrosión inmediata de los látex fluorados sin ZnO. Por lo tanto este resultado mostró que la incorporación de ZnO no era suficiente para paliar los graves problemas de permeabilidad que producía la ausencia de coalescencia de las partículas en el látex fluorado.

Dada esta ausencia de buena formación de film en los látex conteniendo el monómero fluorado, se pensó en la incorporación del acrilato de estearilo hidrofóbico a la formulación del látex. De nuevo se utilizó la técnica de polimerización en emulsión sembrada en semicontínuo, en la que la siembra se había preparado por polimerización en miniemulsión y contenía la totalidad del acrilato de estearilo, y en la que se seguía incorporando el monómero fluorado. Se vio que en este caso la propiedades barrera mejoradas por la presencia de la fase cristalina del poliacrilato de estearilo y la fosfatización del substrato producían un efecto sinérgico de mejora de las propiedades anticorrosivas. De hecho se comprobó que el látex conteniendo un 40% de acrilato de

Resumen y conclusiones

estearilo (SA40) y secado a 60°C sobre el acero, permitía una resistencia a la cámara de niebla salina de 800 horas, frente a las 400 h que soportaba el látex sin fase cristalina.

Finalmente, los látex fosfatados (MB, SA40 y SA50) se incorporaron en formulaciones comerciales para aplicaciones directas al metal (DTM). Se comprobó que las pinturas obtenidas con los látex sintetizados en este trabajo produjeron propiedades anticorrosivas similares a las de una pintura DTM comercial, pero sin la necesidad de incorporar inhibidores en la formulación.